Multiphysics modeling of mechano-chemo-electrical phenomena on surface manifolds and biomembranes

by

Rahul Gulati

A dissertation submitted in partial fulfillment
of the requirements for the degree of

Doctor of Philosophy
(Mechanical Engineering)

at the
UNIVERSITY OF WISCONSIN-MADISON
2024

Date of final oral exam: 01/16/2024
This dissertation is approved by the following members of the Committee:

Shiva Rudraraju, Assistant Professor, Mechanical Engineering
Christian Franck, Professor, Mechanical Engineering
Krishnan Suresh, Professor, Mechanical Engineering
Xiaoping Qian, Professor, Mechanical Engineering
Aviad Hai, Assistant Professor, Biomedical Engineering

Abstract

Traumatic brain injury (TBI) is a disruption of the normal function of the brain that can be caused due to excessive external loading due to falls, accidents, impacts, blast, etc. The challenges with diagnosis of TBI, the need to predict longtime effects, and the limitations on conducting brain experiments have resulted in a widespread interest in predictive modeling of TBI. However, current state of the art in TBI modeling is significantly limited in its predictive ability due to the use of coarse-scale brain tissue models and the use of mechanical metrics that do not directly correlate with neuron-scale injury responses. Neuron-scale injury response is a complex interaction of mechanical, chemical and electrical disruptions to the functioning of the individual neurons and neuronal clusters. The objectives of this dissertation are two-fold: (1) To develop a novel mathematical representation of action potential propagation in the neurons considering the complex geometric heterogeneity of the axonal and dendritic regions, and (2) Develop numerical models of diffusion on surfaces that are suited for studying mechano-chemical interactions on biological membranes. It is expected that these developments will provide a platform for undertaking deeper numerical investigations into the functioning of neuronal membranes under different mechanical load conditions, thus enabling high fidelity modeling of TBI.

Action potential propagation along the axons and across the dendrites is the foundation of the electrical activity observed in the brain and the rest of the central nervous system. Theoretical and numerical modeling of this action potential activity has long been a key focus area of electro-chemical neuronal modeling, and over the years, electrical network models of varying complexity have been proposed. As part of this thesis, a Poisson-Nernst-Planck (PNP) based electro-diffusive framework that accounts for the underlying spatio-temporal ionic concentration dynamics to model the neuronal action potential propagation and is a more general and comprehensive treatment is detailed. The model of propagation in the axon is also extended to include the dendrites as they play an integral role in the mechanism. In this dissertation, the mathematical framework for understanding the mechanical deformation of a single neuron by considering the neuronal microstructure and microenvironment that are relevant to its structural integrity and its ionic homeostasis through a representation of the underlying viscoelastic networks of the neuronal structural microenvironment is presented.

The second part of this research discusses modeling of diffusion on membranes. Surface transport of ions and proteins is central to the functioning of membrane-bound phenomena in cells. Here we focus on diffusional transport, and its modulation due to curvature of the membranes. An investigation of curvature effects on second and fourth order diffusion, including phase transformations, is presented. The effect of mechanical deformation on diffusion via the curvature effects is discussed. This capability to model mechanical deformation of membranes and its effects on surface transport, and there by on electrical conduction in neurons is expected to provide a platform for deeper multiphysics investigations into biological membranes.

Acknowledgements

I heartedly extend my deepest gratitude to my advisor, Prof. Shiva Rudraraju, whose support, insightful guidance, motivation and scholarly expertise have been instrumental in shaping my academic journey during my Ph.D. journey. I dedicate this work to my family: mom, dad, Sonal (you make my life complete, Will you marry me?), Shubham (brother); their boundless love, understanding, sacrifices and video calls have been the bedrock of this journey. Their unwavering support, belief in my endeavors and ability have given me the strength and energy to overcome challenges and pursue my academic goals. My Ph.D. has been their journey too, as much as mine.

I would also like to greatly thank my committee members: Prof. Franck, Prof. Suresh, Prof. Xiaoping, Prof. Hai for advising me and providing valuable critical comments on my research. I would like to thank all my teachers for always inspiring me, during my high school, undergraduation at IIT Ropar, and at UW Madison. The courses at UW-Madison have been very fascinating and intellectually challenged me. I sincerely thank Prof. Himanshu Tyagi for offering invaluable guidance at critical junctures, without which I wouldn't have reached this point. I would also like to thank my TA advisor's: Dress, Andrew Mikkelson, Prof. Rudykh for nurturing my growth as a Teaching Assistant. I am thankful to my labmates: Kunal, Deb and Prakarsh from whom i have learned many fundamental aspects. They made each day in the lab both productive and enjoyable. Thanks to my collaborators- the PANTHER community, Jamie, Luke, Navid and Nahian for insightful discussions on the related subject.

During my stay in Madison, i got to meet wonderful people who helped me survive difficult times like COVID, Madison winters etc. I am grateful to my Madison family: Debbie, Dean, Jeremy, Emily, Daniel, Mohan, Jojo, Ankur, Akash, Matt, Dwivedi. A special thanks to Debbie for making sure that I do not run out of homemade pumpkin bars. Insightful conversations and moments of respite were invaluable in sustaining me through this journey. I am very thankful to each of them for their continued support, belief in me and for being a pillar of strength for me.

Contents

List of Figures

Chapter 1

Introduction

The brain is a vital and the most complex organ that plays a paramount role to our overall wellbeing and existence. The electro-chemo-mechanical integrity of the brain at the cell scale is critical to maintain a healthy lifestyle. This integrity is essential to the understanding of various neurological disorders and diseases like TBI, Alzheimers, cognitive impairment, depression etc. Computational modeling has the potential to supplement the experimental findings and facilitate the understanding of the phenomena taking place at such small length and timescales. Over the last few decades, a lot of research in terms of the computational modeling has been done at the tissue level but there is lack of understanding of this complex phenomena at the sub-cellular level. In this thesis, we delve into the neuron scale and model the novel propagation of electrical conduction using electro-diffusive modeling. Besides modeling the electrical signaling, we present a mechano-chemo numerical framework capable of modeling various chemical phenomena's on the biological cell membrane. Traditionally, the chemical phenomena such as diffusion, phase transformation have been modeled on a planar surface but in reality, cell membranes are highly curved and curvature plays a critical role to the various physiological processes. It is known that cells alter their geometry to modulate the physiological functions. For instance, the pre-synaptic neuron can modulate the geometry of its membrane to alter the diffusion of neurotransmitters for the post-synaptic neuron. The understanding of these mechano-chemo interactions thus has a pivotal role in understanding the fundamentals of diseases like TBI.

The fundamentals of the electrical activity in the brain is essential to an advanced understanding of TBI. The disruption of this requisite signal, for example due to mechanical stretch, can lead to impeding the communication cascade in the nervous system and lead to a number of diseases. Specifically, considering the presence of nodes of Ranvier along the myelinated axon, single-cable models of the propagation of action potential have been popular. Building on these models, and considering a secondary electrical conduction pathway below the myelin sheath, the double-cable model has been proposed. Such cable theory based treatments have inherent limitations in their lack of a representation of the spatio-temporal evolution of the neuronal electro-chemistry. In contrast, a Poisson-Nernst-Planck (PNP) based electro-diffusive framework accounts for the underlying spatio-temporal ionic concentration dynamics and is a more comprehensive treatment. In this work, a high-fidelity implementation of the PNP model is demonstrated. This model is shown to produce results similar to the cable theory based electrical models, and in addition, the rich spatio-temporal evolution of the underlying ionic transport is captured. Novel to this work is the extension of PNP model to axonal geometries with multiple nodes of Ranvier and multiple variants of the electro-diffusive model - PNP without myelin, PNP with myelin, and PNP with the myelin sheath and peri-axonal space. Further, we apply this spatio-temporal model to numerically estimate conduction velocity in a rat axon. Specifically, saltatory conduction due to the presence of myelin sheath and the peri-axonal space is investigated in Chapter 2.

Chapter 3 extends the propagation of electrical signaling. Here, for the first time, using the PNP theory, we integrate the dendritic spine, soma and the axon region to numerically model the propagation of excitatory synaptic potential in a complete neuronal geometry with the synaptic input at the spines, potential initiating at the axon hillock and propagating through the neuronal axon. The model outputs the scintillating forward propagation of the action potential along the neuronal axons as well as the back propagation into the dendritic spines. We point out the significance of the intricate geometry of the dendritic spines, namely the spine neck length and radius, and the ion channel density in the axon hillock to the action potential initiation and propagation. We also study the role of excitatory synaptic input in multiple dendritic spines to the neuronal communication.

Besides studying the electrical response, the thesis presents the mathematical modeling of the mechanical behavior at the cellular scale considering the sub-cellular proteins in the neuron. Each of the primary load bearing protein is considered to have an equivalent viscoelastic network. The combined mechanical response of the neuron is thus a complex viscoelastic network depending on the primary load bearing constitutive proteins in the various regions such as the cytoskeleton, membrane, extra-cellular matrix etc. The constitutive finite-strain mechanical modeling of viscoelasticity and visco-elasto-dynamics is presented in the Appendix. The free energy density functional consists of the deviatoric part and the volumetric part. The approach of a micro model where the domain consists of a single neuron and a macro model consisting of a group of neurons is adopted.

Biological membranes are ubiquitous in nature and play an important part in maintaining the ionic homeostatis, regulating the cell structure and various necessary physiological processes. It is of prime importance to understand this behavior of the membrane. Giant unilamellar vesicles (GUVs) provide an excellent tool to study the membrane, its constituents namely the lipids, the proteins and to inspect the structure, morphology and phase state of the membrane. Due to their appreciable size, GUVs are now being extensively used to get an insight into the biological systems and the associated cell functions. In Chapter 4, the thesis presents a three-dimensional computational mechanics framework for high fidelity modeling of membrane deformation. Membranes undergo significant morphological changes through deformation e.g. tubular shapes. Besides, presenting the mechanical only phenomena, an investigation of curvature effects on second and fourth order diffusion, including phase transformations is carried out. Diffusion is a fundamental process underlying numerous biological, chemical and physical phenomena at varied length scales. Especially in biophysics, lateral diffusion forms the primary means of transport for signaling pathways, cell growth and injury response, cell motility, proteins and lipids embedded on the cell membrane, cell trafficking, ion transport, and various other physiological cellular functions. Other mechanisms of transport in cells include motor-driven transport and advection by the intracellular cytoplasm [1]. The driving force for diffusion, arising from brownian motion, is the concentration gradient and requires no additional energy input. Disruption of this intracellular transport or signaling can prove to be fatal and lead to numerous diseases. For example, ionic diffusion in dendritic spines of the neuron plays quintessential role in the action potential propagation in neurons. Interruption of this diffusive transport can lead to neurological diseases like Traumatic Brain Injury (TBI), Alzheimers etc.

Modeling GUVs through phase transformation on the membranes can help us in understanding the cellular membranes as GUVs mimic the biological cell membranes.

The mathematical treatment is discussed in detail in the chapter. Curvilinear coordinates using the Kirchoff-Love shell formulation, which is fourth order in the out of plane deformation, is adopted. Surface metric tensor, gradient operator etc are introduced. Mass conserving fourth order partial differential equation of Cahn-Hilliard dynamics is used to describe the physics of the phase transformations. To satisfy the requirement of global C^1 continuous discretization, isogeometric analysis (IGA) using non-uniform rational b-splines (NURBS) has been utilized. The role of Korteweg stress, which arises due to the coupling of the in-plane phase transformation with out of plane bending is demonstrated. The role of curvature on diffusion and phase transformation is studied.

The conclusion and possible future work of this dissertation are presented in Chapter 5. Novel spatio-temporal model of saltatory conduction of the action potential has been presented in this dissertation. In nature, the mechano-chemo-electrical behavior of the neuron work in tandem to provide physiological integrity to the neuron. The future work therefore consists of coupling the mechanical response to the electrical behavior of the neurons. In Neurons, the mechano-chemo-electrical phenomena and their coupled emergent dynamics is critical to their physiological integrity and effectiveness. Therefore, future work will focus on improving the coupling of underlying mechanical response to the electrical behavior of the neurons. This will enable us to understand action potential modulation and potential disruption due to mechanical deformation. In support of this work, constitutive modeling of the viscoelastic response relevant to neuronal deformation is presented in the Appendix.

Chapter 2

Spatio-temporal modeling of saltatory conduction in neurons using Poisson-Nernst-Planck treatment and estimation of conduction velocity

This chapter is a published work:

Gulati, Rudraraju, "Spatio-temporal modeling of saltatory conduction in neurons using Poisson-Nernst-Planck treatment and estimation of conduction velocity", Brain Multiphysics, 2023.

2.1 Introduction

Electrical activity in nerve cells, enabled through the propagation of action potentials, is critical to the entire signaling and communication cascade of the nervous system. Disruption of this requisite signaling can lead to a number of neurological disorders such as the motor neuron diseases and is often linked with traumatic brain injury (TBI), Alzheimers, cognitive impairment, depression etc [2–6]. To gain insight into the neuronal electrophysiology, varied experimental investigations using the patch-clamp technique, electroencephalograms (EEG), electrocardiogram (ECG), MRI, calcium imaging, voltage imaging etc have been reported in literature. Despite the wealth of information achieved by these investigations, there is a need to supplement these studies with a robust numerical implementation which has the potential to represent the electrophysiology to a far greater resolution as recorded by the experiments.

Based on numerous voltage clamp experiments on the giant squid, Hodgkin-Huxley came up with a first mathematical model in the form of an electrical circuit to describe the current through the neuronal membrane [7]. They quantitatively detailed the respective ionic conductance in respect to the membrane voltage. Huxley delineated that the action potential propagation along the axon closely follows Ohm's law [8]. Using cable theory, they arrived at a one dimensional model of the action potential propagation. Based on the physiology of the neuron, the importance of myelin sheath that surrounds the axon, has been emphasized. Degradation of this protective covering for example with age can lead to slowdown of the signal or even signal disruption resulting in various diseases [9, 10]. To be able to study the effect of myelin on action potential propagation, the Hodgkin-Huxley model was modified to incorporate the myelin sheath and to obtain the single-cable model [11, 12]. Experimental investigation of the action potential by Barrett and Blight in the 1980's lead to the discovery of an after-potential [13–15]. With the advent of advanced microscopy techniques, the existence of a secondary electrical conduction pathway in the peri-axonal space under the myelin sheath has been uncovered [11].

The cable theory based models namely Hodgkin-Huxley, single-cable, double-cable, etc., have greatly contributed to our understanding of the neuronal electrophysiology. They provide us an excellent insight into the membrane potential, action potential propagation along the neuron, the electric current propagating along the axon, the effect of saltatory conduction due to the presence of myelin sheath, the effect of the submyelin peri-axonal space dictated by the double-cable model, the conduction velocity implied by each of these models etc. The cable theory based models, however, have some limitations. First, these are a one dimensional reduction of the complex heterogeneous spatial propagation of the action potential. Secondly, the cable theory based models fail to describe the underlying spatial ionic diffusion and the generated electric field during the electrical conduction propagation. Therefore, these models are not able to accurately describe the dynamics after a prolonged electrical activity or when the diameter is relatively smaller, as in the case of dendrites. Further, the cable theory based models cannot be easily extended to account for the membrane microenvironment, such as incorporating the membrane-glia interaction.

The Poisson-Nernst-Planck based electro-diffusive model has the capability to overcome the limitations of the cable theory based models and provide a spatio-temporal representation of the electrical potential along with the ionic distributions [16]. The PNP model is a more generalized model which can be reduced to the electroneutral model and can subsequently be reduced to the one dimensional cable theory based model [17]. Qian and Sejnowski modelled one of the first intracellular dynamics incorporating one dimensional PNP theory [18]. PNP model has also been applied to neuron-ECM-astrocyte interations [19]. Assuming electroneutrality, ionic dynamics have also been represented using Kirchoff-Nernst-Planck [20, 21]. However, the assumption of electroneutrality for nonuniform geometries is invalid [22]. Using PNP model, the neuronal intracellular-extracellular dynamics have been represented for a single node of Ranvier [22, 23]. It has been demonstrated that the dynamics of the PNP model resemble to that of the cable theory at higher ion channel density [22]. The PNP model can also be coupled with mechanics to represent the complex neuronal mechano-electrophysiology interactions [24–27].

In this work, we extend the electro-diffusive PNP model to multiple nodes of Ranvier, enhancing our ability to study the electrophysiology in a full length neuronal axon. We present novel variants of the PNP model based on the discrete cable theory based models, i.e. PNP model, PNP model with myelination, and PNP model with myelin and peri-axonal space. As an example, we demonstrate these models by simulating action potential conduction in a rat neuron. Spatial saltatory conduction due to the presence of myelin sheath and the peri-axonal space is demonstrated. Finally, we provide a detailed insight into the numerically estimated conduction velocity for a rat and squid neuron using various representative PNP electro-diffusive models. The Finite element (FE) method is used to discretize the set of PDEs underlying the PNP model. As suggested by an earlier work, non-homogeneous adaptive mesh is employed [23]. Results indicate that the conduction velocity (CV) of the action potential increases with the presence of myelin sheath and the peri-axonal space. The CV for the PNP with myelin is comparable to the single cable network but the CV for the PNP with myelin and peri-axonal space model does not increase drastically as compared to the double cable model. We observe that the action potential amplitude is lower for the PNP model when the myelin sheath is present.

In section 2.2, we briefly review and illustrate the well known models based on the one dimensional cable theory. The electro-diffusive PNP model is presented in section 2.3. The mathematical formulation of the numerical framework is elaborated in section 3.2.2. The simulation results of the various models of the PNP are detailed in section 3.3. Finally, a discussion of the conduction velocity for a rat and a squid neuron is in section 3.4, followed by conclusion in section 3.5.

2.2 Review of electrical network models of action potential propagation

2.2.1 Hodgkin-Huxley model

The classical work of Hodgkin and Huxley was a landmark model in terms of providing deep insights into the ionic basis of action potential propagation in nerve cells. Based on the voltage clamp experiments on the Giant Squid, the physiology of the initiation and propagation of action potential in a neuron was posed as a coupled set of ordinary differential equations. This electrical network model takes into account the membrane capacitance and the ionic currents due to the sodium ions, potassium ions and some leak current through the respective ion channels in the neuronal membrane. The influence of the conductance of the respective ion channels, or conversely the resistance, on the action potential was quantitatively estimated using experimental data. The resulting electrical circuit is depicted in Figure 2.1(A), and the corresponding governing equation linking the evolution of the membrane potential with the underlying ionic transport is the following:

$$C_m \frac{\partial V_m}{\partial t} + \bar{G}_{Na} m^3 h (V_m - E_{Na}) + \bar{G}_K n^4 (V_m - E_K) + G_L (V_m - V_{rest}) = I_{inj} \quad (2.1)$$

where C_m is the membrane capacitance of the lipid bilayer, V_m is the membrane potential, V_{rest} is the resting potential of the nerve cells and I_{inj} is the injected current through the voltage clamp experiments to initiate the action potential in the

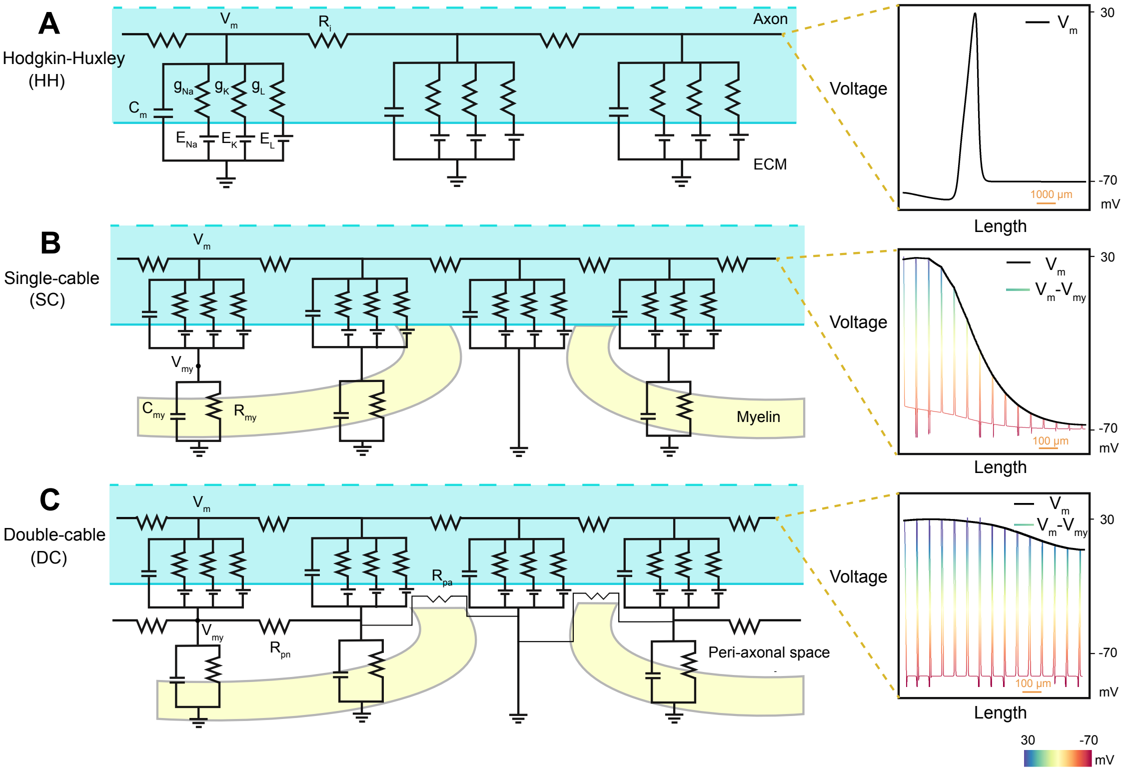

Figure 2.1: Electrical circuit of cable theory based models. (A) Schematics of cable theory based Hodgkin-Huxley circuit consists of membrane capacitance, resistance offered by the ion channels. Action potential propagates like a soliton through the axon and is depicted on the right. Extracellular voltage is taken as 0 mV. (B) Electrical circuit of the single-cable model considers the presence of myelin sheath. The capacitance and resistance offered by the myelin are explicitly modeled. (C) Electrical network of the double-cable representation incorporates an additional cable pathway for the submyelin peri-axonal space. Action potential jumps from one node of Ranvier to the next, resulting in a higher conduction velocity.

cell. $\bar{G}_i$ and E_i are the peak conductance and the Nernst potential of the sodium or potassium ions, and G_L is the conductance of the membrane leak channel.

Numerous experiments have pointed towards the effective behaviour of the intracellular region to that of a resistor along the axon [28]. Utilizing cable theory, one can then arrive at:

$$\frac{1}{R_i}\frac{\partial^2 V_m}{\partial x^2} = I_{inj} \tag{2.2}$$

where R_i is the resistance per unit length of the intra-cellular region along the axon. The partial differential equation (PDE) form of the Hodgkin-Huxley equation can then be written as:

$$C_m\frac{\partial V_m}{\partial t}+\bar{G}_{Na}m^3h(V_m-E_{Na})+\bar{G}_Kn^4(V_m-E_K)+G_m(V_m-V_{rest})=\frac{1}{R_i}\frac{\partial^2 V_m}{\partial x^2} \quad (2.3)$$

Using the above one-dimensional PDE, one can model the propagation of action potential along the length of the axon.

2.2.2 Single-cable model

From the physiology of nerve cells, it is well known that the glial cells provide a protective covering to the axonal membrane. This protective covering consists of multiple layers of myelin sheath along the axon, with gaps in between. These axonal gaps, void of any myelin covering, are identified as the nodes of Ranvier. These myelin lamellae play an indispensable role in the rapid movement of the action potential, since the direct ionic exchange with the extra-cellular medium occurs only at the nodes of Ranvier. This leads to a local current and the action potential jumping from one node of Ranvier to the next, more commonly referred to as *saltatory conduction.* The degradation of the myelin layers is known to lead to a decline in the conduction velocity and is also linked with various neuronal disease conditions [9, 10].

To accommodate this spatial heterogeneity of the myelin sheath, the standard Hodgkin-Huxley treatment needs to be altered to model myelinated-axons. A simple electrical circuit to realize this, known as the single-cable model, has been proposed [12, 29]. The ionic exchange between the intra-cellular regions and the extra-cellular regions takes place at the membrane, but only at the location of the nodes of Ranvier. As an example, for a rat axon, the span of the nodes of Ranvier is around $2.3\mu m$ and the nodes are separated by distance of $70\mu m - 100\mu m$ [11]. The single-cable model with the myelin sheaths having their respective capacitance and resistance is shown in Figure 2.1(B) [11].

2.2.3 Double-cable model

The presence of the submyelin peri-axonal region has been proposed as a potential pathway for rapid electrical conduction along the axon [11, 30]. Due to the presence of two conduction pathways, each modeled using cable theory, this treatment is referred to as the double-cable model. An electrical circuit representing such a double-cable model can be seen in Figure 2.1(C) . The basic governing equations for the electrical circuit at the node of Ranvier are similar to the set of equations from the single cable model/Hodgkin-Huxley model. In addition, using cable theory, the partial differential equation modeling the peri-axonal space takes the form:

$$\frac{1}{R_i}\frac{\partial^2 V_m}{\partial x^2} + \frac{1}{R_{pa}}\frac{\partial^2 V_{my}}{\partial x^2} = C_{my}\frac{\partial V_{my}}{\partial t} + \frac{V_{my}}{R_{my}} \tag{2.4}$$

where R_{pa} is the resistance per unit length in the peri-axonal space, C_{my} is the cumulative capacitance of the myelin sheath, R_{my} is the myelin resistance and V_{my} is the potential in the peri-axonal region.

2.2.4 Comparison of action potential profiles for electrical network models

The main results of this manuscript will be discussed in Section 3.3, but it is worthwhile to present here a brief comparison of the relative differences between the action potential (voltage) profiles predicted by modeling the electrical network models described above. Figure 2.1 presents such a comparison of the voltage profiles. All these plots were generated by solving the governing equations listed earlier in this section using an in-house 1D Finite Element Method implementation, and the model input parameters available in the literature for a giant squid axon [7] and rat axon [11] were used.

Shown as part of Figure 2.1(A) is a typical voltage profile predicted by the Hodgkin-Huxley model. The voltage profile is a single spike that propagates along the length of the axon, in this case from left to right. After the refractory period of the propagating spike, if a potential/current perturbation exceeding the threshold value is injected at the left boundary, then it would result in a voltage wave traveling with the same amplitude.

The voltage profile produced by a single-cable model is shown in Figure 2.1(B). As can be seen, the potential difference between the membrane potential and the myelin potential, ($\mathrm{V}_m - \mathrm{V}_{my}$) jumps across the nodes of Ranvier. This saltatory conduction leads to fast propagation of the voltage envelope, i.e. the membrane potential, which travels like a soliton-like wave. The decreased capacitance and increased resistance due to the myelin sheath enables this mode of propagation. In this simulation, the nodes of Ranvier are assumed to be equidistant. However, if the inter-nodal distance is varying along the length of an axon, it will lead to an axially varying conduction speed.

The voltage profile produced by a double-cable model, that incorporates a secondary conduction pathway, is shown in Figure 2.1(C). It can be observed that the profile of the voltage envelope is flatter than the voltage profiles predicted by the previous two models. Like in the case of the single-cable model, the action potential jumps from one node of Ranvier to the next, but through the peri-axonal space, and the propagation is relatively much faster. The peak amplitude is comparable to the peak amplitude for the Hodgkin-Huxley model and single-cable model.

2.3 A field theoretic model of action potential propagation

Cable theory based electrical network models have proven to be fundamental to our current understanding of the dynamics involved in action potential propagation. However, at the core, the network models are reduced order representations that try to capture the complex spatio-temporal variations of the ionic transport, voltage distribution, and most importantly the membrane structural heterogeneity into effective electrical properties like capacitance and resistance of the membrane and the channels. As mentioned in the introduction, a deeper investigation into spatial and temporal interactions of the ionic transport with the membrane microstructure (ion channel and pump distributions, myelin, glial environment, etc.) is desired, but the resulting coupled evolution of the voltage distributions becomes necessary when more complex phenomena like neuronal injury effects on action potential propagation [31–33], and conditions like neuronal hyperexcitability observed with Alzheimer's disease [34–36] are to be modeled.

An electro-diffusive framework for modeling spatio-temporal ionic charge distribution and the resulting voltage evolution using high-fidelity partial differential equations (PDE) modeling coupled electrostatics and electrochemistry can be capable of faithfully representing spatio-temporally heterogenous evolution of the ionic and voltage distributions leading to generation, propagation and potentially disruption

of the neuronal action potential. While not addressed in this current manuscript, such a capability to model spatial heterogeneity and membrane geometry-action potential interactions is evidently more important in the dendrites than the axons, due to the complex morphology of neuronal dendritic structures and synapses. We now propose a PDE based field theoretic implementation of the Poisson-Nerst-Planck (PNP) framework that can model 2D/3D ionic and voltage field distributions and their interactions with the membrane microstructure.
In this model, the transport of the respective ionic species, c_i, due to the corresponding diffusive and electromigration flux, $\boldsymbol{F}_i$, is modeled using the classical Nernst-Planck equation:

$$\frac{\partial c_i}{\partial t} = -\nabla \cdot \boldsymbol{F}_i \tag{2.5}$$

The ionic flux comprises of the diffusion term and the electro-migration term as presented in Eq. 2.6. Here D_i is the diffusion coefficient of the i^{th} ion, R is the gas constant, T is the temperature, F is the faraday constant and z_i is the valency of the i^{th} ionic species. It is to be noted that the cable theory based models only account for the electro-migration term i.e. the voltage gradient term. While the diffusion term may be neglected for axons with larger diameter, for finer geometries like dendrites, the diffusion term takes over the electro-migration term [18]. Hence, the PNP treatment has a higher-fidelity in representing the underlying action potential propagation. The total flux is given by:

$$\boldsymbol{F}_i = -[D_i(\nabla c_i + \frac{c_i F z_i}{RT} \nabla V)] \tag{2.6}$$

The coupling between the voltage and local ionic distribution is modeled with Poisson's equation [37], shown below.

$$-\nabla \cdot (\epsilon \nabla V) = F \sum_{i=1} z_i c_i \tag{2.7}$$

where ϵ is the permittivity of the medium. In this work, we consider three ionic species: Na^+, K^+ and Cl^-. The presence of an anion species ensures regulation of the required potential - for instance at the resting state. The sodium and potassium ions, as is well understood, depolarise and re-polarise the neuron. While the above PDE formulation by itself is well known, the novelty of its implementation in this work is from its application to model field variations and interactions in the presence of geometric heterogeneity of the nodes of Ranvier, myelin distribution, and the peri-axonal space.

Cable theory models as special cases of the general PNP framework

As advancements in high resolution imaging techniques lead to an improved understanding of the neuronal membrane microenvironment, various electrical network models incorporating the membrane spatial heterogeneity have been proposed over the years. Of these models, a primary classification in terms of increasing complexity of the membrane heterogeneity leads to the three treatments described above: Hodgkin-Huxley model, single-cable model and double-cable model. The PNP model is capable of representing the spatial heterogeneity of each of these models, and thus reproduce the action potential conduction profiles observed with these electrical network models. *To the best of our knowledge, numerical demonstration of this equivalence for each of these three models, and the extraction of equivalent 1D electrical network results (effective capacitance, effective resistance, action potential profile, etc.) from a more general electro-diffusion framework, has not been shown earlier in the literature.* Figure 2.2 depicts this equivalence between:

- PNP model and the classical Hodgkin-Huxley model,
- PNP model with myelination and the single-cable model,
- PNP model with myelin plus peri-axonal space and the double-cable model.

The axonal membrane has ion channels and the embedded membrane capacitance in the PNP model similar to the Hodgkin-Huxley model. The existence of the myelin sheath leads to the presence of nodes of Ranvier and decreased internodal capacitance in the PNP model with myelin. Note that there is no direct correlation of V_{my} as in the single cable model. Finally, the PNP model with myelin and peri-axonal space incorporates the sub-myelin peri-axonal space, leading to lower net resistance and faster propagation speed of the action potential. Here, the axial resistance and the peri-axonal resistance act in parallel, and hence the net axial resistance is lower. While the peri-axonal resistance does not correlate to the axial resistance in the double cable model, this is not the case for the equivalent PNP model as the resistance is computed using the underlying ionic constants. Here, the diffusion constants of the underlying ions in the peri-axonal space are assumed to be the same as in the cytoskeleton region.

Figure 2.2 also shows, as an overlaid line plot in each case, the 1D action potential profile (obtained as a line-out along the axonal axis from the 2D PNP simulations) for the three PNP model variants listed above. It can be noticed that the curvature of the voltage potential is lower when myelin is present as it leads to faster action potential propagation. Further, the presence of myelin leads to a lower action potential amplitude. This maybe due to the fact that the action potential jumps node to node as soon the threshold potential is attained.

2.4 Numerical implementation of the PNP model

The coupled nonlinear system of PDE's for ionic concentration and electrical potential in the electro-diffusive PNP model are solved using the standard Finite Element Method (FEM). The primal fields that are solved for are the voltage and the concentration of $Na^+/\ K^+/\ Cl^-$ ions. The electric field and the net charge are derived fields. The salient features of the computational implementation are: adaptive mesh refinement near the nodes of Ranvier, adaptive time-stepping schemes, support for parallel direct and iterative (Krylov-subspace) solvers with Jacobi/SOR preconditioning. The weak formulation of the governing equations solved with FEM are given in Section 2.4.1. The computational framework is made available to the wider research community as an open source library [38], and we hope it serves as a platform for wider adoption of the high-fidelity PNP framework by neuronal modeling researchers.

2.4.1 Weak formulation of the PNP model

The Nernst-Planck and Poisson equations, expressed in their weak (integral) formulation that is suitable for the FEM implementation, following standard notation, are as follows:

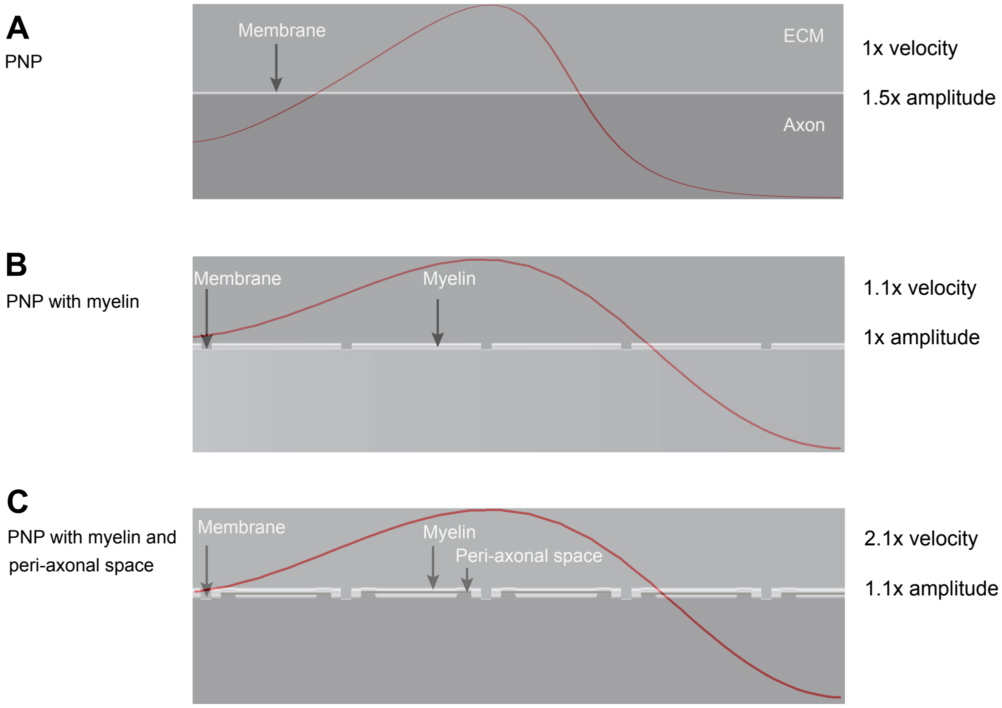

Figure 2.2: Schematic of adaptations of the PNP model based on various cable theory based models. Normalised profile of the action potential propagation computed in this work using the corresponding PNP model is depicted for the three variants: A) The PNP model comprises of ionic exchange between the intra-cellular and the extra-cellular region through the ionic channels present uniformly on the neuronal membrane. B) PNP with myelin model unifies the PNP model and the presence of myelin sheath. The ion channels are only present at the nodes of Ranvier. The low capacitance of the myelin sheath steers the action potential with higher velocity. C) The presence of the submyelin peri-axonal space is accounted for in the PNP model with myelin and submyelin peri-axonal space.

Find the primal fields $\{V, c_{Na}, c_K, c_{Cl}\}$, where,

$$V \in \mathscr{S}_V, \quad \mathscr{S}_V = \{V \ | V = \ \bar{V} \ \forall \ \mathbf{X} \in \Gamma_g^V\},$$
$$c_i \in \mathscr{S}_{c_i}, \quad \mathscr{S}_{c_i} = \{c_i \ | c_i = \ \bar{c}_i \ \forall \ \mathbf{X} \in \Gamma_g^{c_i}\}$$

and $i \in \{Na^+, K^+, Cl^-\}$, such that,

$$\forall\ w^V \in \mathscr{V}_V, \quad \mathscr{V}_V = \{V\ |V = \ 0\ \forall\ \mathbf{X} \in \Gamma_g^V\},$$
$$\forall\ w^{c_i} \in \mathscr{V}_{c_i}, \quad \mathscr{V}_{c_i} = \{c_i\ |c_i = \ 0\ \forall\ \mathbf{X} \in \Gamma_g^{c_i}\}$$

we have,

$$-\frac{F}{\epsilon}\int_\Omega w^V\ (c_{Na} + c_K - c_{Cl})\ dV + \int_\Omega \nabla w^V \cdot \nabla V\ dV - \int_{\Gamma_h^V} w^V\ (\nabla V \cdot \boldsymbol{n})\ dS = 0 \tag{2.8}$$

and,

$$\int_\Omega w^{c_i}\ \frac{\partial c_i}{\partial t}\ dV + \int_\Omega \nabla w^{c_i} \cdot D_i \nabla c_i\ dV + \int_\Omega \nabla w^{c_i} \cdot D_i \frac{c_i z_i F}{RT} \nabla V\ dV + \int_{\Gamma_h^V} w^{c_i}\ (\boldsymbol{F}_i \cdot \boldsymbol{n})\ dS = 0 \tag{2.9}$$

where w^V is the variation for the voltage field, w^{c_i} are the variations for the ionic fields. Ω is the problem geometry, $\{\Gamma_g^V, \Gamma_g^{c_i}\}$ are the Dirichlet boundaries and $\{\Gamma_h^V, \Gamma_h^{c_i}\}$ are the Neumann (Flux) boundaries of the voltage and ionic fields, respectively. $\boldsymbol{n}$ is the unit normal vector . In this work, there is no voltage flux ($\nabla V \cdot \boldsymbol{n} = 0$) at all the boundaries. Eq. 2.9 and Eq. 2.8 are the governing equations solved using FEM.

The PNP framework models the evolution of the voltage field and the ionic concentrations of Na^+, K^+ and Cl^-. The initial ionic concentrations in the various regions such as the extra-cellular region, membrane, myelin, cytoskeleton, etc., are mentioned in the Supplemental Information. The initial voltage in the ECM is taken to be 0 mV and in the cytoskeleton region to be the resting value of -70 mV. The boundary conditions on the top and bottom surface of the domain are applied so that the fields, i.e. voltage and the ionic concentrations, represent their bulk value in the extra-cellular region as in Eq. 3.1. The ionic exchange at the nodes of Ranvier is incorporated as an ionic flux as given by Eq. 3.2. Here I_i is the current of each ionic concentration computed using their respective Hodgkin-Huxley ionic conductance.

At top and bottom boundaries;

$$c_i = c_i^e, \qquad V = 0 \tag{2.10}$$

At the Node of Ranvier:

$$\boldsymbol{F}_i \cdot \boldsymbol{n} = f_i, \qquad f_i = \frac{I_i}{z_i F} \tag{2.11}$$

where,

$$I_{Na} = \bar{G}_{Na} m^3 h (V_m - E_{Na})$$

$$I_K = \bar{G}_K n^4 (V_m - E_K)$$

$$I_{Cl} = 0$$

2.4.2 Estimating effective electrical properties from ionic distributions

In order to compare the action potential propagation modelled using the cable theory and the PNP model, the embedded electrical properties of the PNP model should be the same as the input values of the cable theory based models. The capacitance of the PNP model can be computed using the membrane thickness and myelin thickness to obtain C_m and C_{my}, respectively. The axial resistance offered to the conduction can be computed using the ionic constants as presented in Figure 2.3. Initially, the membrane potential is at its resting value of -70 mV with higher concentration of sodium ions in the extracellular region and a higher concentration of potassium ions in the intra-cellular region. The model is first equilibrated for a few timesteps until there are no fluctuations in the field variables. Next, to initiate the action potential, we assume a sodium ion influx in a region of length $5\mu m$ near the left end of the neuronal membrane until the local potential reaches the threshold potential. Thereafter, the activation parameters regulate the depolarization/repolarization.

2.5 Results

This section seeks to establish the significance of the PNP numerical framework by analyzing the results of the three variants of the electro-diffusive model discussed in the preceding sections. First and foremost, an unmyelinated PNP model for a squid axon is investigated and distinctions with the cable theory based Hodgkin-Huxley model are probed. Subsequently, the simulation results for the PNP with

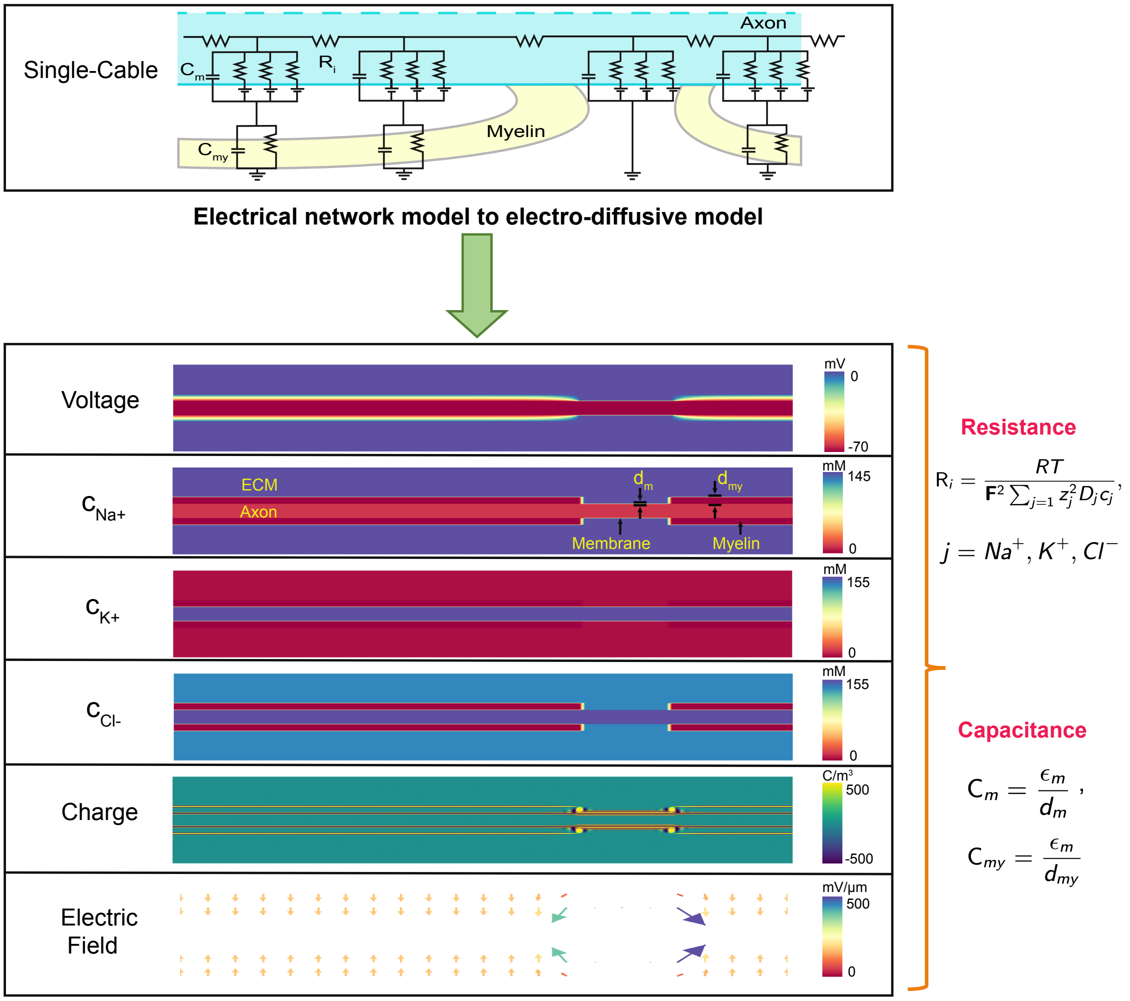

Figure 2.3: Electrical connection between the cable theory based model and the Poisson-Nernst-Planck model. The spatial electro-diffusive PNP model comprises of multiple fields including the voltage and the concentration of the respective ions. The capacitance of the membrane and the myelin sheath are embedded in the PNP model in the form of membrane/myelin thickness. The ion channel currents are treated as a flux (Neumann boundary condition) in the spatial model. The resistance offered to the action potential along the axon can be computed using the ionic constants and the expression given in the figure. The derived fields namely, the electric field and net charge are also plotted. Note that the plot of electric field is zoomed in around the membrane as there is no appreciable electric field in the ECM.

myelin and PNP with myelin plus peri-axonal space model are carefully studied and a detailed comparison with the corresponding cable theory based model is presented. Neuronal axons of a rat and squid are considered for the numerical simulations. The parameters of the respective axons are collected from [7, 11, 22, 23] and are listed in the Supplemental Information.

2.5.1 PNP model

Figure 2.4 compares the action potential resulting from the cable theory based Hodgkin-Huxley model to the PNP model. For this simulation, the neuronal axon of a squid having a length of $20,000$ μm, a radius of 238 μm, and a rat neuron having a length of 1500 μm, a diameter of 1.1 μm are considered. Note that a larger length for the squid axon is selected so that we can clearly observe the propagation profile of the action potential in the simulations. From the plots, we can clearly visualize that the one-dimensional lineout of the spatial voltage resulting from the PNP model is similar to the voltage from the cable theory based Hodgkin-Huxley model. The charge is accumulated near the membrane due to the property of the membrane to act as a capacitor. This leads to the formation of the Debye layer near to the membrane. As reflected from the plot of net charge, the variation of ionic concentration is appreciable near the membrane. The electric field is prominent throughout the membrane due to the potential difference between the intracellular and the extracellular region, however, the magnitude of this electric field varies with the propagation of the action potential along the axon. The initial equivalent resistance offered to the action potential propagation along the squid axon is computed to be 38.18 Ω cm using the underlying ionic constants. The conduction velocity for the squid and the rat axon is computed to be 15.38 m/s and 0.36 m/s respectively.

2.5.2 PNP model with myelin

The action potential and the respective ionic concentrations modeled using the PNP with myelination model are presented in Figure 2.5. The one-dimensional lineout of the primary fields is plotted on the right. We observe that the action potential propagates as a soliton-like wave as in the single-cable model. While the saltatory conduction observed in the single-cable model is due to the potential jump from one node of Ranvier to the next, the saltatory conduction in the electro-diffusive model is observed in the respective ionic concentrations. As in the single-cable model, the saltatory conduction is due to the presence of nodes of Ranvier, and therefore the myelin sheath. Low capacitance of the myelin sheath which quickly charges and discharges, leads to fast propagation of the charge. The envelope of the one-dimensional lineout of the respective ionic concentration propagates with the action potential. We also note that there is no correlation of the myelin voltage in the electrodiffusive model as in the single cable model. The electric field, prominent at the nodes of Ranvier and the membrane is also depicted. As in the previous model, the accumulation of the net charge closer to the membrane can be observed.

Here, we discuss the mechanism of action potential propagation using the PNP electrodiffusive model. As compared to the bulk, the net charge is considerable near the membrane due to the membrane capacitance. This leads to lower net resistance in the intra-cellular region near the membrane. To initiate the action potential, there is sodium ion influx from the first node of Ranvier. The high electric field/ high voltage gradient at this node of Ranvier steers the charge to propagate at a faster velocity along the membrane as this offers a low resistance conduction path. These ions reach the adjacent node of Ranvier, resulting in the membrane potential attaining the threshold potential. At this point, the Hodgkin-Huxley activation/inactivation parameters govern the ionic flux and the propagation of action potential along the entire length of the axon. One must realize that the ionic diffusion is immensely slow but the combination of high voltage gradient/electric field at the respective nodes of Ranvier, the ionic flux through the membrane leads to the local current and thus faster propagation of the action potential along the axon. This ability of the PNP framework to model the electric field and net charge, in addition to the action potential and the ionic distributions, make it a high-fidelity and more comprehensive model compared to the cable theory models.

2.5.3 PNP model with myelin and peri-axonal space

The propagation of the action potential using the PNP model with myelin and peri-axonal space is depicted in Figure 2.6. The profile of the action potential propagation is similar to the earlier presented PNP model. However, the one-dimensional lineout plot of the respective ionic concentration depicts a lot of surges due to the presence of the peri-axonal space in addition to the nodes of Ranvier. The envelope of the sodium ion concentration propagates with the action potential. However, the envelope of the potassium and the chloride ion travel relatively fast with respect to the action potential. Again, we can visualize the spatial saltatory conduction from the respective ionic concentration which jumps from one node of Ranvier to the next. As in the previous PNP model, we note the lower amplitude of action potential propagation, the dominant electric field at the nodes of Ranvier, and the accumulation of net charge near the membrane. Note that the magnitude of the electric field varies with the neuronal conduction along the axon. Simulation video of the myelinated PNP models showing the spatio-temporal evolution of all the fields is provided as part of the Supplemental Information.

2.5.4 Spatial resolution of the primal fields

Based on the simulation results presented in the previous sections, one can appreciate the potential of the PNP framework to augment the voltage imaging experiments where the neuron is stained with a voltage-sensitive or ion-sensitive dye to carry out an analysis of the action potential propagation and its properties such as conduction velocity. Figure 2.7 demonstrates the capability of the PNP framework to determine the voltage fields and the respective ionic concentration to a fine resolution. This fine resolution is important, as it's the small variations in the respective ionic concentrations that eventually result in the quintessential propagation of the action potential. At any point P in the domain, one can visualize the temporal variation of the respective primary or derived fields. Thus, in addition to the voltage imaging experiments, this model can potentially act as a digital twin for the patch-clamp/voltage-clamp experiments where the profile of the voltage or the current is plotted at a specific point in the neuron where the electrode is inserted.

2.6 Discussion on estimated velocity of action potential propagation

The conduction velocity for a rat axon computed using the various cable theory based models and the PNP models are compared in Figure 2.8a. For each of the models based on cable theory or PNP, the conduction velocity increases due to myelination or the presence of submyelin peri-axonal space. While the conduction velocity computed using the PNP and the PNP with myelin are in close proximity to that computed from the classical Hodgkin-Huxley and the single-cable model respectively, the double cable model has nearly a nine fold increase in the speed

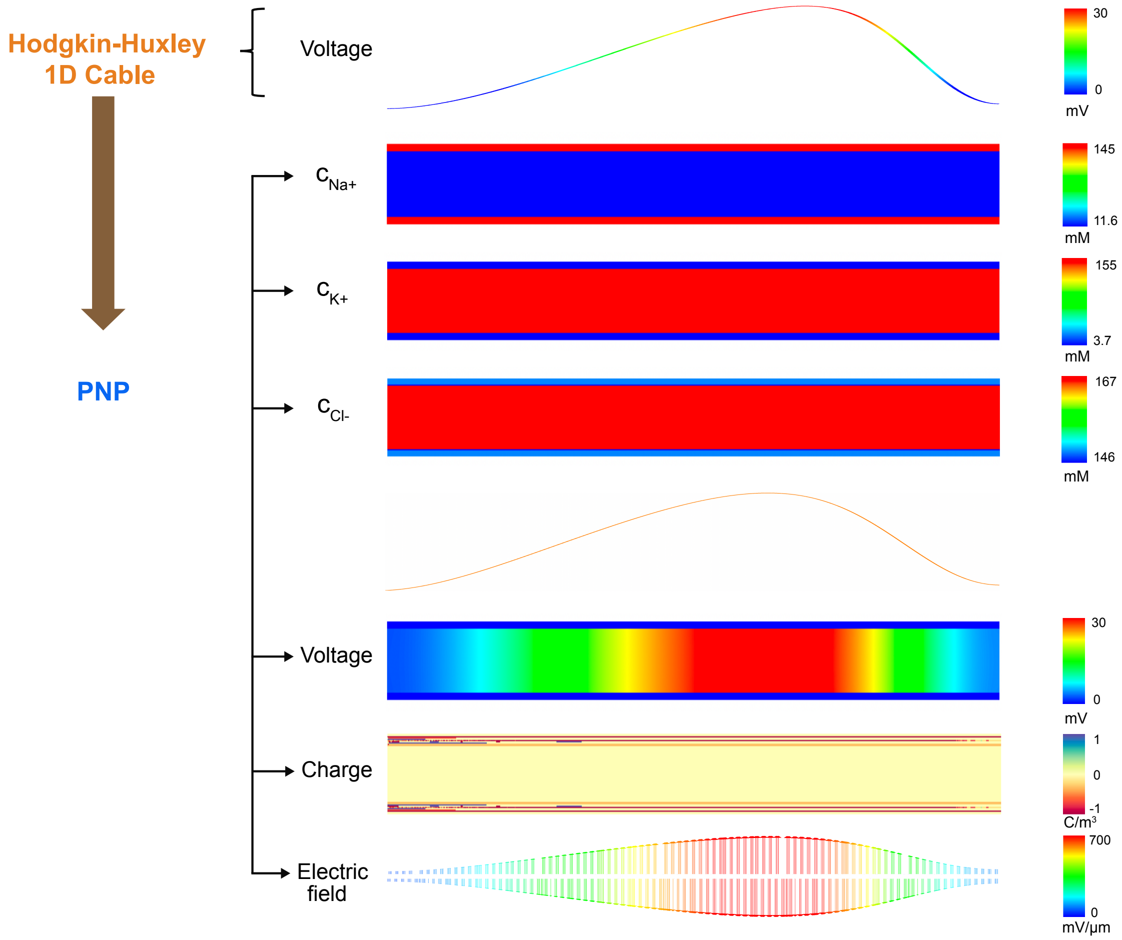

Figure 2.4: Comparison of the cable theory based Hodgkin-Huxley to the PNP model for a squid axon. The models have identical inputs of the membrane capacitance and resistance. The schematics depict the capability of the PNP model to visualize the spatial distribution of the voltage, ionic concentration, net charge and the electric field. Net charge and electric field are dominant at the membrane. The profile of the one dimensional lineout of the action potential propagation from the PNP model resembles to the action potential propagation modelled using the cable theory based classical Hodgkin-Huxley model.

compared to the PNP model with myelin and periaxonal space. This may be due to the fact that, while the double-cable model employs the peri-axonal resistance and the para-nodal resistance, these values for the PNP model depend on the underlying ionic constants and are therefore of the same order of magnitude as in the axonal cytoplasm. It has been assumed that the ionic diffusion coefficient is the same in the cytoskeleton of the neuronal axon and the sub-myelin peri-axonal space which may not be the case. However, once these values are obtained experimentally, we

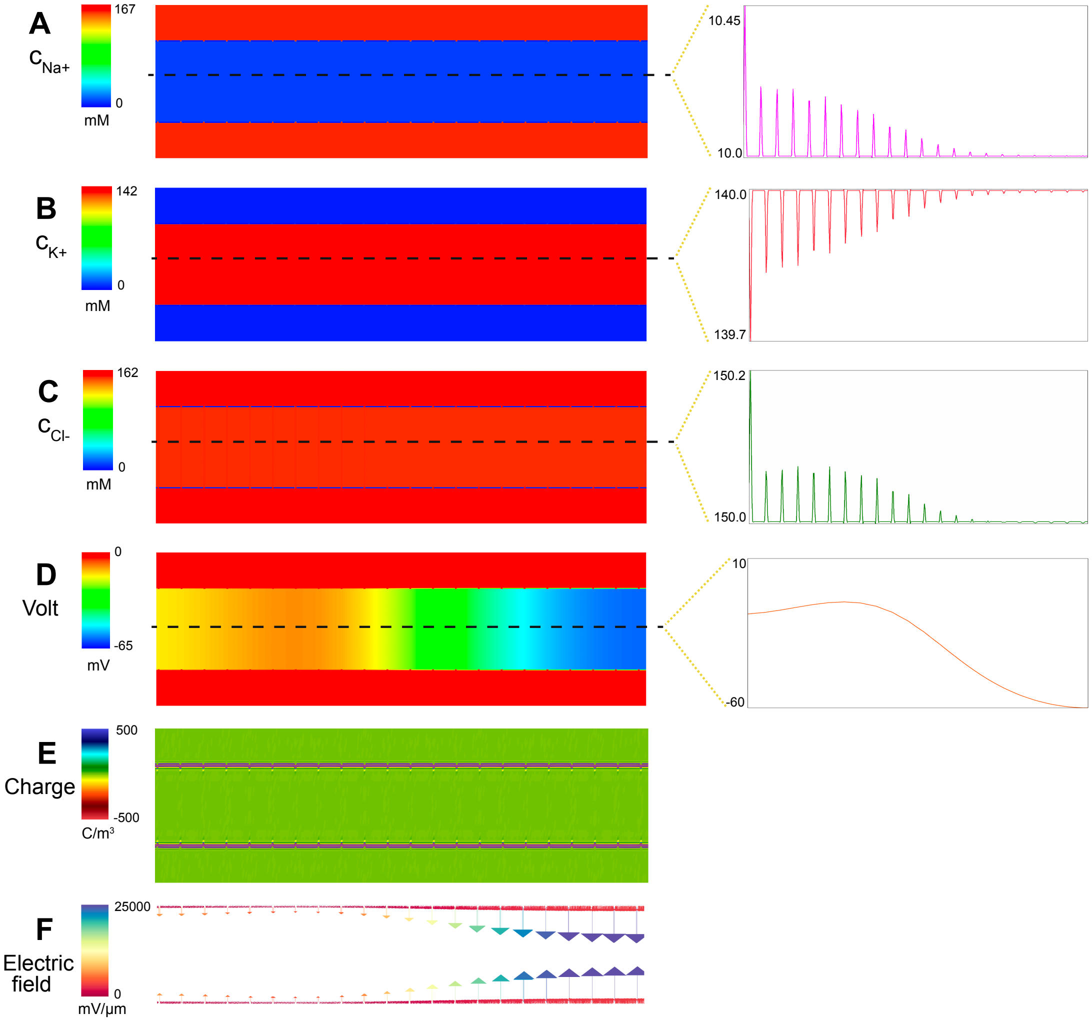

Figure 2.5: Schematics of the various fields modelled using the PNP model with myelin for a rat axon. A lineout of the one dimensional profile of the primary fields extracted from the spatial PNP model is depicted in the right. The action potential propagates as a soliton-like wave as in the HH model. The ionic concentrations depict a saltatory conduction where it appears that the concentration jumps from one node of Ranvier to another. This is unlike the saltatory conduction observed using the one dimensional single-cable model. This is observed for all the ionic species present. Net charge is accumulated near the membrane. Electric field is dominant at the nodes of Ranvier.

can easily incorporate this in the PNP framework. The slight difference in the conduction velocity computed using the PNP model, PNP with myelin model as compared to the cable theory based Hodgkin-Huxley, single cable model is discussed next. Initially the equivalent axial resistance of the PNP model is comparable to the

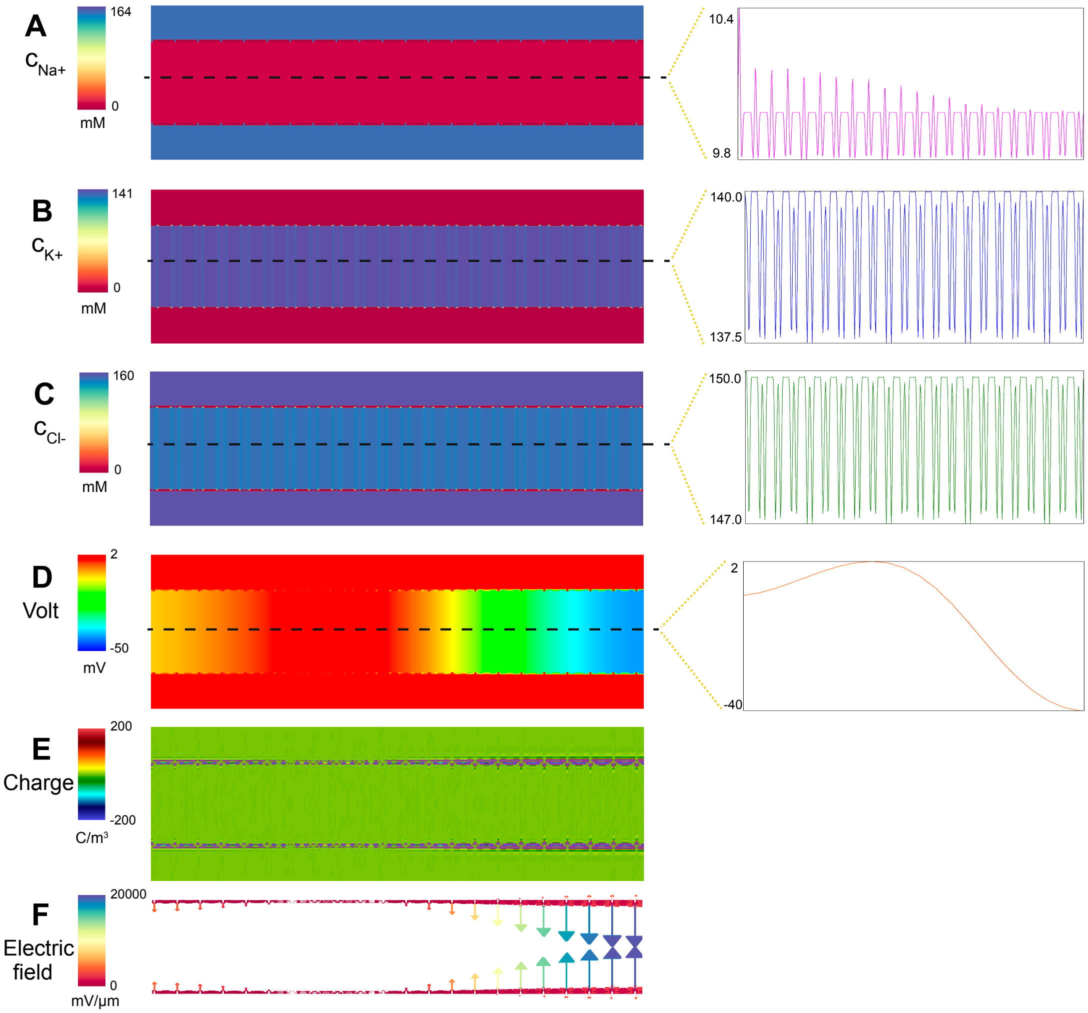

Figure 2.6: Schematics of the fields modelled using the PNP model with myelin and periaxonal space for a rat axon. A lineout of the one dimensional profile of the primary fields extracted from the spatial PNP model is depicted in the right. The profile of the action potential is similar to earlier models. As in the PNP with myelin model, the ionic concentrations depict a saltatory conduction jumping from one node from Ranvier to the next. However, this conduction is faster here as compared to the PNP with myelin model.

cable theory based model. With the propagation of action potential and because of the nature of the membrane to act as a capacitor, the net charge is appreciable near the membrane in the intracellular region. This leads to lower net resistance near the membrane in the PNP models and the differences in the conduction velocity when compared to their corresponding cable theory based model.

For a squid, there is a two fold increase in the computed conduction velocity

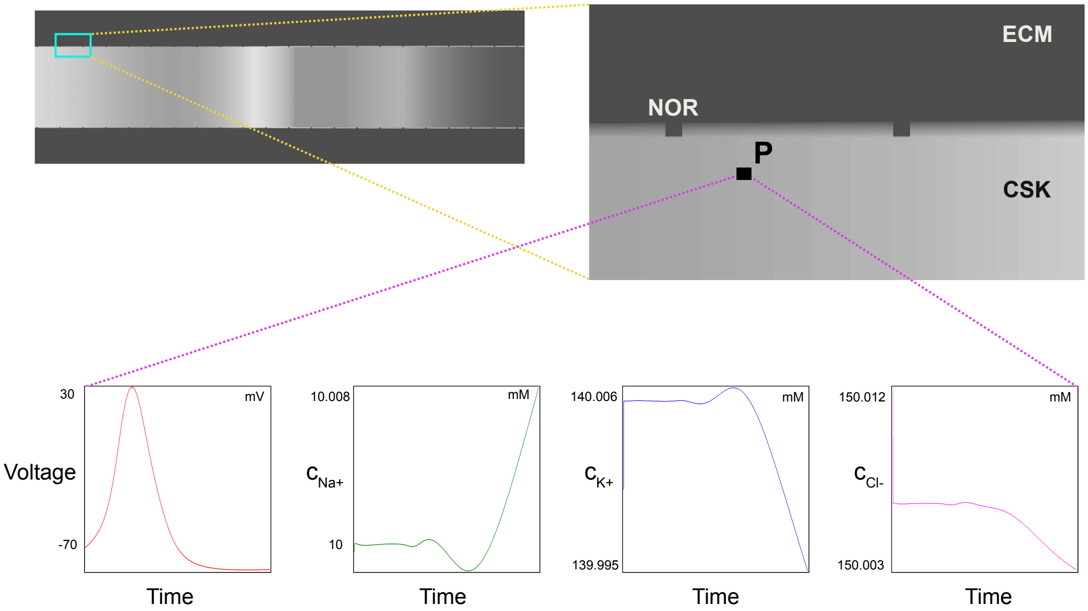

Figure 2.7: Spatial resolution of the primary and derived fields in the PNP with myelin model of a rat axon. The framework of the PNP based models can provide insight into the various spatial fields present at a material point on the neuronal membrane or its vicinity. The time evolution of various field values at a point ‘P’ in the intra-cellular region is depicted in the plots.

when the electro-diffusive model includes myelination. The conduction speed of the Hodgkin-Huxley model is close to the value computed using the PNP model. The primary difference in neuronal conduction velocity of a squid and a rat is due to the larger diameter of the squid axon. The net axial resistance in the rat axon is therefore relatively higher.

2.7 Conclusion

Cable theory based Hodgkin-Huxley, single-cable and double cable models have been extensively used to model the action potential propagation along the neuron. These models are essentially a one dimensional reduced order representation of the complex action potential dynamics, and ignore the spatial ionic diffusion which can be crucial to study propagation in non-trivial geometries and in the heterogeneous neuronal microenvironment, such as in action potential propagating through thin dimensions in dendrites, and of multiple action potentials. The Poisson-Nernst-Planck model

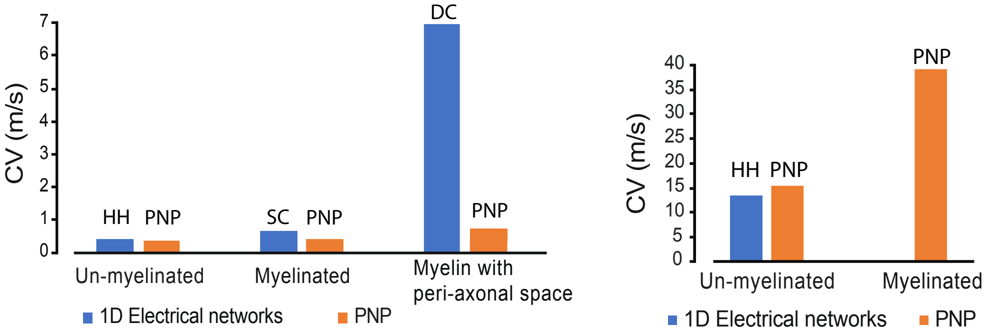

(a)

(b)

Figure 2.8: Estimated conduction velocity (CV) of action potential propagation. (a) Numerical estimates of the CV of the action potential propagating through the rat neuron modeled using variants of cable theory and PNP based models. Using the cable theory based models, the CV increases due to the presence of the myelin sheath and the peri-axonal space. The same trend is observed for the PNP models but the increase in the conduction speed when the peri-axonal space is present in the PNP model, is comparatively lower than the double-cable model. (b) CV for the action potential propagating through the squid neuron modeled using cable theory and PNP models. The increase in the CV is significant when myelin is present. Here, HH, SC, and DC abbreviations are used for the Hodgkin-Huxley, Single-Cable, and Double-Cable models, respectively, to distinguish between the three 1D electrical network models.

provides a robust framework to represent the action potential propagation due to the spatio-temporal variation of the ionic concentrations at a much finer resolution. Also, the derived fields, such as the electric field and the net charge, can be easily obtained and analyzed. Moreover, as shown in this work, this model is able to emulate the various variants of the cable theory based models. This framework can also be extended to model the heterogeneous microenvironment around the neuronal membrane, such as the neuron-glia interactions.

To the best of our knowledge, the framework presented here for numerically estimating the conduction velocity of the spatial action potential propagating using the PNP model, is a first-of-its-kind. Further, the spatio-temporal manifestation of the well-known saltatory conduction mechanism has been demonstrated. This electro-diffusive PNP framework can augment experiments to yield an elevated understanding of the action potential propagation, and thus assisting us to get a better insight into the functioning of our neurophysiology, and into the action potential related underpinnings of various neurological diseases.

Chapter 3

Electro-diffusive modeling and the role of spine geometry on action potential propagation in neuronal dendrites

3.1 Introduction

The brain, a complex structure, has the neuron as its fundamental building block. The primary role of the neuron is to smoothly transmit the electrical signals also known as the action potential. The understanding of the propagation of this action potential is critical to understand the functioning of the brain, the disruption of which can lead to neurological disorders and a number of diseases such as, Alzheimers, traumatic brain injury etc [2–4, 6, 35]. The primary mechanism of the inter-neuronal electrical transmission is through the release of neurotransmitter by the pre-synaptic neuron which activates the receptors on the post-synaptic neuron. The excitatory synaptic potential is thus initiated at the dendritic spines, accumulated at the axon hillock until the threshold is attained leading to the firing of the all-or-none action potential along the axon. Besides the role of the different components of the neuron, such as the spine, the dendritic shaft, the axon hillock and the axon, the transmission is aided by the rich ion channel density and the receptor density present on the neuronal membrane.

The neuron consists of thousands of dendritic spines, which are the narrow protrusions on the dendritic shaft. The spines were discovered more than a century ago and their importance as the principal site for excitatory synaptic input was established. The neurotransmitter receptors present on the spine are activated once the neurotransmitter binds onto them leading to the influx of excitatory input in the form of synaptic current. It has also been contested that the geometry of the spine plays a paramount role in regulating the synaptic potential and therefore in synaptic plasticity. Experimental investigation of the spines has been challenging due to difficulty in accessing them owing to their small size. Numerical modeling in the form of cable theory has been widely applied to understand the fundamentals of the electrical propagation but it was realized that this theory breaks down for thin compartments as the spine [18]. The Poisson and Nernst-Planck equations consider the coupling of the electric field to the ionic flow and provide a high-fidelity capability to model the rich spatio-temporal propagation of the action potential. Recently, dendritic spines have been numerically modeled using the PNP electrodiffusive equations. Coarse grained PNP equations are modeled by [39], PNP equations under electroneutrality assumption is considered by [40], PNP equations are modeled by [41]. [39, 41] emphasize the role of the spine geometry on potential induced at the soma by the synaptic input at the spine. It is also to be noted that their numerical models do not include the ion channels on the spine as they do not play a prominent role during excitatory synaptic input [42].

Recently, super-resolution imaging techniques and fluorescent voltage dyes have enabled the visualization of the potential in the spines [43]. The effect of attenuation of the excitatory synaptic input from the spine to the soma has been studied by [41, 42, 44–48]. Spines with longer neck or lesser radius are electrically silent at the soma. [48, 49] have predicted biochemical compartmentalization at the spine heads due to the high diffusional resistance offered by the spine neck. Effect of backpropagating action potential in spines has been closely observed by [42, 44–46]. It has been inferred that the back-propagation leads to high potential in the spines and the role of the ion channels in the spines is not as prominent during the excitatory synaptic input. There is a high density of potassium ion channels in the dendrites which ensures that the action potential does not initiate in the dendrite [50]. It has also been observed that there is a high density of sodium ion channels in the axon hillock that results in attaining the threshold potential in the hillock region [51]. With the rising capability of the experimental investigation of the spine biophysics, it has become obligatory for the numerical models to faithfully supplement them and act as their digital twin.

Once the voltage threshold is attained at the axon hillock, it leads to the propagation of action potential in the axon. Neuronal axon electrophysiology has been studied through varied experimental investigations such as patch-clamp technique, electroencephalograms (EEG), electrocardiogram (ECG), MRI, voltage imaging etc which have consequently provided immense details of the voltage profile, conduction speed etc. Hodgkin-Huxley based cable theory provided a first mathematical basis to model the electrical transmission in the axon [7, 28]. With advanced imaging techniques, the presence of myelin sheath and the peri-axonal space have lead to the single-cable and double-cable models [11]. The cable theory based models have a number of limitations and this lead to the electro-diffusive PNP modeling [16, 18]. Both the unmyelinated and the myelinated case have been modeled for a single node of ranvier [22, 23]. A first complete model of propagation of action potential along the myelinated neuronal axon consisting of multiple nodes of Ranvier using PNP was demonstrated by [52] which has immense capability to act as a digital twin for the electrophysiological experiments.

Currently, the numerical models of action potential propagation using PNP are limited to a spine only or the axon only propagation. With the advancements of the experimental investigations into the spine, there is a requirement of an integrated numerical model that demonstrates propagation of the electrical signaling starting from the spine and propagating to the axon through the dendritic shaft and the soma region. This unified model can aid the experimental findings and provide insights to a far greater resolution. In this work, we extend our previous work [52] to include the spine, dendrite and the soma region to model the action potential propagation in the complete neuronal geometry. To our knowledge, this is the first integrated model which is based on the Poisson-Nernst-Planck equations. It is to be noted that there are full neuronal scale numerical models that exist in literature but they are based on the cable theory which is inaccurate for small compartments as the dendritic spine [44, 48, 53]. We demonstrate the initiation and propagation of action potential in the neuron, namely, the forward propagation along the axon and the back propagation into the spines. The effect of spine geometry on voltage attenuation at the soma is also studied. It is believed that spines modify their geometry and play an essential role in synaptic plasticity. This model can also be coupled with mechanics to represent the complex neuronal mechano-electrophysiological interactions [27].

3.2 Methods

3.2.1 Numerical representation of dendritic structure and synaptic interface

As discussed in the introduction, the synaptic current at the synapse plays a vital role in the healthy propagation of the inter-neuronal electrical signaling. Electrodiffusion of neurotransmitters, the receptor's capability to capture the neurotransmitters are an important part of the mechanism. While the model discussed can be extended to multi-neuronal cluster, here, we focus on a single neuron to get a detailed insight. We use finite element method to solve the PNP set of equations. To simplify the geometry, we approximate the neuronal geometry using straight lines instead of curved lines so that the focus is not on the geometry. Fig. 3.1 depicts the schematics of the neuron with a simplified geometry under investigation using the FE method. To initiate the action potential in this single neuron model, we assume that once the neurotransmitter released by the pre-synaptic neuron is captured by the receptors residing on the spine head of the post-synaptic neuron, it leads to sodium ion influx. This leads to the voltage buildup at the axon hillock region leading to the firing of the action potential once the threshold potential is attained. There are Hodgkin-Huxley based Na^+, K^+ ion channels on the dendritic shaft, the soma and the axon neuronal membrane. Besides these, some leak K^+ ion channels are also present on the dendrite which ensure that the potential threshold is not attained in the dendrite region. There is a high density of ion channel density in the axon hillock region which ensures the propagation of the action potential. The myelin sheath leads to the presence of nodes of Ranvier region on the axon which consist of ion channels.

3.2.2 Numerical implementation of the PNP model

The coupled nonlinear system of PDE's for ionic concentration and electrical potential in the electro-diffusive PNP model are solved using the standard Finite Ele-

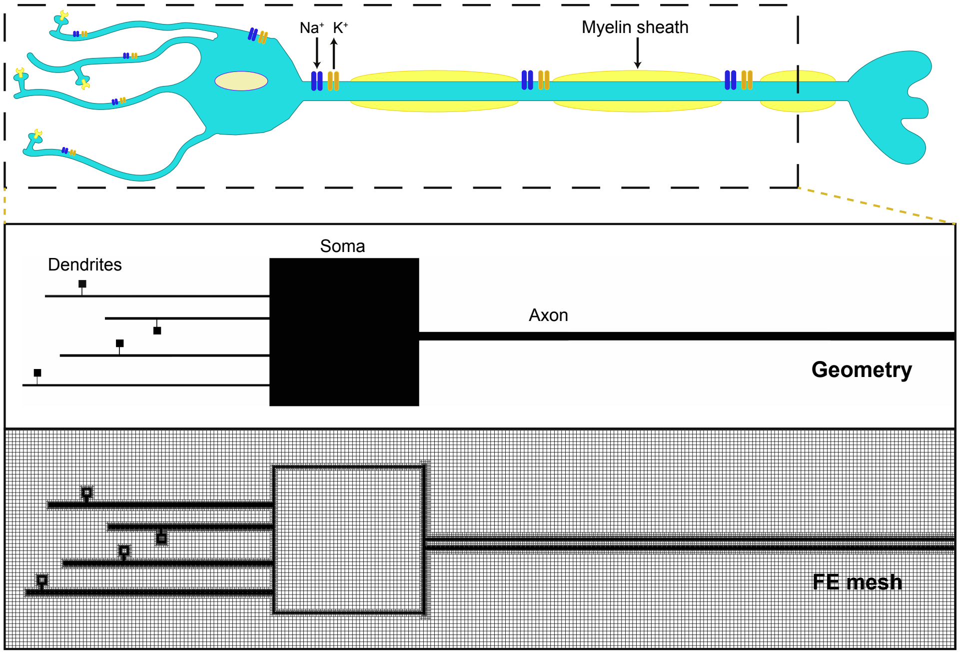

Figure 3.1: The schematics of a simplified neuron geometry with respect to the electrophysiological modeling. The receptors in the spine head form the primary site of the synaptic input which leads the potential to flow through the spine neck, the dendritic shaft, the soma to the axon hillock where it accumulates until the threshold is attained and leading to the firing of this action potential along the axon. The myelin sheath adds to the faster propagation of this potential via spatio-temporal saltatory conduction. The geometry and the mesh used to represent the neuronal geometry for the finite element method are also presented.

ment Method (FEM). The primal fields that are solved for are the voltage and the concentration of Na^+/ K^+/ Cl^- ions. The weak formulation of the governing equations solved with FEM were provided in the previous chapter. The computational framework is made available to the wider research community as an open source library [38], and we hope it serves as a platform for wider adoption of the high-fidelity PNP framework by neuronal modeling researchers.

The PNP framework models the evolution of the voltage field and the ionic concentrations of Na^+, K^+ and Cl^-. The initial ionic concentrations in the various regions such as the extra-cellular region, membrane, myelin, cytoskeleton, etc., are mentioned in the Supplemental Information. The initial voltage in the ECM is taken to be 0 mV and in the cytoskeleton region to be the resting value of -70 mV. The boundary conditions on the top and bottom surface of the domain are applied so that the fields, i.e. voltage and the ionic concentrations, represent their bulk value in the extra-cellular region as in Eq. 3.1. The ionic exchange at the nodes of Ranvier is incorporated as an ionic flux as given by Eq. 3.2. Here I_i is the current of each ionic concentration computed using their respective Hodgkin-Huxley ionic conductance.

At top and bottom boundaries;

$$c_i = c_i^e, \qquad V = 0 \tag{3.1}$$

At the Node of Ranvier:

$$\boldsymbol{F}_i \cdot \boldsymbol{n} = f_i, \qquad f_i = \frac{I_i}{z_i F} \tag{3.2}$$

where,

$$I_{Na} = \bar{G}_{Na} m^3 h (V_m - E_{Na})$$

$$I_K = \bar{G}_K n^4 (V_m - E_K)$$

$$I_{Cl} = 0$$

The following expression for the leak current in the dendrite is adopted.

$$I_K^{leak} = g_K^{leak} (V - E_K) \tag{3.3}$$

Model parameters

Initially, the membrane potential is at its resting value of -70 mV with higher concentration of sodium ions in the extracellular region and a higher concentration of potassium ions in the intra-cellular region. The model is first equilibrated for a few timesteps until there are no fluctuations in the field variables. The geometrical, electrical and ionic parameters of the model are listed in Table 3.1, 3.2 and 3.3.

Table 3.1: Constants used in the electro-diffusive numerical framework.

Parameter	**Value**	**Description**
R	$8.31454\ J \cdot mole^{-1} \cdot K^{-1}$	Gas constant
T	$279.45\ K$	Temperature
F	$96485\ C \cdot mole^{-1}$	Faraday constant
D_{Na}	$1.33\ \mu m^2 \cdot ms^{-1}$	Diffusion coefficient of sodium ion
D_K	$1.96\ \mu m^2 \cdot ms^{-1}$	Diffusion coefficient of potassium ion
D_{Cl}	$2.0\ \mu m^2 \cdot ms^{-1}$	Diffusion coefficient of chloride ion
ϵ_o	$8.88541\ e^{-12} C \cdot m^{-1} \cdot V^{-1}$	Electric permittivity in vacuum
ϵ_w	80.0	Relative dielectric permittivity of water
g_{Na}	$120\ mS/cm^2$	peak conductance of Na^+
g_K	$36\ mS/cm^2$	peak conductance of K^+
g_{Na}^{leak}	$0.05\ mS/cm^2$	leak conductance of Na^+
g_K^{leak}	$0.5\ mS/cm^2$	leak conductance of K^+
c_{Na}^i	$10\ mM$	Initial intracellular concentration of Na^+
c_K^i	$140\ mM$	Initial intracellular concentration of K^+
c_{Cl}^i	slightly exceeds $150\ mM$	Initial intracellular concentration of Cl^-
c_{Na}^e	$155\ mM$	Initial extracellular concentration of Na^+
c_K^e	$3.5\ mM$	Initial extracellular concentration of K^+
c_{Cl}^e	$158.5\ mM$	Initial extracellular concentration of Cl^-

3.3 Results

This section seeks to establish the significance of the PNP numerical framework by analyzing the results of the initiation and forward / backward propagation of action potential in the neuronal geometry. First and foremost, the synaptic current is input at a single spine head leading to the initiation of the axon potential at the axon hillock and propagating along the axon. Subsequently, the effect of geometry of the spine and the dendritic shaft are carefully studied and detailed insights are presented. Finally, we consider the case of synaptic input at multiple spine heads and present an exhaustive comparison with the corresponding case of input at a single spine head. Neuron of a rat with myelinated axon is considered for the numerical simulations. The parameters of the axon are collected from [7, 11, 22, 23, 52].

Table 3.2: **Geometric properties of the neuron studied for the action potential propagation using the PNP model.**

Parameter	**Value**
Spine head dimension	1.0 μm*1.0 μm
Spine neck length	1.0 μm
Spine neck diameter	0.1 μm
Dendritic shaft diameter	0.3 μm
Distance of Spine 1 from soma	25 μm
Distance of Spine 2 from soma	15 μm
Distance of Spine 3 from soma	20 μm
Distance of Spine 4 from soma	31 μm
Soma dimension	20 μm*20 μm
Ion channel length at dendritic shaft	1.0 μm
Ion channel length at soma	3.0 μm
Node of Ranvier length in axon	5.0 μm
Ion channel length at the axon hillock	50.0 μm
Axonal internodal distance	70 μm
Diameter of rat axon	1.1 μm

Table 3.3: **Electrical properties of the neuron under investigation.**

Parameter	**Value**	**Description**
C_{Spine} / $C_{Dendrite}$ / C_{Soma}	0.85 $\mu F/cm^2$	Membrane capacitance
C_{Axon}^{Myelin}	0.16 $\mu F/cm^2$	Myelin sheath capacitance
$C_{Axon}^{Membrane}$	1.45 $\mu F/cm^2$	Membrane capacitance
R_{Neck}	54 $M\Omega$	Spine neck resistance

3.3.1 Synaptic input at single spine head

In this section we present the result of action potential propagation due to the synaptic current input at a single spine head. Fig. 3.2 compares the action potential propagation at the spine head, dendritic shaft, soma and the axon. For axon, we record the value in the region close to the axon hillock region. We observe that due to the synaptic current input at the spine, the potential is initially higher at the spine head and least at the axon until the threshold potential is attained at the axon hillock region. Once the threshold is attained, due to the action of the ion channels, the action potential forward propagates along the axon but also leads to the back-propagation in the dendritic spines. A peak action potential value of around 0 mV is numerically recorded as has been observed in [52]. It is to be noted that the synaptic input is only present until the threshold potential is attained. Fig. 3.3 presents the concentration of sodium ions in the spine head and the spine neck along the marked yellow line at the threshold potential timeframe. We can observe that there is a significant concentration variation in the spine. Cable theory which does not consider the ionic variation is thus inaccurate for such small geometries and the Poisson-Nernst-Planck equations present a versatile framework for accurate modeling of the electrical signaling.

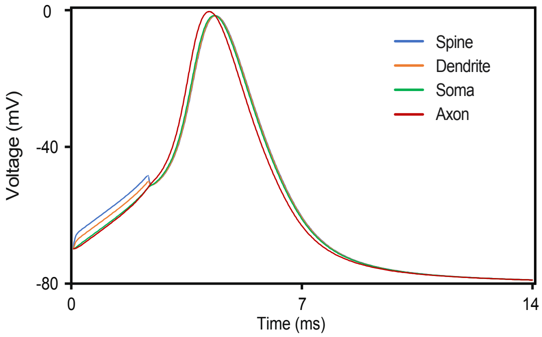

Figure 3.2: Comparison of the action potential propagation in different neuronal regions, namely, the spine, dendritic shaft, soma and the axon. The value of the potential in spine is higher until the action potential is fired at the axon hillock to propagate along the axon and backpropagate into the spine.

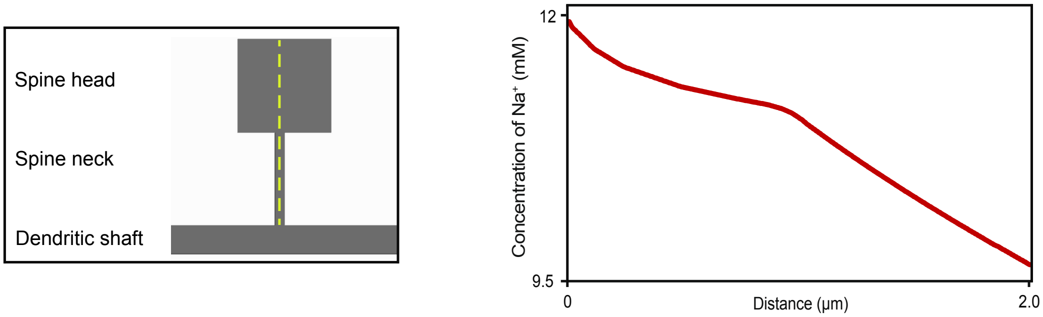

Figure 3.3: Variation of sodium ion concentration in the spine head and neck. Geometry of a spine is depicted on the left. The plot on the right depicts the concentration of sodium ions along the dashed yellow line. The concentration gradient is higher in the spine neck due to its higher diffusional resistance.

Effect of input synaptic current density

To observe the effect of spine geometry on the action potential, we start by varying the input synaptic current. On increasing the input synaptic current density by five times, we observe that the potential difference between the spine and the soma region increases drastically. This is due to the diffusional barrier offered by the spine neck. This is evident from Fig. 3.4. The number of receptors on the spine head or the receptor density on the spine head thus plays an influential role in regulating the voltage attenuation at the soma. As expected, we also observe that the threshold potential is attained early for this case and the peak action potential is higher compared to the previous case.

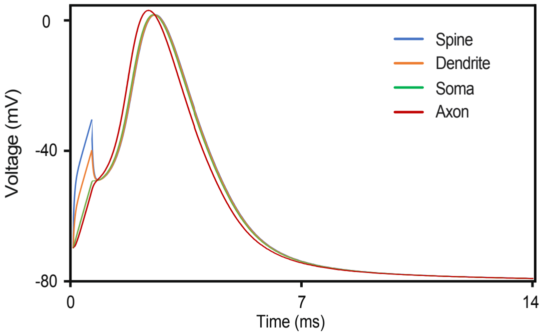

Figure 3.4: A comparison of action potential propagation in the different neuronal regions when the input synaptic current increases by five times. It can be clearly observed that the potential difference between the spine and the soma region increases drastically.

Effect of spine neck geometry

Fig. 3.5 presents the potential plots for various regions in the neuron upon increasing the spine neck length from $1\mu m$ to $4\mu m$. We note that the potential attenuation from the spine to the soma region is higher compared to the base case due to the higher resistance induced by the increased neck length. However, this attenuation is lesser compared to the case when the synaptic current is increased by five folds. A similar case is observed when the spine neck radius is decreased. The initial spine neck resistance is computed to be 54 $M\Omega$.

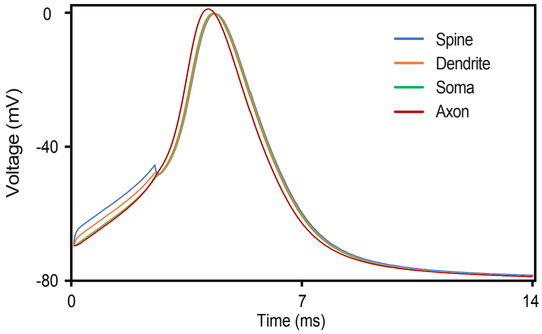

Figure 3.5: Action potential propagation in different regions of the neuron when the spine neck length is increased. A peak action potential of around 0 mV is attained for this case.

Effect of dendritic shaft geometry

After carefully studying the effect of spine geometry, we now observe the effect of the geometry of the dendritic shaft. Fig. 3.6 refers to the case when the width of the dendritic shaft is increased from $0.3\mu m$ to $0.5\mu m$. The potential difference between various regions of the neuron is not considerable for this case. If however the width of the dendritic shaft is reduced to 0.1 μm, the potential difference between various regions is higher due to the increased diffusional resistance offered by the dendrite. This is demonstrated in Fig. 3.7.

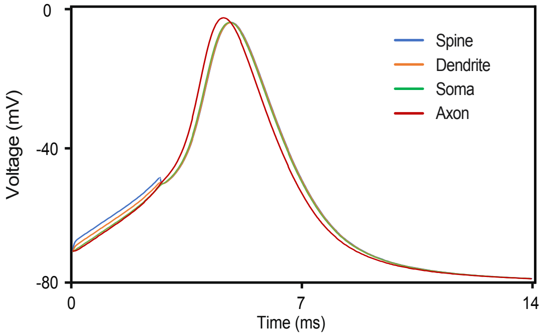

Figure 3.6: Action potential propagation at various regions in the neuron upon increasing the width of the dendritic shaft. The peak action potential is lower for this case as the ion channel density needs to be higher due to larger volume of the geometry.

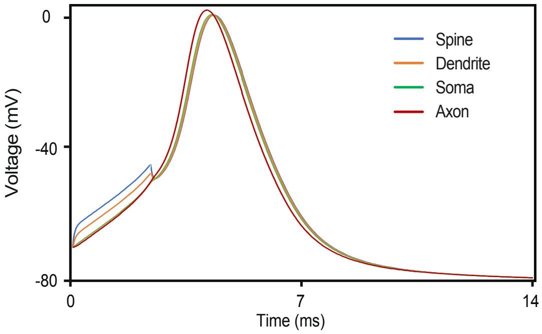

Figure 3.7: Effect of resistance offered by the geometry of dendritic shaft. High diffusional resistance offered by the thin dendritic shaft as observed from the potential propagating in distinct regions in the neuron.

3.3.2 Synaptic input at multiple spines

Next, we consider the case study of the synaptic input being activated at all the four spines present in the FE geometry. As can be observed from Fig. 3.8, we observe that before the threshold potential is attained in the axon hillock, the potential in distinct regions of the neurons is alike. After the firing of the action potential at the hillock, we observe forward propagation along the axon and the backpropagation in the spine as in the earlier cases.

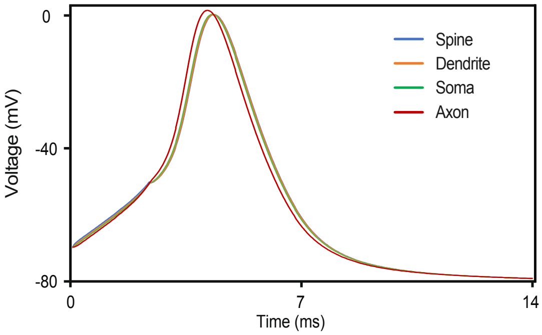

Figure 3.8: Effect of simultaneous injection at multiple spines. The potential profile for action potential propagation when the synaptic current is input in multiple spines at once.

3.4 Discussion

One of the key research problem of neuroscience is to get an elevated understanding of the electrical signaling in the brain. Further, in order to understand neurological diseases, it is of prime importance to understand the fundamental building blocks of the brain- the neuron. Numerical modeling has been an effective strategy to aid the experimental advances. In this work, we present a novel numerical framework of action potential propagation in a complete neuronal geometry. This model can be easily put into use / extended to understand various disease conditions, however, at this point, we focus on understanding the initiation and propagation of action potential in the neuron. We also emphasize the role of spine geometry in regulating synaptic plasticity, which has been an active area of research. The morphological changes in the spine geometry, namely the spine neck length and diameter have been known to play a key role in modulating the potential [54]. The resistance of the dendritic shaft is also considerable relative to the spine. Here, we compute the initial spine neck resistance to be 54 $M\Omega$ and for the dendritic shaft to be 150 $M\Omega$ for the case of synaptic input at a single spine. Fig. 3.9 presents the voltage attenuation at the soma induced by the synaptic input at the spine. We observe that increasing the spine neck length or decreasing the radius of the spine neck leads to increasing the voltage attenuation due to the increased resistance offered by the spine neck. Thus, spine neck has a crucial role to play in synaptic plasticity. We also note that increased input synaptic current density due to the increased number of receptors being activated offers to synaptic plasticity. As reported in literature, we did not observe the effect of spine head geometry or the membrane capacitance to voltage attenuation.

The numerical framework developed here fosters our understanding of the action potential propagation through demonstrating the forward propagation along the axon as well as back propagation into the spine. We note that the voltage amplitude in the spine during forward propagation is around 23 mV and during back propagation has a value of 70 mV. This model can certainly aid the experimental findings such as from voltage dyeing to a far better resolution. Ion channels also play a dominant role in the electrical signaling. Here, we do not study the effect of back propagating voltage attenuation at the spine based on its distance from the soma since ion channel density in the spine is not precisely known. However, once the ion channel density in the spine/ dendrite region is known, the model can be easily extended to study the effect of back propagating voltage amplitude in the spine with their distance from the soma. The ion channel density in the axon hillock region is also critical to the action potential amplitude. Note that the neuron for a rat is considered since a lot of our quantitative understanding is for a rat neuron.

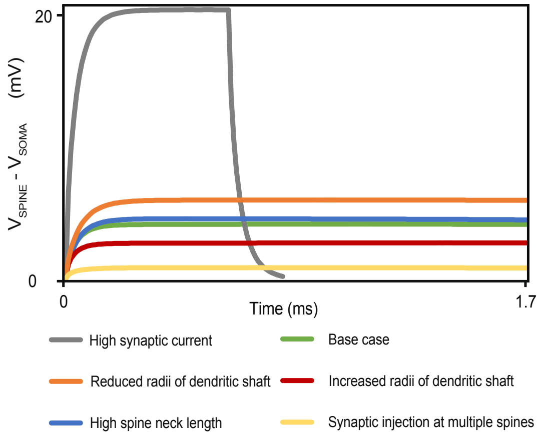

Figure 3.9: Voltage attenuation at the soma induced by the synaptic current in the spine. The effect of input synaptic current density, spine geometry and the dendrite geometry on voltage attenuation at the some is evident. The spine geometry has tremendous capability to modulate the membrane potential.

This model can be easily extended to other neurons such as a human neuron by incorporating the geometry, the ion channel density etc [55].

3.5 Conclusion

Advanced experimental techniques in the last decade have provided bewildering insights into the spine electrophysiology. This necessitates development of a numerical framework that captures the intricate details of the neuron to an astounding resolution. Here, we extend our previous work on axonal electrophysiology using the PNP model to include the spine, the dendrite and the soma regions to observe the action potential initiation and propagation.

To the best of our knowledge, the framework presented here for spatial action potential propagation in the complete neuron geometry using the PNP model is a first-of-its-kind. Further, the role of spine geometry, dendrite geometry on the attenuation of potential from spine to the soma has been demonstrated. Both forward and backward propagation observed in the model enhance its rich capability to act as a digital twin to the neuronal experiments and provide an elevated understanding of neuronal electrophysiology.

Chapter 4

Mechanochemical phenomena on membranes - modeling surface diffusion using Kirchoff-Love shell kinematics

A part of this chapter is a published work:

Auddya, Zhang, Gulati, Vasan, Garikipati, Rangamani, Rudraraju "Biomembranes undergo complex non axisymmetric deformations governed by Kirchhoff-Love kinematics and revealed by a three dimensional computational framework", Proceedings of the Royal Society A, 2021.

4.1 Introduction

Shells and plates are used in a wide variety of applications. A shell is called to be thin when its thickness is very small compared to the characteristic length of the reference surface. Thin shells can be further classified into solid shells and liquid shells and are ubiquitous in nature including biological, chemical and mechanical systems [56–59]. Biological membranes constitute a large proportion of these applications.

Extensive research has been done on diffusion along the volumetric geometries and for the flat planar surfaces such as the widely known Saffman and Delbruck theory, which relates the diffusion constant to the size of the protein, viscosity of the fluid and the membrane thickness [60]. However, the applications of diffusion discussed in the introduction such as in the intracellular transport take place on a highly curved cell membrane. It is believed that the presynaptic neuron modulates the release of neurotransmitters through modulating the curvature of the membrane. Experimental techniques such as single-particle tracking (SPT), fluorescence correlation spectroscopy (FCS), atomic force microscopy (AFM) have been put into use to analyze diffusion. However, there is a lot of anomaly in analyzing the experimental results of diffusion on curved surfaces such as the cell membrane. Analytical results for diffusion on curved manifold are highly complex and have been scarcely attempted in literature. Analysis of a geometry having constant gaussian curvature is elucidated in [61]. [62] adapt geodesic polar coordinates and present the effects of curvature on diffusion, which can then be characterized by the geodesic curvature or the Gaussian curvature. The complicated general diffusion equation can be simplified for the case of developable surfaces and isotropic surfaces. The lack of a generalized analytical solution for various membrane geometries has fueled the motivation for numerical studies of diffusion on curved manifolds which have been carried out in [63] for complex geometries like a dome, tube, pearled structure. However, their geometries are complex, use the Laplace beltrami operator and their formulation is axi-symmetric. [64] compare the diffusion of proteins along the cylindrical geometry of varying curvature. It has been demonstrated that diffusion affects the membrane shape if the spontaneous curvature depends on the concentration [65, 66].

Analogous to diffusion, phase separation is of prime importance to understand mechanisms such as protein aggregation. Phase transformation governs the temporal dispersion of proteins and therefore the physiological functions of the membrane. Protein interactions may result in the creation of protein microdomains. Phase transformations has been modeled using the Ginzburg-Landau energy. Phase separation has been classically studied for volumetric objects and flat surfaces. However, membranes are highly curved and their morphology is critical to protein transport and kinetics. Biological cells modulate their geometry and thus curvature to regulate key biological functions. There has been a lot of interest in computationally modeling Giant unilamellar vesicles (GUVs) as they mimic biological cell membrane and provide great insight into their structure and functioning. It also enables the modeling of proteins in relation to their inherent curvature [67, 68]. For instance, phase separation and protein organization using reaction-diffusion equation on a dendritic spine has been numerically studied using hybrid discrete-continuum stochastic description by [69]. It is known that the geometry of the spine neck plays a critical role in modulating the action potential. Evolution of Cahn-Hilliard on curved geometries has been modeled in [56, 70].

The cellular membrane exhibits significant heterogeneity, encompassing diverse lipids, proteins, and ion channels within its structure. Capturing this spatiotemporal behavior of the cell membrane is numerically challenging [27]. The goal of this chapter is to formulate a general framework of non linear shells and to model the phase transformation phenomena on shells to study the role of curvature on diffusion and phase transformation. We start by presenting diffusion on a two dimensional curved cylindrical surface embedded in the three dimensional space. Diffusion at the continuum scale is a generalization of brownian motion and is modeled using Fick's second law. Here, we do not incorporate molecular crowding which is believed to lead to anomalous diffusion. Next, we rigorously investigate the role of curvature in phase separation. Initially, we start with phase transformation on a rigid geometry and henceforth proceed with a deformable lipid bilayer. To model shells, the Kirchoff-Love theory and Uflyand-Mindlin theory have been prominently utilized in literature. In this work, the Kirchoff-Love shell kinematics is put into use, where the normal to the mid-surface remains perpendicular while deformation. For modeling the in-plane mechanical behaviour, we use the Neo-Hookean energy and for the out of plane bending, Koiter bending energy is utilized. The fourth order partial differential equation in the out of plane deformation is coupled to the fourth order mass conserving Cahn-Hilliard equation, which describes the physics of the phase transformation. The constitutive equations for the thin shell formulation is discussed in detail in the following sections. Finite element technique is used to solve this non-linear coupled set of equations. The weak form requires the solution to be C^1 continuous. FE discretization using Isogeometric analysis (IGA) is employed due to its capability to easily satisfy the requirement of C^1 continuity. The in-plane phase transitions coupled to the out of plane mechanical deformation introduces the Korteweg stress.

4.2 Mathematical background

Here, we briefly review some concepts before moving to the discussion on kinematics and constitutive equations. Contravariant vectors are the vectors whose components transform in the opposite way as compared to the basis. Examples of contravariant vectors are most of the vectors that we know, e.g. force, acceleration etc. These are denoted by $a^i\boldsymbol{u}_i$. Components of a co-variant vector transform in the same way as their basis. Example: gradient field. These are denoted by $a_i\boldsymbol{u}_i$. The values in a metric tensor, $a_{ij} = \boldsymbol{a}_i.\boldsymbol{a}_j$, can be used to measure lengths in a different basis. A 2D surface in 3D space has two principle curvatures κ_1, κ_2. The gaussian curvature,κ (also known as specific curvature/second curvature/total curvature) is the product of the principle curvatures. The mean curvature, H is the average of the principle curvatures. A surface is flat if κ =0 and minimal if H=0. For example, a cylindrical surface is flat.

4.3 Kinematics

Consider a shell (2-manifold) embedded in a 3D volume. Let the reference and current configuration of the shell surface be denoted by $\mathcal{S}_0$ and $\mathcal{S}$, respectively. $\mathcal{S}_0$ and $\mathcal{S}$ are parametrized in terms of the parametric coordinates ξ^1 and ξ^2 that map a flat 2D domain to the surface coordinates $\boldsymbol{X}$ and $\boldsymbol{x}$:

$$\boldsymbol{X} = \boldsymbol{X}(\xi^1, \xi^2) \quad \forall \quad \boldsymbol{X} \in \Omega_0, \qquad \boldsymbol{x} = \boldsymbol{x}(\xi^1, \xi^2) \quad \forall \quad \boldsymbol{x} \in \Omega \tag{4.1}$$

The (covariant) tangent vectors in the reference and current configuration, are given by:

$$\boldsymbol{A}_I = \frac{\partial \boldsymbol{X}}{\partial \xi^I} = \boldsymbol{X}_{,I} \qquad \boldsymbol{a}_i = \frac{\partial \boldsymbol{x}}{\partial \xi^i} = \boldsymbol{x}_{,i} \tag{4.2}$$

Using the tangent vectors we can determine the surface normals as follows:

$$\boldsymbol{N} = \frac{\boldsymbol{A}_1 \times \boldsymbol{A}_2}{\|\boldsymbol{A}_1 \times \boldsymbol{A}_2\|} \qquad \boldsymbol{n} = \frac{\boldsymbol{a}_1 \times \boldsymbol{a}_2}{\|\boldsymbol{a}_1 \times \boldsymbol{a}_2\|} \tag{4.3}$$

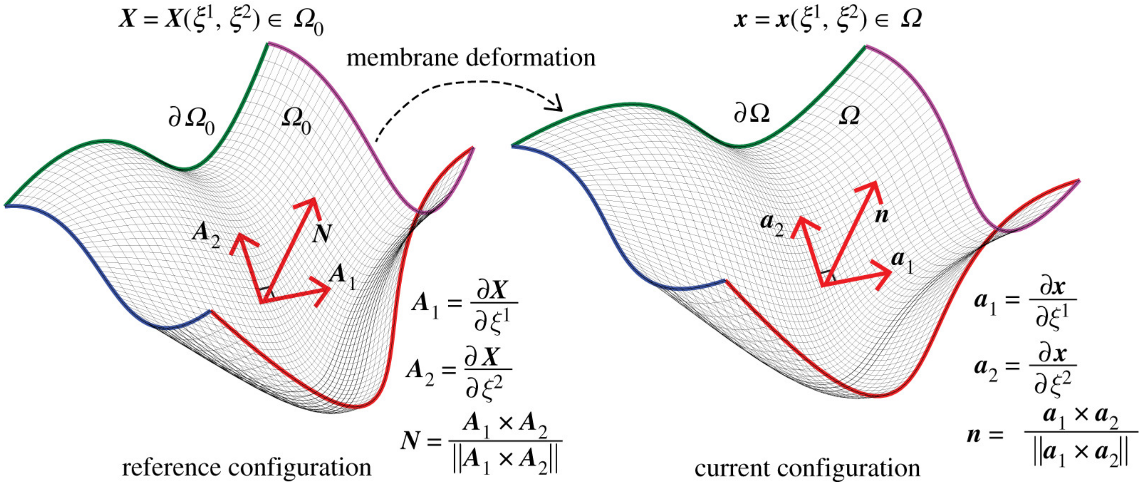

Figure 4.1: Surface parametrization of a biomembrane in the reference undeformed configuration (Ω_0) and current deformed configuration (Ω). The 2D surface, Ω_0, is bounded by the curves $\partial\Omega_0$ (highlighted with color), and embedded in a 3D volume. Here, $\boldsymbol{X}$ is the position vector of a point on the surface parametrized in terms of the surface coordinates (ξ^1,ξ^2) which are associated with a flat 2D domain that is then mapped to Ω_0 as $\boldsymbol{X} = \boldsymbol{X}(\xi^1, \xi^2)$. The local tangent vectors to the surface at $\boldsymbol{X}$ are $\boldsymbol{A}_1$ and $\boldsymbol{A}_2$, and $\boldsymbol{N}$ is the corresponding surface normal. The position dependent triads $\{\boldsymbol{A}_1,\boldsymbol{A}_2,\boldsymbol{N}\}$ and $\{\boldsymbol{a}_1,\boldsymbol{a}_2,\boldsymbol{n}\}$ form the local curvilinear coordinate basis for the reference undeformed configuration and current deformed configuration, respectively.

4.3.1 Metric tensor

Now the components of the metric tensor are given by (via the first fundamental form):

$$A_{IJ} = \boldsymbol{A}_I \cdot \boldsymbol{A}_J \qquad a_{ij} = \boldsymbol{a}_i \cdot \boldsymbol{a}_j \tag{4.4}$$

The contravariant tangent vectors are then given by the transformations:

$$\left[A^{IJ}\right] = \left[A_{IJ}\right]^{-1} \qquad \left[a^{ij}\right] = \left[a_{ij}\right]^{-1} \tag{4.5}$$

$$\boldsymbol{A}^I = A^{IJ}\boldsymbol{A}_J \qquad \boldsymbol{a}^i = a^{ij}\boldsymbol{a}_j \tag{4.6}$$

and the following identities hold:

$$\boldsymbol{A}^I \cdot \boldsymbol{A}_J = \delta^I_J \qquad \boldsymbol{a}^i \cdot \boldsymbol{a}_j = \delta^i_j \tag{4.7}$$

4.3.2 Curvature tensor

The second order derivatives of the surface coordinates $\boldsymbol{X}$ and $\boldsymbol{x}$ are given by:

$$\boldsymbol{A}_{I,J} = \frac{\partial \boldsymbol{A}_I}{\partial \xi_J} \qquad \boldsymbol{a}_{i,j} = \frac{\partial \boldsymbol{a}_i}{\partial \xi_j} \tag{4.8}$$

and the corresponding covariant derivatives are given by:

$$\boldsymbol{A}_{I;J} = (\boldsymbol{N} \otimes \boldsymbol{N})\boldsymbol{A}_{I,J} \qquad \boldsymbol{a}_{i;j} = (\boldsymbol{n} \otimes \boldsymbol{n})\boldsymbol{a}_{i,j} \tag{4.9}$$

The covariant derivative can be more easily obtained through the use of the Christoffel symbols ($\Gamma^K_{IJ} = \boldsymbol{a}^K \cdot \boldsymbol{a}_{I,J}$):

$$\boldsymbol{A}_{I;J} = \boldsymbol{A}_{I,J} - \Gamma^K_{IJ}\boldsymbol{A}_K \qquad \boldsymbol{a}_{i;j} = \boldsymbol{a}_{i,j} - \Gamma^k_{ij}\boldsymbol{a}_k \tag{4.10}$$

Now we can obtain the derivatives of the tangent vectors and thus the components of the curvature tensor (via the second fundamental form) in the reference and current configuration as:

$$B_{IJ} = \boldsymbol{A}_{I,J} \cdot \boldsymbol{N} \qquad b_{ij} = \boldsymbol{a}_{i,j} \cdot \boldsymbol{n} \tag{4.11}$$

Using the components of the curvature tensor, we can obtain the mean curvature:

$$H = \frac{1}{2}B^{IJ}A_{IJ} \quad \text{on} \quad \mathcal{S}_0, \qquad H = \frac{1}{2}b^{ij}a_{ij} \quad \text{on} \quad \mathcal{S} \tag{4.12}$$

the Gaussian curvature:

$$\kappa = \frac{|B|}{|A|} \quad \text{on} \quad \mathcal{S}_0, \qquad \kappa = \frac{|b|}{|a|} \quad \text{on} \quad \mathcal{S}, \quad |\cdot| = det(\cdot) \tag{4.13}$$

and the principal curvatures:

$$\kappa_{1/2} = H \pm \sqrt{H^2 - \kappa} \tag{4.14}$$

4.3.3 Shell basis

The triads $\{\boldsymbol{A}_1, \boldsymbol{A}_2, \boldsymbol{N}\}$ and $\{\boldsymbol{A}^1, \boldsymbol{A}^2, \boldsymbol{N}\}$ both form a basis to decompose vectors into the in-plane and out-of-plane components. For any general vector $\boldsymbol{V} \in R^3$,

$$\boldsymbol{V} = V^I \boldsymbol{A}_I + (\boldsymbol{V}.\boldsymbol{N})\boldsymbol{N} = V_I \boldsymbol{A}^I + (\boldsymbol{V}.\boldsymbol{N})\boldsymbol{N} \tag{4.15}$$

where $V_I = \boldsymbol{V} \cdot \boldsymbol{A}_I$ and $V^I = \boldsymbol{V} \cdot \boldsymbol{A}^I$ are the covariant and contravariant components of the vector $\boldsymbol{V}$. Similarly, one can use the basis $\{\boldsymbol{a}_1, \boldsymbol{a}_2, \boldsymbol{n}\}$ or $\{\boldsymbol{a}^1, \boldsymbol{a}^2, \boldsymbol{n}\}$ to decompose any general vector $\boldsymbol{v} \in R^3$ in the current configuration.

4.3.4 Additional surface kinematics

The variation of the tangent vector can be obtained as:

$$\delta \boldsymbol{a}_i = \delta \boldsymbol{x}_{,i} \tag{4.16}$$

Taking its parametric derivative;

$$\delta \boldsymbol{a}_{i,j} = \delta \boldsymbol{x}_{,ij} \tag{4.17}$$

The variation of equation 4.4 is given by:

$$\delta a_{ij} = \boldsymbol{a}_i.\delta \boldsymbol{a}_j + \delta \boldsymbol{a}_i.\boldsymbol{a}_j \tag{4.18}$$

The co-variant vectors are perpendicular to the normal i.e. $\boldsymbol{a}_i.\boldsymbol{n} = 0$. The variation of the normal can therefore be computed as

$$\delta \boldsymbol{n} = -\boldsymbol{a}^i(\boldsymbol{n}.\delta \boldsymbol{a}_i) \tag{4.19}$$

Using equation 4.11, the variation of the curvature tensor can be obtained as:

$$\delta b_{ij} = \boldsymbol{a}_{i,j}.\delta \boldsymbol{n} + \boldsymbol{n}.\delta \boldsymbol{a}_{i,j} \tag{4.20}$$

Substituting equation 4.19, the following expression can be obtained

$$\delta b_{ij} = (\delta \boldsymbol{a}_{i,j} - \Gamma^{k}_{ij} \delta \boldsymbol{a}_k).\boldsymbol{n} \tag{4.21}$$

From the formula of Gauss;

$$\boldsymbol{a}_{i;j} = b_{ij}\boldsymbol{n} \tag{4.22}$$

The surface deformation gradient is given by;

$$\boldsymbol{F} = \boldsymbol{a}_i \otimes \boldsymbol{A}^i \tag{4.23}$$

The area change $ds = JdA$ where J is the surface stretch.

$$J = \frac{J_a}{J_A} = \frac{\sqrt{deta_{ij}}}{\sqrt{detA_{ij}}} \tag{4.24}$$

The following expression for jacobian can therefore be obtained;

$$\frac{\partial J}{\partial a_{ij}} = \frac{J}{2} a^{ij} \tag{4.25}$$

The right cauchy green tensor, $\boldsymbol{C}$ is given as $\underline{\mathrm{C}} = \boldsymbol{F}^T \underline{\mathrm{F}} = a_{ij} \underline{\mathrm{A}}^i \otimes \underline{\mathrm{A}}^j$. Its trace, $I_1 = \underline{\mathrm{C}} : \underline{1}_o$, where $\underline{1}_o = \underline{\mathrm{A}}_i \otimes \boldsymbol{A}^i$. Solving, $I_1 = A^{ij} a_{ij}$ It can be determined;

$$\delta a = a a^{ij} \delta a_{ij} \tag{4.26}$$

The following can be obtained

$$\delta a^{ij} = a^{ijkl} \delta a_{kl} \tag{4.27}$$

where

$$a^{ijkl} = \frac{\partial a^{ij}}{\partial a^{kl}} = \frac{-1}{2}(a^{ik}a^{jl} + a^{il}a^{jk}) \tag{4.28}$$

which has major and minor symmetry. Therefore, contracting it with symmetric tensor yields,

$$b_{kl} a^{ijkl} b_{kl} = -b^{ij} \tag{4.29}$$

Using equation 4.12, the variation of the mean curvature can be computed as,

$$\delta H = \frac{1}{2}\partial a^{ij} b_{ij} + \frac{1}{2} a^{ij} \partial b_{ij} \tag{4.30}$$

For mean curvature, using equation 4.26, 4.28, it follows:

$$\frac{\partial H}{\partial a_{ij}} = \frac{-b^{ij}}{2} \tag{4.31}$$

$$\frac{\partial H}{\partial b_{ij}} = \frac{a^{ij}}{2} \tag{4.32}$$

Gaussian curvature, κ, is also given by

$$\kappa = \frac{1}{2} e^{ij} e^{kl} b_{ik} b_{jl} \frac{1}{a} \tag{4.33}$$

and its variation can be computed as;

$$\delta\kappa = \frac{1}{2} e^{ij} e^{kl} \delta b_{ik} b_{jl} \frac{1}{a} + \frac{1}{2} e^{ij} e^{kl} b_{ik} \delta b_{jl} \frac{1}{a} - \frac{1}{2} e^{ij} e^{kl} b_{ik} b_{jl} \frac{\delta a}{a^2} \tag{4.34}$$

Using the third term in preceeding equation, and equation 4.26 we get,

$$\frac{\partial \kappa}{\partial a_{ij}} = -\kappa a^{ij} \tag{4.35}$$

Using the first two terms in equation 4.34 one can arrive at,

$$\frac{\delta\kappa}{\delta b_{ij}} = \frac{1}{2} e^{ij} e^{jl} b_{jl} \frac{1}{a} + \frac{1}{2} e^{ij} e^{kj} b_{jk} \frac{1}{a} = \frac{b}{a} b^{ij}_{inv} = \kappa b^{ij}_{inv} \tag{4.36}$$

4.4 Material model

Considering the classical Helfrich formulation for biological membranes, the strain energy density of a membrane in the current configuration is given by:

$$w = k_B * (h - h_0)^2 + k_G \kappa \tag{4.37}$$

where k_B and k_G are the bending modulus and the Gaussian curvature modulus of the membrane, h is the mean curvature, κ is the Gaussian curvature and h_0 represents the instantaneous curvature induced in the membrane. To enforce the constant area constraint, we can consider a penalty formulation or Lagrange multiplier formulation.

In the penalty formulation, the total strain energy density of the membrane in the current configuration is given as :

$$w_P = k_B * (h - h_0)^2 + k_G\kappa + \frac{\delta}{2}(J-1)^2 \tag{4.38}$$

where J $(= \frac{\sqrt{det(a)}}{\sqrt{det(A)}})$ is the surface stretch and δ is the penalty parameter.

Likewise, following a Lagrange multiplier formulation for the constant area constraint:

$$w_{LM} = k_B * (h - h_0)^2 + k_G\kappa + \lambda(J-1) \tag{4.39}$$

where λ is the point value of the Lagrange multiplier field.

4.5 Equilibrium

The conditions for quasi-static equilibrium in the weak formulation are given by [57] :

$$\int_S \frac{1}{2}\delta a_{ij}\sigma^{ij} da + \int_S \delta b_{ij} M^{ij} da - \int_S \delta\boldsymbol{x}\cdot\boldsymbol{f} da - \int_{\partial S} \delta\boldsymbol{x}\cdot\boldsymbol{t} ds = 0 \tag{4.40}$$

For a hyperelastic material model, we can express the stress and moment components in terms of the strain energy density as:

$$\sigma^{ij} = \frac{2}{J}\frac{\partial w}{\partial a_{ij}} \tag{4.41}$$

$$M^{ij} = \frac{1}{J}\frac{\partial w}{\partial b_{ij}} \tag{4.42}$$

For the Helfrich-type strain energy density expressions, without the area constraint, these are given by:

$$\sigma^{ij} = (k_B(h-h_0)^2 - k_G\kappa)a^{ij} - 2k_B(h-h_0)b^{ij} \tag{4.43}$$

$$M^{ij} = (k_B(h-h_0) + 2k_G h)a^{ij} - k_G b^{ij} \tag{4.44}$$

Finite Element Formulation

A point $\boldsymbol{x}$ in the current configuration can be approximated as

$$\boldsymbol{x} \approx \bar{\mathbf{N}}\mathbf{x_e} \tag{4.45}$$

where e denotes the element and $\bar{\mathbf{N}}$ is the basis function obtained from NURBS so that the mesh is C^1 continuous. The variation of $\boldsymbol{x}$ can be obtained as

$$\delta\mathbf{x} \approx \bar{\mathbf{N}}\delta\mathbf{x_e} \tag{4.46}$$

The co-variant tangent vector can now be written as

$$\boldsymbol{a}_i = \frac{\partial\mathbf{x}}{\partial\xi^i} \approx \bar{\mathbf{N}}_{,\mathbf{i}}\mathbf{x_e} \tag{4.47}$$

and the variation of the tangent vector can be expressed as:

$$\delta\boldsymbol{a}_i \approx \bar{\mathbf{N}}_{,\mathbf{i}}\delta\mathbf{x_e} \tag{4.48}$$

Using the above finite dimensional discretization, the weak form can be expressed as

$$\int_S \frac{1}{2}(2\boldsymbol{a}_i\delta\boldsymbol{a}_j)\sigma^{ij}da + \int_S(\delta\boldsymbol{a}_{i,j} - \Gamma^k_{ij}\delta\boldsymbol{a}_k).\boldsymbol{n}M^{ij}da - \int_S \delta\boldsymbol{x}\cdot\boldsymbol{f}da - \int_{\partial S}\delta\boldsymbol{x}\cdot\boldsymbol{t}ds = 0 \tag{4.49}$$

Knowing the variations are given by $\delta\boldsymbol{a}_i = \bar{\boldsymbol{N}}_{,i}\delta\boldsymbol{x}_e$ and $\delta b_{ij} = (\bar{\boldsymbol{N}}_{,ij} - \Gamma^k_{ij}\bar{\boldsymbol{N}}_{,k}).\boldsymbol{n}\delta\boldsymbol{x}_e$, this expression reduces to

$$\int_S \boldsymbol{a}_i \bar{\boldsymbol{N}}_{,j} \sigma^{ij} da \delta \boldsymbol{x}_e + \int_S (\bar{\boldsymbol{N}}_{,ij} - \Gamma^k_{ij} \bar{\boldsymbol{N}}_{,k}).\boldsymbol{n} M^{ij} da \delta \boldsymbol{x}_e - \int_S \bar{\boldsymbol{N}} \boldsymbol{f} da \delta \boldsymbol{x}_e - \int_{\partial S} \bar{\boldsymbol{N}} \boldsymbol{t} ds \delta \boldsymbol{x}_e = 0 \tag{4.50}$$

This is the finite dimensional weak formulation of the problem that is implemented in the computational code underlying the framework presented in this work.

4.5.1 Stabilization stress

The stabilization stress σ^{ij}_{sta} can be added to σ^{ij} to stabilize the system of liquid shells by adding additional stiffness. The stress term can be split into in-plane and out of plane components. The stabilization stress can therefore be added to the respective stress component. Variation in x can be split into in-plane and out of plane components: $\delta x = w_i \boldsymbol{a}^i + w\boldsymbol{n}$ where w_i is in-plane component and w is the out of plane component along the normal. The variation δa_{ij} can be written as; $\delta a_{ij} = w_{i;j} + w_{j;i} - 2wb_{ij}$. Substituting this expression of variation of a_{ij}, it can be written in terms of in-plane and out of plane stress components:

$$\int \frac{1}{2} \delta a_{ij} \sigma^{ij} da = \int \frac{1}{2} (2w_{i;j} - 2wb_{ij}) \sigma^{ij} da \tag{4.51}$$

$$\int \frac{1}{2} \delta a_{ij} \sigma^{ij} da = \int w_{i;j} \sigma^{ij} da - \int wb_{ij} \sigma^{ij} da \tag{4.52}$$

Thus the out of plane component can be written as $-\int \sigma^{ij} b_{ij} N^T \boldsymbol{n} da$ and the in-plane component can be written as total term minus the out of plane component, i.e. $\int \sigma^{ij} N^T_{,i} a_j da - \int \sigma^{ij} b_{ij} N^T \boldsymbol{n} da$

4.5.2 Rotational boundary conditions

The rotational constraints at the boundaries can be applied using the penalty method. The constraint potential is

$$\int \frac{\epsilon}{2} (n - \bar{n}).(n - \bar{n}) dS \tag{4.53}$$

Taking its variation and using equation 4.19, we get

$$\int \frac{\epsilon}{2} 2(n-\bar{n}).\delta n dS = \int \epsilon(n-\bar{n})(-a^i \boldsymbol{n}.N_{,i}) dS \delta x_e = \int -\epsilon(n-\bar{n}) a^i \boldsymbol{n} N_{,i} dS \delta x_e \tag{4.54}$$

4.6 Cahn Hilliard

The formulation for phase transformation using the Cahn Hilliard principles on deforming surfaces is discussed here. A brief on surface derivatives is reviewed in the first sub section.

4.6.1 Surface Calculus Revisit

In cartesian coordinates, we write gradients as:

$$\nabla f = \frac{\partial f}{\partial x} i + \frac{\partial f}{\partial y} j \tag{4.55}$$

which in indicial notation can be written as;

$$\nabla^i f = \frac{\partial f}{\partial x} \tag{4.56}$$

while the differential operator is expressed as:

$$df = \frac{\partial f}{\partial x} dx + \frac{\partial f}{\partial y} dy \tag{4.57}$$

On a general manifold, the gradient is defined as,

$$\nabla f = f_{;i} \mathbf{a}^i \tag{4.58}$$

which can be expressed in indicial notation, with basis $\mathbf{a}_i$, as

$$\nabla^i f = a^{ij} \frac{\partial f}{\partial \xi^j} = a^{ij} \partial_j f \tag{4.59}$$

For instance, in cartesian basis, $a^{ij} = \delta_{ij}$ and the expression for gradient reduces to that in Eq. 4.56. For a polar basis, $a^{ij} = \begin{pmatrix} 1 & 0 \\ 0 & \frac{1}{r^2} \end{pmatrix}$. The expression for gradient in Eq. 4.59 reduces to

$$\nabla f = \frac{\partial f}{\partial r} e_r + \frac{1}{r^2} \frac{\partial f}{\partial \theta} e_\theta \tag{4.60}$$

For a general vector $\mathbf{v} = v^\alpha \mathbf{a}_\alpha + v\mathbf{n}$, the divergence operator on a general basis on the manifold is written as:

$$\nabla \cdot (\mathbf{v}) = (v^\beta \mathbf{a}_\beta + v\mathbf{n})_{;\alpha} \cdot \mathbf{a}^\alpha = (v^\beta \mathbf{a}_\beta)_{;\alpha} \cdot \mathbf{a}^\alpha + (v_{;\alpha}\mathbf{n} + v\mathbf{n}_{;\alpha}) \cdot \mathbf{a}^\alpha \tag{4.61}$$

$$= v^\beta_{;\alpha} a^\alpha_\beta + v^\beta \mathbf{a}_{\beta;\alpha} \cdot \mathbf{a}^\alpha + (0 + v(-b_{\alpha\beta}\mathbf{a}^\beta) \cdot \mathbf{a}^\alpha) = v^\alpha_{;\alpha} + 0 + 0 - v b_{\alpha\beta} a^{\alpha\beta} = v^\alpha_{;\alpha} - 2Hv \tag{4.62}$$

where

$$\mathbf{a}_{\alpha;\beta} = b_{\alpha\beta}\mathbf{n}, \qquad H = \frac{1}{2} a^{\alpha\beta} b_{\alpha\beta} \tag{4.63}$$

Finally, the Laplace operator can be written as;

$$\Delta f = \nabla \cdot (\nabla f) = (f_{;\beta}\mathbf{a}^\beta)_{;\alpha} \cdot \mathbf{a}^\alpha = f_{;\alpha\beta} a^{\alpha\beta} \tag{4.64}$$

4.6.2 Phase transformation formulation

To model phase transformation, the free energy density functional for the coupled Cahn-Hilliard and out of plane deformation can be written as

$$W = J(k_B(c) * (H - H_0(c))^2 + k_G\kappa) + \frac{\lambda(c)}{2}(J-1)^2 + JN\omega\frac{\gamma}{2}\nabla c \cdot \nabla c + k_c N\omega c(1-c)$$
$$+ TNk_{Bolt}(c \log c + (1-c)\log(1-c)) \tag{4.65}$$
$$= J(k_B(c) * (H - H_0(c))^2 + k_G\kappa) + \frac{\lambda(c)}{2}(J-1)^2 + JN\omega\frac{\gamma}{2} c_{;\mu}\mathbf{a}^\mu \cdot c_{;\nu}\mathbf{a}^\nu + k_c N\omega c(1-c)$$
$$+ TNk_{Bolt}(c \log c + (1-c)\log(1-c)) \tag{4.66}$$
$$= J(k_B(c) * (H - H_0(c))^2 + k_G\kappa) + \frac{\lambda(c)}{2}(J-1)^2 + JN\omega\frac{\gamma}{2} c_{;\mu}c^{;\mu} + k_c N\omega c(1-c)$$
$$+ TNk_{Bolt}(c \log c + (1-c)\log(1-c)) \tag{4.67}$$

Note that the gradient term in the above expressions is on the surface manifold. Stress can then be computed as

$$\begin{aligned}\sigma^{ij} &= a^{ij}(k_b(H-H_o)^2 - k_g\kappa) - 2k_b(H-H_o)b^{ij} + \lambda(J-1)a^{ij} \\ &\quad + \frac{2}{J}N\omega\Big(\frac{J}{2}a^{ij}\frac{\gamma}{2}c_{;\mu}c^{;\mu} + \frac{J\gamma}{2}c_{;\mu}c_{;\nu}\frac{\partial a^{\mu\nu}}{\partial a_{ij}}\Big)\end{aligned} \tag{4.68}$$

We know from Eq. (4.28):

$$\frac{\partial a^{\mu\nu}}{\partial a_{ij}} = \frac{-1}{2}(a^{\nu i}a^{\mu j} + a^{\nu j}a^{\mu i}) \tag{4.69}$$

Stress for the coupled bending-phase transformation then reduces to

$$\begin{aligned}\sigma^{ij} &= a^{ij}(k_b(H-H_o)^2 - k_g\kappa) - 2k_b(H-H_o)b^{ij} + \lambda(J-1)a^{ij} \\ &\quad + \gamma N\omega\Big(\frac{1}{2}c_{;\mu}c^{;\mu}a^{ij} - c^{;i}c^{;j}\Big)\end{aligned} \tag{4.70}$$

The last term in the above expression is the Korteweg stress, σ^{ij}_{CH} due to the Cahn-Hilliard energy. The free-energy density functional reduces to the same moment as for the helfrich-bending case discussed earlier.

From energy balance [56], the chemical potential per unit reference area is obtained to be

$$\mu_c = \frac{\partial W}{\partial c} - J\Big(\frac{1}{J}\frac{\partial W}{\partial c_{;\alpha}}\Big)_{;\alpha} = \mu_b + \mu_i = \mu_{cc} + \mu_{el} + \mu_i \tag{4.71}$$

The chemical potential can now be computed as

$$\mu_b = \frac{\partial W}{\partial c} = \mu_{el} + \mu_{cc} \tag{4.72}$$

$$\mu_{el} = J\Big(k_b^{'}(c)(H - H_o(c))^2 - 2k_b(c)(H - H_o(c))H_o^{'}(c)\Big) + \frac{\lambda^{'}(c)}{2}(J-1)^2 \tag{4.73}$$

$$\mu_{cc} = k_c N\omega \frac{\partial}{\partial c} c(1-c) + TNk_{Bolt} \log \frac{c}{1-c} \tag{4.74}$$

$$\mu_i = -JN\omega\gamma\Delta c \tag{4.75}$$

$$\begin{aligned} \mu_c = \frac{\partial W}{\partial c} &= J\Big(k_b^{'}(c)(H - H_o(c))^2 - 2k_b(c)(H - H_o(c))H_o^{'}(c)\Big) \\ &+ \frac{\lambda^{'}(c)}{2}(J-1)^2 - JN\omega\gamma\Delta c \\ &+ k_c N\omega \frac{\partial}{\partial c} c(1-c) + TNk_{Bolt} \log \frac{c}{1-c} \end{aligned} \tag{4.76}$$

The diffusive flux can be decomposed as

$$j^\alpha = j_c^\alpha + j_{el}^\alpha + j_i^\alpha \tag{4.77}$$

where

$$j_{oo}^\alpha = -\frac{M}{J} a^{\alpha\beta} \mu_{oo,\beta}, \qquad oo = c, el, i \tag{4.78}$$

Here $M = Dc(1-c)$ is the mobility with the parameter D as constant.

4.6.3 Weak form-CH

Using the balance of mass equation: $\rho\dot{c} = -j^\alpha_{;\alpha}$, we can write the weak form as:

$$\int_\Omega \rho\dot{c} w da + \int_\Omega w j^\alpha_{;\alpha} da = 0 \tag{4.79}$$

$$\int_\Omega \rho\dot{c} w da - \int_\Omega w_{;\alpha} j^\alpha da + \int_{\partial\Omega} w \mathbf{j} \cdot \nu ds = 0 \tag{4.80}$$

Note that j_i^α leads to three derivatives of concentration, c. To reduce this to second order, lets apply surface divergence theorem to the second term.

$$\int_{\partial\Omega} \nabla w \cdot \nu M(\frac{\mu_i}{J})ds = \int_{\Omega}(\Delta w M + \nabla w \nabla M)\mu_i dA + \int_{\Omega} \nabla w(-j_i^{\alpha})da \tag{4.81}$$

The same expression follows for μ_{el}. We then obtain:

$$\int_{\partial\Omega} \nabla w \cdot \nu M(\frac{\mu_i + \mu_{el}}{J})ds = \int_{\Omega}(\Delta w M + \nabla w \nabla M)(\mu_i + \mu_{el})dA + \int_{\Omega} \nabla w(-j_i^{\alpha} - j_{el}^{\alpha})da \tag{4.82}$$

$$\int_{\Omega} \nabla w(j_i^{\alpha} + j_{el}^{\alpha})da = -\int_{\partial\Omega} \nabla w \cdot \nu M(\frac{\mu_i + \mu_{el}}{J})ds + \int_{\Omega}(\Delta w M + \nabla w \nabla M)(\mu_i + \mu_{el})dA \tag{4.83}$$

where $\nabla M = M^{'} \nabla c$ and

$$\nabla w j_{cc}^{\alpha} = -\nabla w \cdot \nabla c \mu_{cc}^{'} \frac{M}{J} \tag{4.84}$$

The weak form in Eq. 4.80 reduces to:

$$\int_{\Omega} \rho \dot{c} w da + \int_{\Omega_o} \nabla w \cdot \Big(M \mu_{cc}^{'} - M^{'}(\mu_i + \mu_{el})\Big) \nabla c dA - \int_{\Omega_o} \Delta w M(\mu_i + \mu_{el})dA \tag{4.85}$$

$$+ \int_{\partial\Omega} w \mathbf{j} \cdot \nu ds + \int_{\partial\Omega} \nabla w \cdot \nu M(\frac{\mu_i + \mu_{el}}{J})ds = 0 \tag{4.86}$$

4.6.4 FE Discretization

Using,

$$c_{;\alpha}^{h} = \bar{N}_{,\alpha} c_e \tag{4.87}$$

$$\nabla c^h = \mathbf{a}^{\alpha} \bar{N}_{,\alpha} c_e \tag{4.88}$$

$$\nabla w^h = \bar{N}_{,\alpha} \mathbf{a}^{\alpha} \delta c_e \tag{4.89}$$

$$\Delta c^h = \Delta \bar{N} c_e = a^{\alpha\beta}(\bar{N}_{,\alpha\beta} - \Gamma_{\alpha\beta}^{\gamma} \bar{N}_{,\gamma})c_e \tag{4.90}$$

$$\Delta w^h = \Delta \bar{N} \delta c_e = a^{\alpha\beta}(\bar{N}_{,\alpha\beta} - \Gamma_{\alpha\beta}^{\gamma} \bar{N}_{,\gamma})\delta c_e \tag{4.91}$$

The weak form can be discretized as:

$$\begin{aligned} R = &\int_{\Omega_o} \rho_o \dot{c} \bar{N} dA + \int_{\Omega_o} \bar{N}_{,\alpha} a^{\alpha\beta} \cdot \Big(M\mu^{'}_{cc} - M^{'}(\mu_i + \mu_{el})\Big) \bar{N}_{,\beta} c_e dA \\ &- \int_{\Omega_o} a^{\alpha\beta}(\bar{N}_{,\alpha\beta} - \Gamma^{\gamma}_{\alpha\beta}\bar{N}_{,\gamma}) M(\mu_i + \mu_{el}) dA + \int_{\partial\Omega} \bar{N}\mathbf{j} \cdot \nu ds \\ &+ \int_{\partial\Omega} \bar{N}_{,\alpha}\mathbf{a}^{\alpha} \cdot \nu M(\frac{\mu_i + \mu_{el}}{J}) ds \end{aligned} \tag{4.92}$$

Note that $\dot{c}$ can be discretised in time using backward euler. For a non-coupled phase transformation $\mu_{el} = 0$. The line integrals can be taken to be zero assuming zero flux across boundary.

4.7 Formulation of Cahn-Hilliard Coupled with Shell Mechanics (Neo Hookean in-plane and Koiter bending model)

The free energy density functional can be written as

$$\begin{aligned} \Psi(\boldsymbol{\alpha}, \boldsymbol{\beta}, c) = &\frac{K(c)}{4}(J^2 - 1 - 2ln(J)) + \frac{G(c)}{2}(\frac{I_1}{J} - 2) + \frac{C(c)}{2}(b_{ij} - B_{ij})(b_o^{ij} - B^{ij}) \\ &+ f_c + J\frac{\gamma}{2}\boldsymbol{\nabla} c \cdot \boldsymbol{\nabla} c \end{aligned} \tag{4.93}$$

in the reference configuration, where $K(c), G(c), C(c)$ are the bulk modulus, shear modulus and the bending modulus respectively and $b_o^{ij} = A^{ik} b_{kl} A^{lj}$. Note that the $\boldsymbol{\nabla}$ is the surface gradient. Stress can be computed to be

$$\begin{aligned} \sigma^{ij} = &\frac{2}{J}\Big[\frac{K(c)}{4}(2J.\frac{J}{2}A^{ij} - \frac{2}{J}.\frac{J}{2}a^{ij}) + \frac{G(c)}{2}(\frac{A^{ij}}{J} - \frac{I_1}{J^2}.\frac{J}{2}a^{ij}) + \frac{J}{2}a^{ij}\frac{\gamma}{2}c_{,m}c^{,m} \\ &+ \frac{J\gamma}{2}c_{,m}c_{,n}\frac{\partial a^{mn}}{\partial a_{ij}}\Big] \end{aligned} \tag{4.94}$$

$$= \frac{K(c)}{2J}(J^2 - 1)a^{ij} + \frac{G(c)}{2J^2}(2A^{ij} - I_1 a^{ij}) + \gamma(\frac{1}{2}c_{,m}c^{,m}a^{ij} - c^{,i}c^{,j}) \tag{4.95}$$

The moment can similarly be calculated to be,

$$M^{ij} = \frac{1}{J}\big[\frac{C(c)}{2}(b_o^{ij} - B^{ij}) + \frac{C(c)}{2}(b_{ij} - B_{ij})(A^{im}A^{jn}\delta_{im}\delta_{jn})\big] \tag{4.96}$$

$$= \frac{C(c)}{J}(b_o^{ij} - B^{ij}) \tag{4.97}$$

Chemical potential is the variational derivative of the free energy density functional and computed to be

$$\mu = \mu_{el} + \mu_c \tag{4.98}$$

where

$$\mu_{el} = \frac{K'(c)}{4}(J^2 - 1 - 2ln(J)) + \frac{G'(c)}{2}(\frac{I_1}{J} - 2) + \frac{C'(c)}{2}(b_{ij} - B_{ij})(b_o^{ij} - B^{ij}) \tag{4.99}$$

$$\mu_c = f_{c,c} - J\gamma\Delta c \tag{4.100}$$

The equation for chemistry is now presented. We start from the mass balance equation

$$\rho\dot{c} = -\boldsymbol{\nabla}\cdot j \quad \text{where} \quad j = -M\boldsymbol{\nabla}\mu \tag{4.101}$$

The weak form can then be written as:

$$\int_\Omega w\rho\dot{c}da = -\int_\Omega w\boldsymbol{\nabla}\cdot jda \tag{4.102}$$

$$= -\int_{\partial\Omega} j\cdot nwds + \int_\Omega j\boldsymbol{\nabla}wda \tag{4.103}$$

$$= 0 - \int_\Omega M\boldsymbol{\nabla}\mu\boldsymbol{\nabla}wda \tag{4.104}$$

$$\int_\Omega w\rho\dot{c}da = -\int_\Omega M\boldsymbol{\nabla}w\boldsymbol{\nabla}(\frac{\mu_{el}}{J} + \mu_c)da \tag{4.105}$$

$$= -M\int_\Omega \boldsymbol{\nabla}w\frac{\boldsymbol{\nabla}\mu_{el}}{J}da - \int_\Omega M\boldsymbol{\nabla}w\frac{\boldsymbol{\nabla}f_{c,c}}{J}da + \int_\Omega M\gamma\boldsymbol{\nabla}w\boldsymbol{\nabla}\Delta cda \tag{4.106}$$

$$= -M\int_{\partial\Omega_o}\boldsymbol{\nabla}w\mu_{el}dS + M\int_{\Omega_o}\Delta w\mu_{el}dA - \int_{\Omega_o}M\boldsymbol{\nabla}w\boldsymbol{\nabla}cf_{c,cc}dA \tag{4.107}$$

$$+ M\gamma\int_{\partial\Omega}\boldsymbol{\nabla}w\Delta cds - M\gamma\int_\Omega \Delta c\Delta wda \tag{4.108}$$

The residual can finally be computed as

$$R = \int_{\Omega} w\rho\dot{c}da + M\int_{\partial\Omega_o} \boldsymbol{\nabla} w\mu_{el}\cdot ndS - M\gamma\int_{\partial\Omega} \boldsymbol{\nabla} w\Delta c\cdot nds - M\int_{\Omega_o} \Delta w\mu_{el}dA \tag{4.109}$$

$$+\int_{\Omega_o} M\boldsymbol{\nabla} w\boldsymbol{\nabla} cf_{c,cc}dA + M\gamma\int_{\Omega}\Delta c\Delta wda \tag{4.110}$$

If required, the following terms (Nitsche's terms) can be added to the Residual

$$N = -\int_{\partial\Omega} M\gamma\boldsymbol{\nabla} N\boldsymbol{\nabla} c\cdot nds + \frac{C_e}{h}\int_{\Omega}\boldsymbol{\nabla} N\cdot n\boldsymbol{\nabla} c\cdot nds \tag{4.111}$$

The respective modulus can be defined using *tanh* function as

$$K(c) = K_1 f(c) + K_o(1 - f(c)) \tag{4.112}$$

where

$$f(c) = \frac{1}{2}(1 + tanh(4\pi c - 1.25\pi)) \tag{4.113}$$

4.8 Numerical result

In this section, we demonstrate the simulation framework through various case studies. First, we simulate the mechanical behavior of a membrane tube pulling problem. Subsequently, we dive into the modeling of diffusion and phase transformation on membranes to demonstrate the capability of the framework to model the coupled phenomena.

4.8.1 Membrane tube pulling

Many cell organelles and cytoplasmic projections are shaped as vesicles, tubes, or elongated membrane structures. Some examples of such shapes are the filopodia protrusions, inner mitochondrial region, endoplasmic reticulum, the Golgi complex, etc. These tubular structures play an important role in the locomotion of cells, production and folding of proteins, and in the formation of vesicles for transporting proteins and lipids among others. A typical mechanism for producing these tubular shapes involves motor proteins that attach to the cell membrane and pull it along the filaments of the cytoskeleton [71, 72]. Further, as is the case with the fission of endocytic vesicles, the tubular or vesicular structures also undergo constriction by scission proteins like dynamin [73–75]. This constriction mediates a membrane pinch-off mechanism that leads to the formation of vesicles. From a biophysical standpoint, it is important to gain a quantitative understanding of the interaction between the proteins and the membranes by determining the deformation mechanisms, forces exerted by proteins, and kinematic constraints.

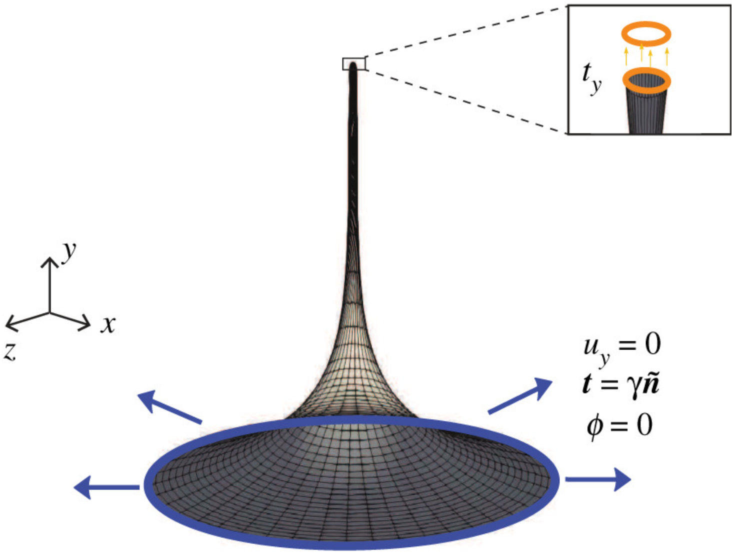

Figure 4.2: Schematic of the various membrane boundary value problems considered in this work. Shown are the geometry and boundary conditions for (a) formation of tubular shapes and their lateral constriction due to the application of axisymmetric constriction pressure, (b) Piezo1-induced membrane footprint generation, and (c) the budding of membranes due to the spontaneous curvature of the protein coats during endocytosis. Blue and orange colors identify the outer and inner rims, respectively.

A classic benchmark problem in the understanding of elongated biomembrane structures is the analytical model of the formation and interaction of membrane tubes proposed by Derényi et al [76]. Some key results of this model are the prediction of the magnitude of protein-membrane interaction forces and tubule radius, and their dependence on the membrane bending modulus (κ_B) and surface tension (γ). The protein pulling force, t_y, and the tubule radius, r, are related to the bending modulus and surface tension of the membrane as follows: $t_y \propto \sqrt{\kappa_B\ \gamma}$ and

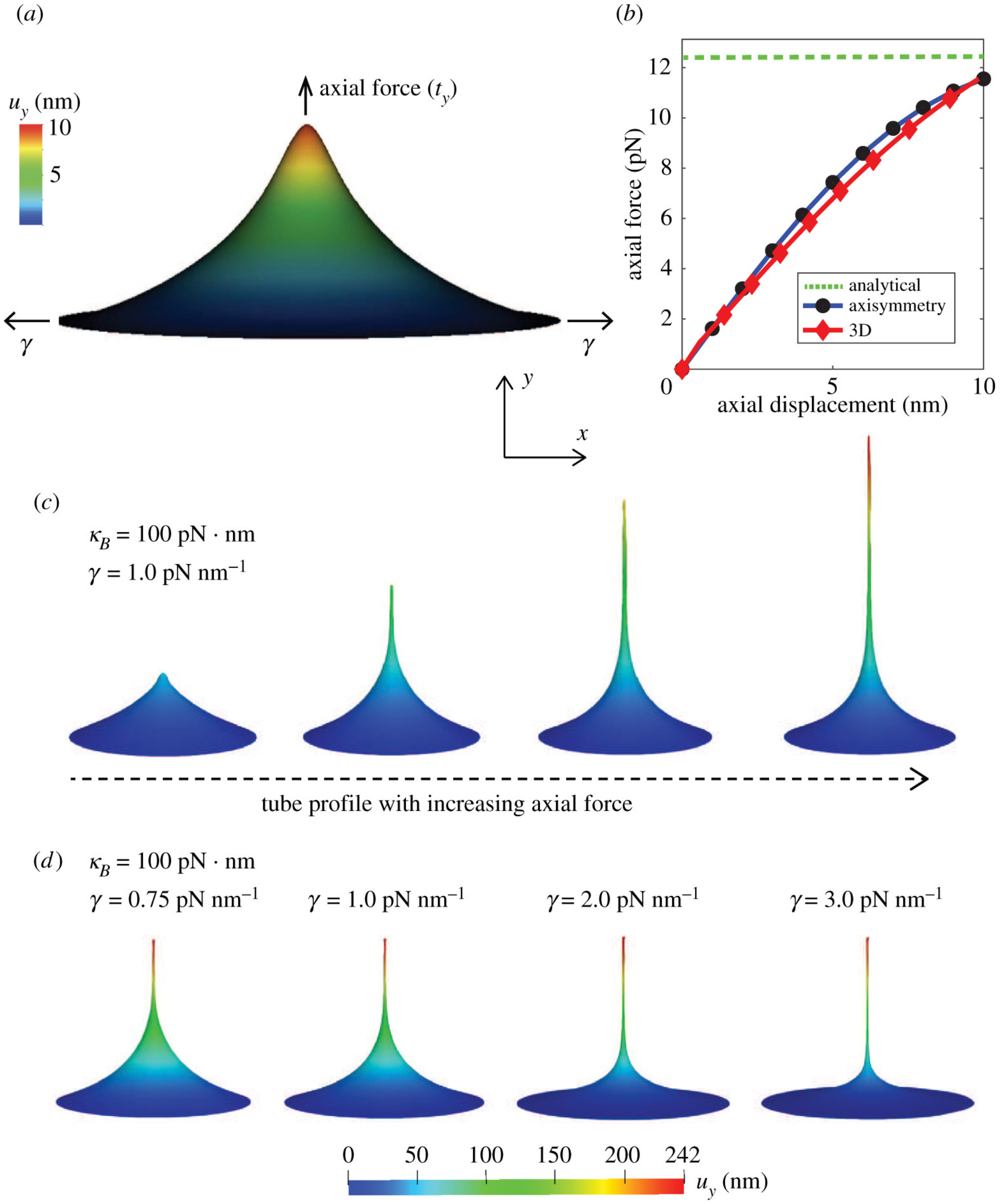

Figure 4.3: Deformation profile and force-displacement response of a membrane during tube pulling. Shown are the (a) deformation profile with the application of axial force on a membrane with a bending modulus of 20 pN-nm under a surface tension of 0.1 pN/nm, (b) comparison of the 3D force-displacement response with the axisymmetric solution and the equilibrium tube pulling force predicted by the analytical model, (c) progression of tube pulling with increasing axial force, and (d) dependence of the deformation profile and tube radius on the surface tension of the membrane.

$r \propto \sqrt{\kappa_B/\gamma}$. In addition to these analytical estimates, numerical solutions to the problem of membrane tube pulling, albeit with axisymmetric constraints on deformation, are available in the literature [77, 78] and in our earlier work [79]. We take advantage of the analytical estimates proposed by Derényi et al., the numerical solutions available from axisymmetric models [79], and validate the computational framework proposed in this work by comparing the load-displacement response of membrane tube pulling from these three approaches.

The boundary value problem solved, along with the spatial discretization (mesh), boundary conditions on the displacement ($\boldsymbol{u}$) and the membrane boundary slope (ϕ) are shown in 4.2(a). The simulation results are shown in 4.3: 4.3 (a) is the deformation profile obtained during tube pulling, and in 4.3 (b) is the load-displacement response of the 3D framework compared to the asymmetric result and the equilibrium value of tube pulling force predicted by the analytical model. We note that the analytical model only predicts the final equilibrium value of the tube pulling force, and hence only a single value of the force from the analytical model is plotted. As can be seen from 4.3(b), the 3D model very closely tracks the axisymmetric solution and asymptotically approaches the equilibrium value of force from the analytical solution. Further, we show the evolution of the deformation profile with increasing tube pulling force in 4.3(c), and the dependence of the deformation profile and tubule radius on the applied surface tension in 4.3(d). Here we note that the small deviation of the 3D model results from the axisymmetric solution in 4.3(b) is due to the fact that the 3D model boundary value problem is less constrained along the outer rim than the axisymmetric boundary value problem. For the 3D problem we enforce $u_y = 0$ along the outer rim, whereas the axisymmetric problem also enforces complete radial symmetry of the u_x and u_z displacements in addition to enforcing $u_y = 0$ (See 4.2(a)). This makes the axisymmetric problem more stiff to the applied load.

4.8.2 Diffusion on curved manifold

Next, we model diffusion on rigid geometries. We compare the diffusion on a plate with radius $1nm$, $100nm$ and 10^7nm respectively, to study the effect of diffusion on curvature. These plates have the same length of $5.75nm$ and unit width each, thus having the same area. The initial condition is that there is a concentration, $c = 1$ on one end of the respective plate and zero everywhere else. Due to this dirichlet boundary condition, the concentration diffuses to the other end. The geometry of the plates is depicted in Fig. 4.4.

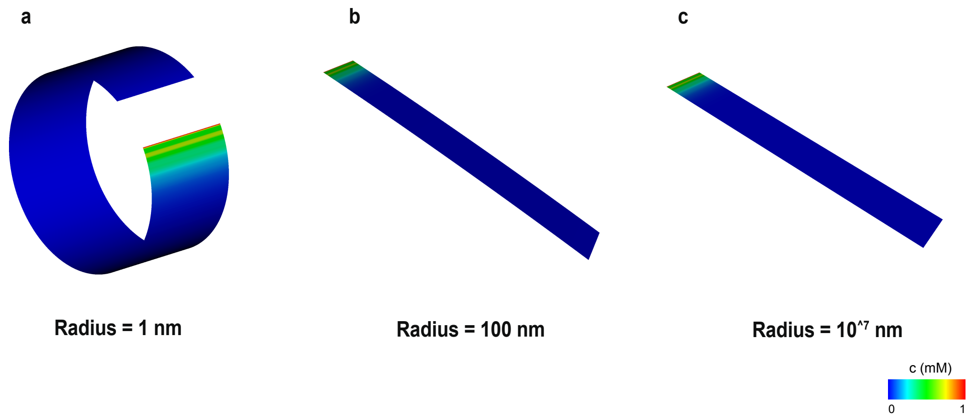

Figure 4.4: Geometry of the plates having distinct radius to study the role of curvature on diffusion.

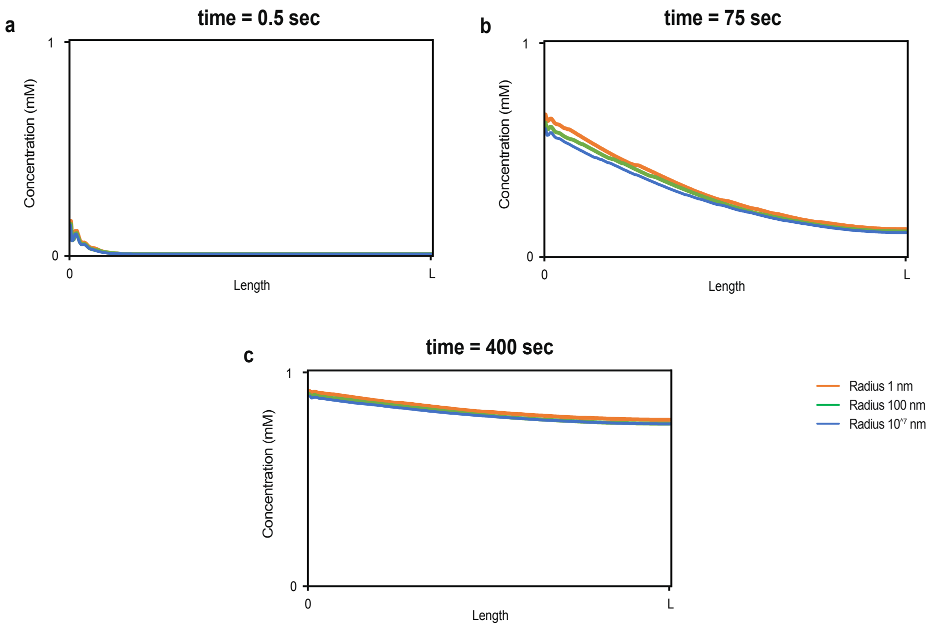

Figure 4.5: Evolution of concentration upon diffusion on curved plates, all having the same diffusion area.

The plots of evolution of the concentration upon diffusion along the different plates at various times is presented in Fig. 4.5. We note that the diffusion is faster in the comparably highly curved manifold. Similar results have been presented in [64]. This can be seen from the diffusion equation. The surface gradient is higher in the curved manifold having larger curvature, thus leading to a higher net diffusivity. Analytical result for diffusion on a cylindrical manifold with a constant mean curvature and zero gaussian curvature have been presented in [62].

4.8.3 Phase transformation on manifolds

Next, we study phase transformation using Cahn-Hilliard dynamics on various two dimensional surfaces embedded in the 3D space. First, we demonstrate phase segregation on a flat surface as in Fig. 4.6. The initial concentration is $c = 0.65 \pm 0.05$ with periodic boundary conditions. We notice the evolution of the concentration as it would be using the traditional two dimensional volumetric mesh.

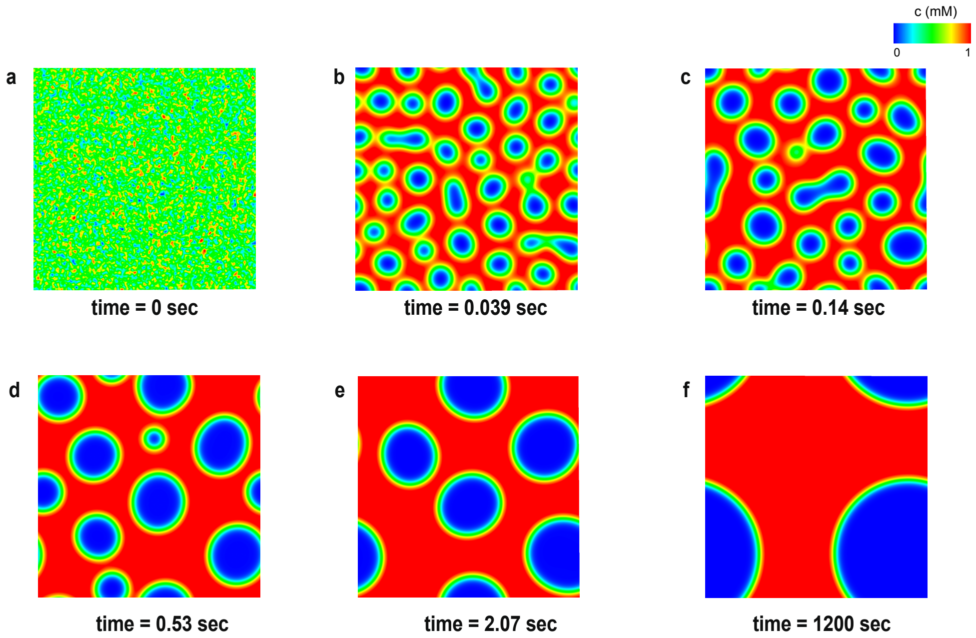

Figure 4.6: The spatial evolution of the phases on a flat surface using the fourth order mass conserving Cahn-Hilliard dynamics.

After studying the phase transformation on a planar surface, we now move to modeling a cylindrical manifold. A cylinder has a constant mean curvature and a zero gaussian curvature. The initial and the boundary conditions are the same as for the previous case of flat surface. We notice the phase evolution as in Fig. 4.7. We notice that phase segregation on this geometry takes longer as compared with the planar surface.

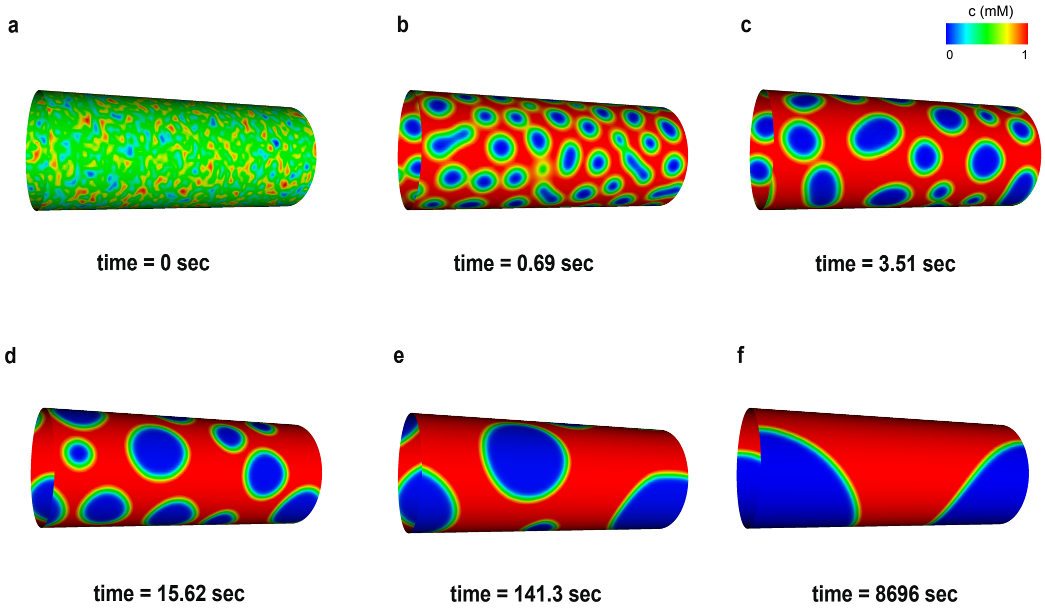

Figure 4.7: The spatial evolution of the phases on a cylinder manifold using the fourth order mass conserving Cahn-Hilliard dynamics.

Finally, we consider the geometry of a sphere and an ellipsoid. Both these geometries have non zero mean and gaussian curvature with the same initial/ boundary conditions as for the previous cases. We clearly observe the neat evolution of the phases which has a critical role for modeling the behavior of proteins on the cell membrane. The results are depicted in Fig. 4.8, 4.9.

4.8.4 Phase transformation coupled to mechanics

In this subsection, we add mechanics to the phase transformation phenomena on surface manifolds. For mechanics, we consider a solid shell with the material model of neo-hookean in-plane and Koiter energy for out of plane bending. There is an internal pressure inside the geometry acting on the respective surfaces considered here. The distinct modulus of the respective phases, that arise due to the concentration difference, leads to the complex shapes produced. The profiles of the

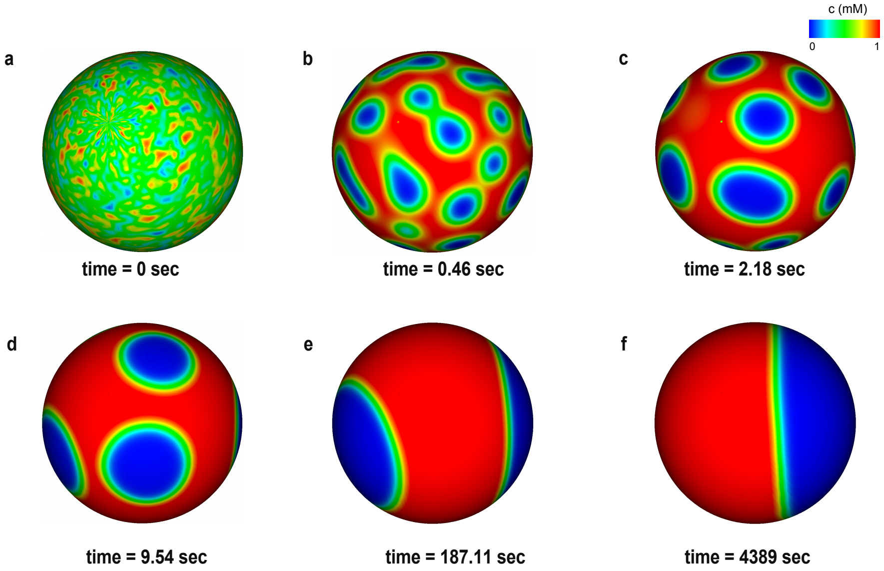

Figure 4.8: The spatial evolution of the phases on a two dimensional sphere manifold embedded in the 3D space using the fourth order mass conserving Cahn-Hilliard dynamics.

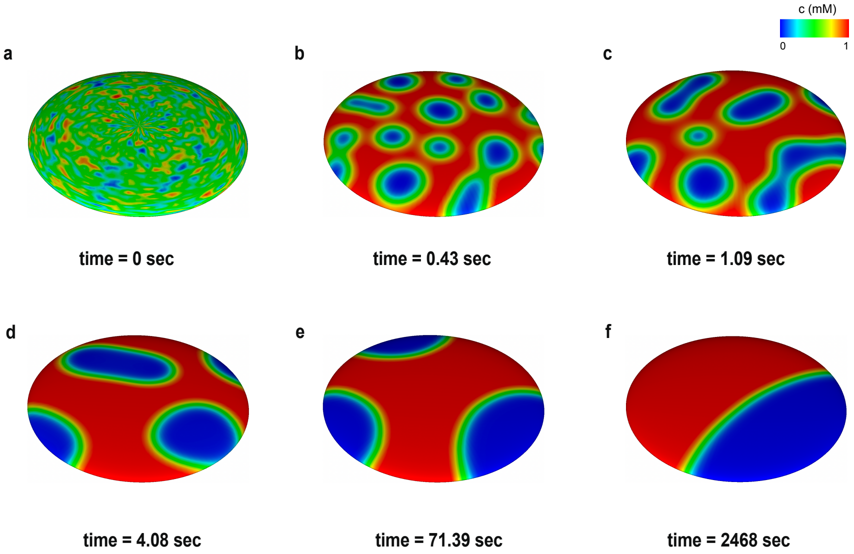

Figure 4.9: The spatial evolution of the phases on an ellipsoid with double major axis using the fourth order mass conserving Cahn-Hilliard dynamics.

geometries considered, a cylinder, sphere can be appreciated from Fig. 4.10, 4.11. The temporal simulation results in the segregation of phases. The difference in the mechanical modulus such as the bulk modulus, shear modulus, bending modulus

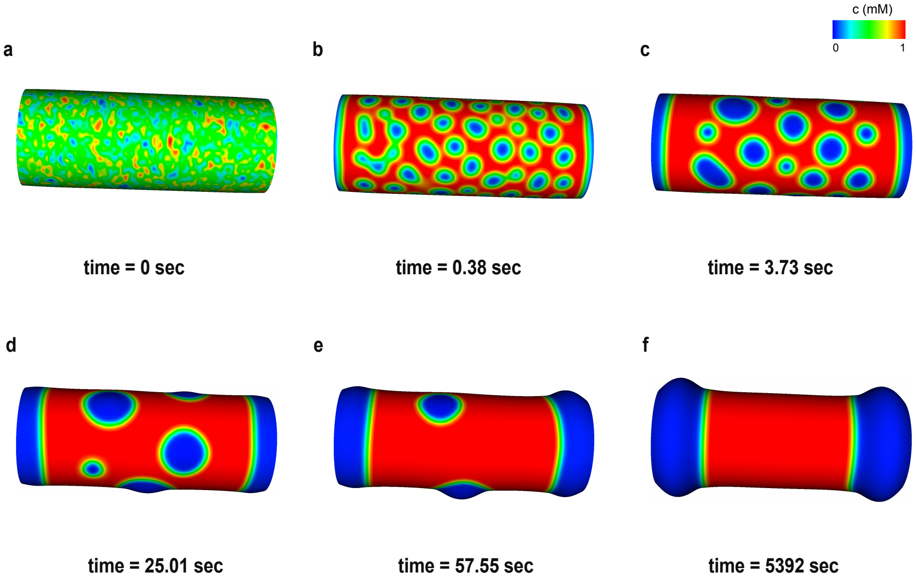

Figure 4.10: Mechanical in-plane and out of plane bending coupled with Cahn-Hilliard in-plane phase transformation dynamics on a cylindrical manifold. The evolution profile of the cylinder due to the phase separation coupled to the intrinsic curvature of the phases can be clearly observed.

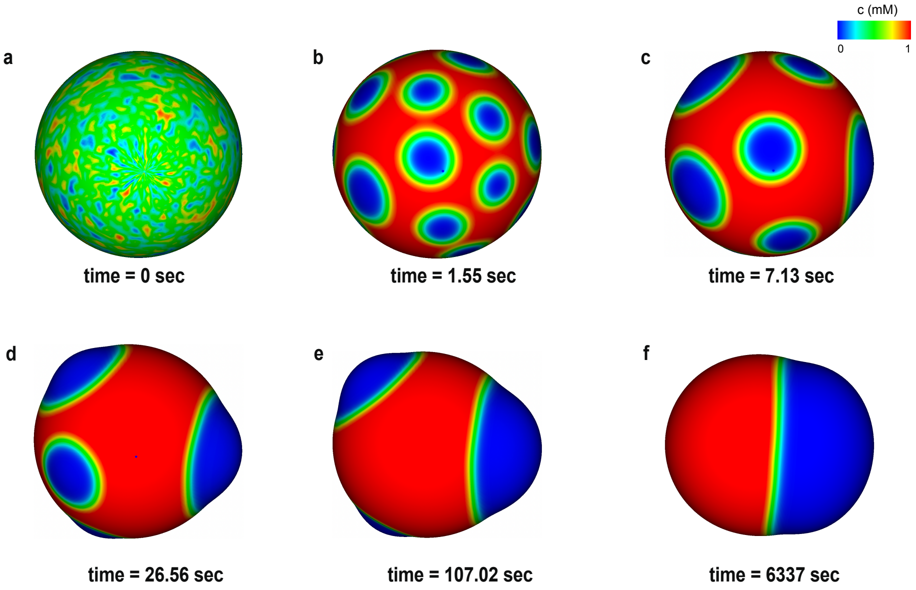

Figure 4.11: Mechanical deformations coupled with in-plane phase transformations on a spherical manifold.

etc leads to different intrinsic curvatures of the respective concentration region. The initial condition on concentration is $c = 0.65 \pm 0.05$. One end of the respective geometry is fixed. A displacement multiplier of 3 is applied to visualize the numerical simulations.

4.8.5 Role of curvature on phase transformation

The goal of this part of the chapter is to understand the role of curvature on the phase transformation besides the effect of geometry on phase segregation. Using the coupled mechanics-phase transformation numerical framework, we consider the following boundary value problem. Consider a boundary value problem consisting of an initial flat plate whose two ends are fixed and is indented at the center. The maximum displacement of the plate keeps on increasing at every timestep. Modeling this using finite element techniques, we observe that phase segregation reaches near equilibrium upon a critical mean curvature. This is the stage $\boldsymbol{c}$ in Fig. 4.12. Next, we consider reducing the indentation load. Upon decreasing the load, the maximum displacement and thus the mean curvature decrease and we observe that the phase segregation continues to take place until completion. We can conclude from this simulation that higher mean curvature reduces the mobility of phase segregation. This numerical result is of great interest as unlike diffusion, an analytical solution for fourth order partial differential equation of Cahn-Hilliard is extremely complex to compute.

4.9 Conclusion

Membrane morphology plays a critical role in membrane microstructure. We started this chapter by appreciating the relevance as well as the physics of modeling phase transformation on a two dimensional manifold embedded in the three dimensional space. Detailed discussions on the mathematical background, Kirchoff-Love shell kinematics, equilibrium equations, finite element formulation of Cahn-Hilliard coupled with shell mechanics is presented in the chapter. The coupling of the Cahn-Hilliard and out of plane deformation leads to the special existence of the Korteweg stress, which is absent when phase transformations are modeled on a volumetric

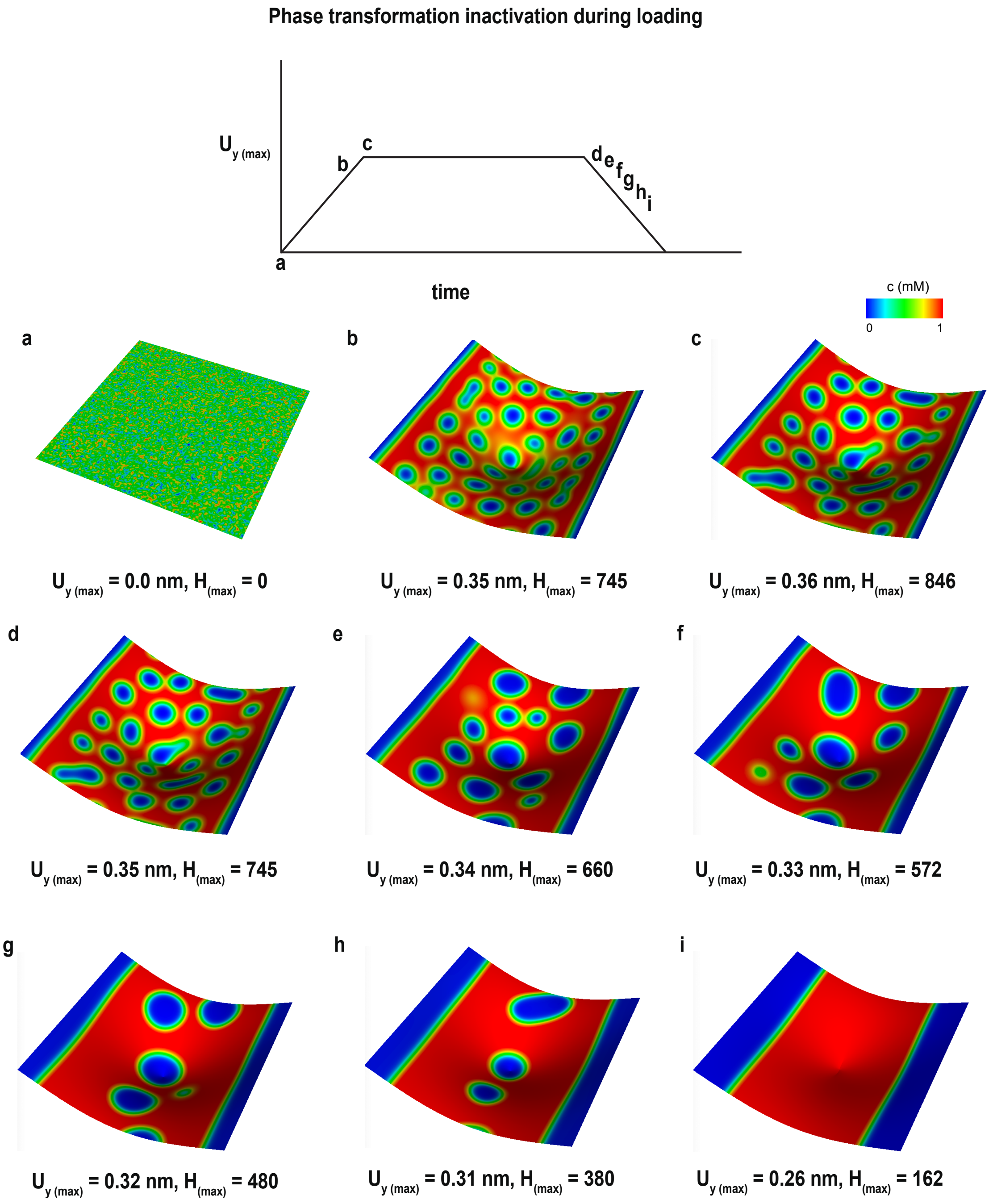

Figure 4.12: Inactivation of phase segregation upon mechanical loading.

surface. During phase transformation, when two miscible phases are brought into contact, it leads to immediate diffusion. If however, this timescale of the diffusion process is slow, large concentration gradients exist at the interface of the phases, which leads to the presence of an interfacial tension. The Korteweg stress represents this interfacial tension. The role of curvature on diffusion and phase transformation is also presented. While reaction-diffusion models of phase separation have demonstrated the formation of hexagonal patterns due to curvature [80], here we model the mass conserving phase transformation using Cahn-Hilliard dynamics and noticed no change in pattern formation controlled by curvature. We demonstrate the role of curvature on surface diffusion and thereby on surface phase transformation phenomena through a few numerical simulations.

Chapter 5

Conclusion and Future work

5.1 Conclusion

In this thesis, we started by appreciating the mechano-electro-chemo integrity of the brain at the neuron scale. The mathematical treatment is followed by a presentation of a novel modeling scheme of spatio-temporal propagation of action potential that incorporates some recent advances in the understanding of neuronal signal propagation. The numerical modeling of action potential propagation along the neuronal axons is discussed in detail in Chapter 2. Brief overview of the existing electrical networks to model the electrical propagation is followed by demonstration of novel modeling of spatio-temporal propagation of action potential incorporating the recent advances to the signal propagation. This numerical framework is capable of acting as a digital twin to various neuronal electro-physiological experiments such as patch-clamp experiment, monitoring the voltage propagation via dyeing calcium ions or via voltage imaging etc. The remarkable resolution of the primary and various derived fields in the numerical model can supplement the experimental outcomes for a far greater understanding of the neuronal structure, which is desired to understand the neuronal diseases. Numerical estimates of action potential conduction velocity are also presented.

Electrodiffusive modeling in Chapter 2 is extended to include the dendrites and the soma region in Chapter 3. The forward propagation of the action potential along the neuronal axons as presented in the previous Chapter is supplemented with the backpropagation into the dendritic spines. It is believed that the neurons modulate the action potential using the spine geometry etc. The role of spine geometry in modulation of the potential is demonstrated. Like in the modeling of axonal signal propagation in the previous Chapter, this work on the dendritic and the soma region can be used in conjunction with experimental observations to get a better understanding of neurological functioning and disorders.

Similar to electrical propagation in neurons, it is of utmost importance to reliably understand various mechanical metrics (stress, strain, rate dependence, residual stress, etc.) that lead to neuronal injury. Numerical models have the capability to precisely incorporate various length-scales and time-scales of the constitutive visco-elasto-dynamic response by modeling the various mechanical elements of the microstructure of the neuron. Existing tissue-scale numerical models of the brain are too homogenized to incorporate these intricate neuronal microstructure details that are necessary to understand neuronal injury. Towards this goal, a constitutive model of the viscoelastic response relevant to neuronal deformation is presented in the Appendix. This framework, when fully developed, is capable of acting as a digital twin for neuronal loading and impact experiments. Eventually, this framework is expected to numerically estimate injury curves characterizing neuronal injury in the phase space of strain and strain rate.

Surface diffusion and phase transformation on biomembranes is of great interest to elucidate our understanding of biophysical membrane mechanisms. Invariably, many of these transport processes occur on curved cell membranes and are responsible for assembling and transporting various membrane-bound protein structures. Traditionally, the effect of curvature on diffusion has been relatively neglected, but in recent years, their is an increased interest in understanding and modeling curvature effects. Phase transformation on membranes constitute another important category of problems that are critical to understand various membrane-bound phenomena. In this work, a numerical model adopting Kirchhoff-Love shell kinematics, equilibrium equations and the constitutive equations is presented. The coupling of the in-plane phase transformations to the out of plane deformation is modeled. The presence of Korteweg stress, which arises due to the inherent coupling of surface gradients, is noted. The numerical results demonstrate curvature effects on surface diffusion and distribution of the constitutive phase.

5.2 Future work

This dissertation presents numerical frameworks for modeling various volumetric and surface phenomena in biological cells and their membranes, and can be further extended to describe various coupled multiphysics interactions. An example is to couple the action potential propagation along the neuronal axons to their mechanical deformation. The resulting model can be expected to provide good insights into the modulation and disruption of electrical signals due to neuronal deformation. Further, the spatio-temporal action potential propagation model presented in this work to model signal propagation in the axons, some and dendrites can be used be study various physiological disease conditions, in addition to TBI. Extending this model to permit for synaptic ionic transport and associated action potential propagation will allow us to model synapse-bound physiological disease conditions, including Alzheimer's and Depression.

Appendix A

Nonlinear finite-strain viscoelastic and visco-elasto-dynamic modeling of neuronal axons

A.1 Introduction

This chapter presents the constitutive framework for the numerical modeling of brain via a bottom-up approach i.e. the viscoelastic response to mechanical deformation at the cellular level. As discussed in the introductory chapter, the mechanical response of the neurons is critical to the entire functioning of the brain as a whole. In this chapter, we start by reviewing the physiology of a neuron. Based on the micro-environment of the neuron, a viscoelastic network of respective regions such as the cytoskeleton, the membrane, and the extra-cellular region is formulated. Important work has been done in this context by Rooij et al [81]. For each of the respective regions, the key load bearing constitutive proteins are noted and a representative viscoelastic network is identified. The kinematics and the finite-strain constitutive viscoelastic modeling is discussed subsequently. A micro model consisting of a single neuron and a macro model consisting of a group of neurons are considered as the reference domain respectively.

A.2 Physiology of a neuron and internal structure of an axon

The neuronal physiology is briefly reviewed in this section. We know that a neuron consists of a cell body which has various organelles such as the nucleus. An axon or the nerve fiber transmits electrical signal away from the cell body towards the synaptic terminals. The goal of this chapter is to model the viscoelastic behavior of the neuronal axon since an axon bears the primary load under various loading conditions. The load bearing components of the axon are depicted in Fig. A.1. The neuronal membrane is made up of the lipid bilayers. The load bearing proteins in the intra-cellular region comprise of the microtubules, tau proteins and the actin filament.

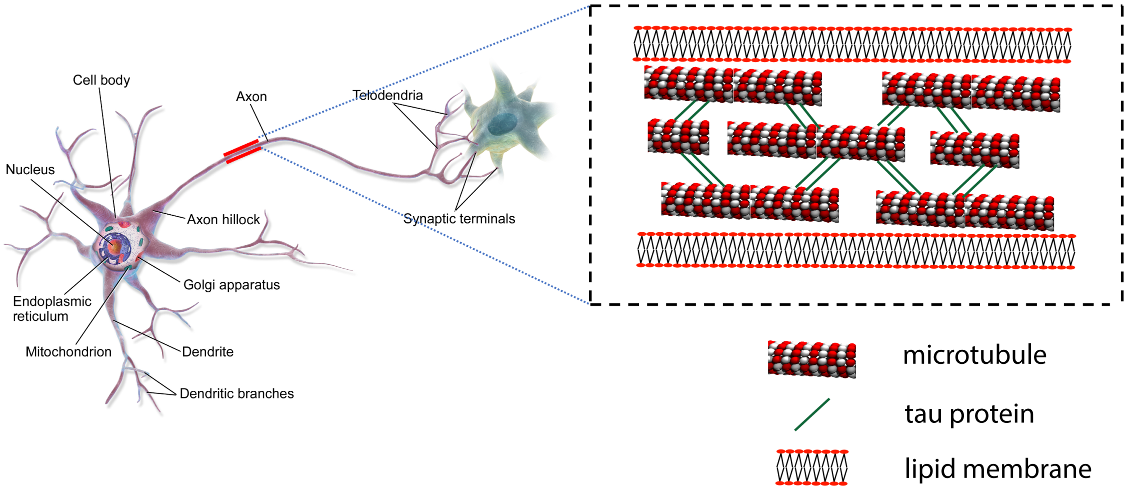

Figure A.1: Various components present in the neuron for the physiological functioning of the cell. A zoomed-in portion of an axon depicting the primary load bearing proteins namely microtubule, tau protein is demonstrated on the right. Figure inspired from [82]

The two dimensional microstructure of the micro model consisting of a single neuron and the key load bearing constitutive proteins in the cytoskeleton are depicted in Fig. A.2. The outside region of the microstructure, marked in green, is the extra-cellular matrix (ECM). The membrane, marked in orange, consists of lipid bilayers. The cytoskeleton region consisting of primary mechanical load sharing proteins is depicted in blue, with the other constitutive proteins demonstrated in red to provide the tensegrity effect. An equivalent network capable of representing the mechanical viscoelastic behavior for the different regions in the neuronal microstructure is discussed in the following subsections. A standard linear solid (SLS) model is selected for the membrane.

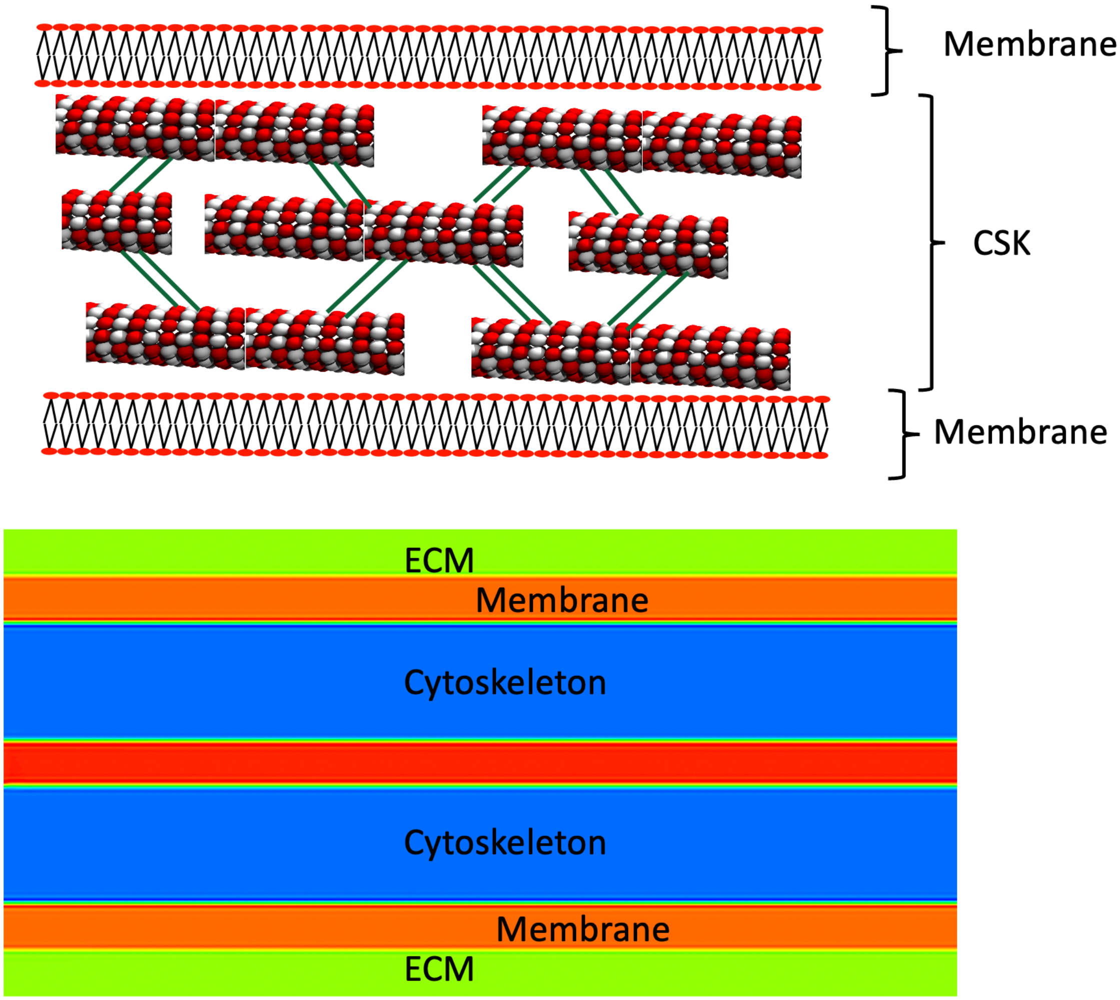

Figure A.2: Axonal microstructure having various continuum regions such as the cytoskeleton, membrane and the extra-cellular matrix. This domain consisting of a single neuron constituents, forms the micro model.

A.2.1 Cytoskeleton

The neuronal cytoskeleton is an intricate accumulation of proteins as can be seen in Figure A.3 (a). It consists of various proteins such as longitudinally aligned microtubules, actin filament near the membrane, actin ring along the circumference of the membrane, and various crosslink proteins such as tau protein, dynein protein, myosin protein etc. The microtubule and actin filament provide considerable strength to the axon. Tau and dynein protein interlink the microtubule proteins, dynein in-addition crosslinks actin filaments to microtubule proteins and myosin interlinks the actin filaments. To realize the complex interplay of load sharing between the load bearing components like the microtubule or actin filaments and the various crosslink proteins, an equivalent viscoelastic network is constructed as in Figure A.3 (b). The first branch of the viscoelastic network represents the stiffness and viscosity of the tau and dynein crosslink proteins. The second and the third branch represent the behavior of the actin filament and the microtubule protein respectively. The crosslink between the second and the third branch is due to the presence of the dynein protein that crosslinks actin protein with the microtubule proteins.

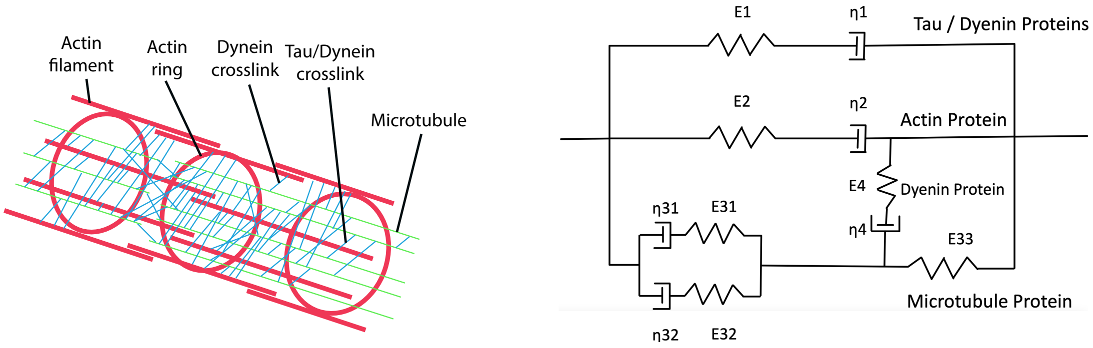

Figure A.3: The intricate structure of the neuronal axon formed by the various constitutive proteins. The proteins such as tau, dynein, myosin provide a crosslink for the microtubule and actin filament. An equivalent continuum viscoelastic network to realize this behavior is presented in the right. The stiffness and viscosity of the respective proteins builds up this viscoelastic mechanical model. Figure inspired from [81]

A.2.2 Extracellular Matrix (ECM)

Figure A.4 (a) presents the various proteins present in the extra-cellular region of the neuron. Glial cells like the oligodendrocytes are present in the vicinity of the neuronal membrane and provide strength to the axon. Proteins such as the collagen, fibronectin, proteoglycan etc are responsible for providing viscoelastic mechanical strength to the ECM. As we go far from the membrane into the ECM, the elastin protein is present in abundance and is primarily responsible for the providing elasticity to the mechanical structure. The equivalent viscoelastic network taking into account the presence of these proteins is presented in Figure A.4 (b). Each of the branch represents the stiffness and viscosity of the respective protein. The glial cells, collagen, fibronectin and proteoglycan act in parallel and in series with the pure elastic stiffness of the elastin protein. The elasticity of the elastin protein causes the skin to come back to its initial position when pinched. The equivalent viscoelastic network thus faithfully represents the behavior of the ECM.

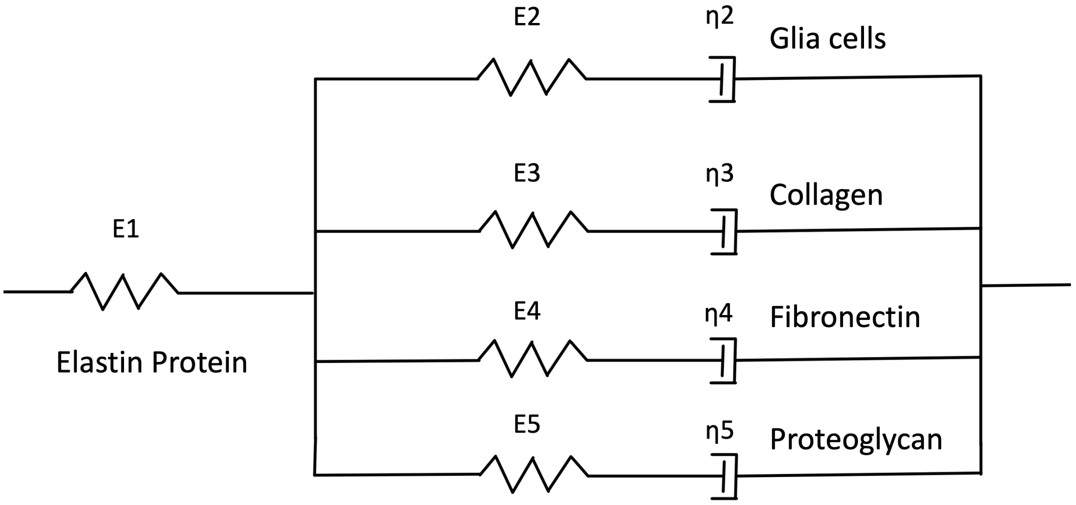

Figure A.4: The constitutive proteins in the ECM comprise of collagen, fibronectin, proteoglycan, elastin and various glial cells such as oligodendrocyte. The elastic stiffness of the elastin coupled to the stiffness and viscosity of the various proteins builds up the equivalent viscoelastic network.

A.3 Continuum modeling

Here we discuss the continuum mechanical modeling of the viscoelastic network. A detailed description of the modeling is present in [83].

A.3.1 Kinematics

Consider a body, Ω_O in the reference configuration which gets deformed to its current configuration, Ω. Any point in the reference configuration is denoted as $\mathbf{X}$. Upper case indices are used to represent the components of the tensors denoting the quantities in the reference configuration while the lower case indices are put into use for the components in the current configuration. The deformation gradient is $\mathbf{F} = \partial\varphi/\partial\mathbf{X} = \mathbf{1} + \partial\mathbf{x}/\partial\mathbf{X}$, where $\varphi(\mathbf{X}, t) = \mathbf{X} + \mathbf{u} = \mathbf{x}$, is the deformation map between the reference and the current configuration and $\mathbf{u}$ is the displacement field. In the coordinate notation, the deformation gradient is given by $F_{iJ} = \delta_{iJ} + \partial u_i/\partial X_J$ and the Green-Lagrange strain is expressed as $E_{IJ} = \frac{1}{2}(F_{kI}F_{kJ} - \delta_{IJ})$. The deformation gradient can be split into volumetric and deviatoric response as,

$$\boldsymbol{F} = J^{\frac{1}{3}}\bar{\boldsymbol{F}}, \qquad J = det(\boldsymbol{F})$$

where $\bar{\boldsymbol{F}}$ is the deviatoric part,

$$det(\bar{\boldsymbol{F}}) = 1 \tag{A.1}$$

The Green-Lagrange strain, $\boldsymbol{E}$, and the right Cauchy-Green tensor, $\boldsymbol{C}$, along with their volumetric counterparts can be expressed as

$$\begin{aligned} \boldsymbol{C} &= \boldsymbol{F}^T\boldsymbol{F}, \qquad \boldsymbol{E} = \frac{1}{2}(\boldsymbol{C} - \mathbf{1}) \\ \bar{\boldsymbol{C}} &= \bar{\boldsymbol{F}}^T\bar{\boldsymbol{F}}, \qquad \bar{\boldsymbol{E}} = \frac{1}{2}(\bar{\boldsymbol{C}} - \mathbf{1}) \end{aligned}$$

Using variational technique, one can compute the following partial derivatives that will be used in the further course of action.

$$\begin{aligned} \partial_{\boldsymbol{C}}\bar{\boldsymbol{C}} &= J^{-\frac{2}{3}}[\mathbf{I} - \frac{1}{3}\boldsymbol{C} \otimes \boldsymbol{C}^{-1}] \\ \partial_{\boldsymbol{C}}J &= \frac{1}{2}J\boldsymbol{C}^{-1} \end{aligned}$$

A.3.2 Constitutive model

Consider a free-energy density functional of the form,

$$\psi(\boldsymbol{C}, \mathbf{Q}_i) = W(\boldsymbol{C}) - \sum_{i=1}^{N} \frac{1}{2} \bar{\boldsymbol{C}} : \mathbf{Q}_i + \Omega\big(\sum_{i=1}^{N} \mathbf{Q}_i\big) \tag{A.2}$$

where $\mathbf{Q}_i$ are the internal variables that represent the inelastic strain due to the presence of the dashpot in the network, W is the elastic free energy density functional, Ω is a dissipative functional and N is the number of viscoelastic Maxwell branches in parallel. From second law of thermodynamics, we know,

$$-\dot{\psi}(\boldsymbol{C}, \mathbf{Q}_i) + \frac{1}{2} \boldsymbol{S} : \dot{\boldsymbol{C}} \geq 0 \tag{A.3}$$

where $\boldsymbol{S}$ is the second Piola-Kirchoff stress tensor. From equation A.2,

$$\dot{\psi}(\boldsymbol{C}, \mathbf{Q}_i) = \big(\partial_{\boldsymbol{C}} W(\boldsymbol{C}) - J^{-\frac{2}{3}} \sum_{i=1}^{N} \frac{1}{2} DEV[\mathbf{Q}_i]\big) : \dot{\mathbf{C}} - D(\boldsymbol{C}, \mathbf{Q}_i, \dot{\mathbf{Q}}_i) \tag{A.4}$$

where D is a dissipative function as,

$$D(\boldsymbol{C}, \mathbf{Q}_i, \dot{\mathbf{Q}}_i) = -\partial_{\mathbf{Q}_i} \psi : \dot{\mathbf{Q}}_i = [\frac{\dot{\boldsymbol{C}}}{2} - \partial_{\mathbf{Q}_i} \Omega(\sum_{i=1}^{N} \mathbf{Q}_i)] : \dot{\mathbf{Q}}_i \tag{A.5}$$

This results in

$$\big(\frac{\boldsymbol{S}}{2} - \partial_{\boldsymbol{C}} W(\boldsymbol{C}) + \frac{1}{2} J^{-\frac{2}{3}} \sum_{i=1}^{N} DEV[\mathbf{Q}_i]\big) : \dot{\boldsymbol{C}} + D(\boldsymbol{C}, \mathbf{Q}_i, \dot{\mathbf{Q}}_i) \geq 0 \tag{A.6}$$

Thus, the following must hold;

$$\mathbf{S} = 2\partial_{\boldsymbol{C}} W(\boldsymbol{C}) - J^{-\frac{2}{3}} \sum_{i=1}^{N} DEV[\mathbf{Q}_i] \tag{A.7}$$

Next, consider the break-up of the stored energy functional into the volumetric and volume preserving parts as,

$$W(\boldsymbol{C}) = U(J) + \bar{W}(\bar{\boldsymbol{C}}) \tag{A.8}$$

The initial second Piola-Kirchoff stress can thus be computed.

$$\boldsymbol{S}^o = 2\partial_{\boldsymbol{C}} W(\boldsymbol{C}) = 2U^{'}(J)\partial_{\boldsymbol{C}} J + 2\partial_{\bar{\boldsymbol{C}}} \bar{W}(\bar{\boldsymbol{C}}) : \partial_{\boldsymbol{C}} \bar{\boldsymbol{C}} \tag{A.9}$$

$$\boldsymbol{S}^o = JU^{'}(J)\boldsymbol{C}^{-1} + 2J^{-\frac{2}{3}}\big[2\partial_{\bar{\boldsymbol{C}}}\bar{W}(\bar{\boldsymbol{C}}) - \frac{1}{3}\big(\partial_{\bar{\boldsymbol{C}}}\bar{W}(\bar{\boldsymbol{C}}) : \boldsymbol{C}\big)\boldsymbol{C}^{-1}\big] \tag{A.10}$$

The complete second Piola-Kirchoff stress for the viscoelastic network is governed by,

$$\boldsymbol{S} = \boldsymbol{S}^o - J^{-\frac{2}{3}} DEV[\sum_{i=1}^{N} \boldsymbol{Q}_i] \tag{A.11}$$

For viscoelastic networks, the evolution of the internal variables is governed by the following equation, where γ_i constitute the relaxation function.

$$\dot{\boldsymbol{Q}}_i + \frac{1}{\tau_i}\boldsymbol{Q}_i = \frac{\gamma_i}{\tau_i} DEV[2\partial_{\bar{\boldsymbol{C}}}\bar{W}(\bar{\boldsymbol{C}})] \tag{A.12}$$

and

$$\lim_{t\to-\infty}\boldsymbol{Q}_i = 0$$

Solving, we get

$$\boldsymbol{Q}_i = \frac{\gamma_i}{\tau_i}\int_{-\infty}^{t} e^{\frac{-(t-s)}{\tau_i}} DEV[2\partial_{\bar{\boldsymbol{C}}}\bar{W}(\bar{\boldsymbol{C}}(s))]ds \tag{A.13}$$

The second Piola-Kirchoff stress response function is then obtained as

$$\boldsymbol{S}(t) = JU^{'}(J)\boldsymbol{C}^{-1}(t) + J^{-\frac{2}{3}}(t)\int_{-\infty}^{t} g(t-s)\frac{d}{ds}\big(DEV(2\partial_{\bar{\boldsymbol{C}}}\bar{W}(\bar{\boldsymbol{C}}(s)))\big)ds \tag{A.14}$$

where $g(t)$ is the relaxation function of the viscoelastic model.

A.4 Concluding remarks

A bottom-up approach for modeling the viscoelastic mechanical behavior for the neuronal axons is demonstrated. An equivalent viscoelastic network of respective regions in the neuronal microenvironment considering the constitutive proteins is constructed. The kinematics and the constitutive model for the finite strain numerical framework is presented.

Appendix B

Supplemental information for neuronal electro-diffusive modeling

B.1 Hodgkin-Huxley activation/inactivation parameters

n, m and h represent the potassium channel activation, sodium channel activation, sodium channel inactivation and are dimensionless quantities between 0 and 1, relating the ionic flux of the respective ions across the neuronal membrane. These are described by the following ODE's:

$$\frac{dn}{dt} = \alpha_n(V_m)(1-n) - \beta_n(V_m)n \tag{B.1}$$

$$\frac{dm}{dt} = \alpha_m(V_m)(1-m) - \beta_m(V_m)m \tag{B.2}$$

$$\frac{dh}{dt} = \alpha_h(V_m)(1-h) - \beta_h(V_m)h \tag{B.3}$$

The rate constants α_i, β_i are given by

$$\alpha_n(V) = \frac{0.01(10-V)}{\exp(\frac{10-V}{10})-1}, \qquad \beta_n(V) = 0.125\exp(\frac{-V}{80}) \tag{B.4}$$

$$\alpha_m(V) = \frac{2.5 - 0.1V}{\exp(\frac{25-V}{10}) - 1}, \qquad \beta_m(V) = 4\exp(\frac{-V}{18}) \tag{B.5}$$

$$\alpha_h(V) = 0.07\exp(\frac{-V}{20}), \qquad \beta_h(V) = \frac{1}{\exp(\frac{30-V}{10}) + 1} \tag{B.6}$$

B.2 Leak current

The leak current controls the hyperpolarization phase of the action potential propagation and therefore ensures that the membrane potential comes back to its resting state after the signal has propagated. The following expression for the leak current is adopted [84]. Note that this leak is active only at the nodes of Ranvier when the myelin sheaths are present.

$$I_K^{leak} = g_K^{leak}(V - E_K) \tag{B.7}$$

$$I_{Na}^{leak} = g_{Na}^{leak}(V - E_{Na}) \tag{B.8}$$

B.3 Ionic pumps

The expression for the ionic pumps embedded in the neuronal membrane is mentioned below and is adapted from [85–87]. The role of the ionic pumps is to replenish the respective ionic concentration in the intracellular region to its resting state concentration after the propagation of the action potential. In some simulations, ionic pump term is ignored for better visualization of the respective fields.

$$I_K^{pump} = -2I_{max}A_{pump}$$

$$I_{Na}^{pump} = 3I_{max}A_{pump}$$

$$A_{pump} = \Big(1 + \frac{k_K}{c_K^e}\Big)^{-2}\Big(1 + \frac{k_{Na}}{c_{Na}^i}\Big)^{-3}$$

Here k_i are the Michaelis-Menten dissociation constants for the respective ion, c_K^e is the local concentration of potassium in the extracellular region and c_{Na}^i is the local concentration of sodium ions in the intracellular region.

B.4 Table of Parameters

Parameter	Value	Description
R	$8.31454\ J \cdot mole^{-1} \cdot K^{-1}$	Gas constant
T	$279.45\ K$	Temperature
F	$96485\ C \cdot mole^{-1}$	Faraday constant
D_{Na}	$1.33\ \mu m^2 \cdot ms^{-1}$	Diffusion coefficient of sodium ion
D_K	$1.96\ \mu m^2 \cdot ms^{-1}$	Diffusion coefficient of potassium ion
D_{Cl}	$2.0\ \mu m^2 \cdot ms^{-1}$	Diffusion coefficient of chloride ion
ϵ_o	$8.88541\ e^{-12} C \cdot m^{-1} \cdot V^{-1}$	Electric permittivity in vacuum
ϵ_w	80.0	Relative dielectric permittivity of water
g_{Na}^{leak}	$0.065\ mS/cm^2$	leak conductance of Na^+
g_K^{leak}	$0.435\ mS/cm^2$	leak conductance of K^+

Table B.1: Constants used in the electro-diffusive model simulations

Parameter	Value	Description
c^i_{Na}	12 mM	Initial intracellular concentration of Na^+
c^i_K	155 mM	Initial intracellular concentration of K^+
c^i_{Cl}	slightly exceeds 167 mM	Initial intracellular concentration of Cl^-
c^e_{Na}	145 mM	Initial extracellular concentration of Na^+
c^e_K	4 mM	Initial extracellular concentration of K^+
c^e_{Cl}	149 mM	Initial extracellular concentration of Cl^-
r	238 μm	Radius of squid axon

Table B.2: Neuronal parameters used for the squid axon [22, 23]

Parameter	Value	Description
c^i_{Na}	10 mM	Initial intracellular concentration of Na^+
c^i_K	140 mM	Initial intracellular concentration of K^+
c^i_{Cl}	exceeds 150.0 mM	Initial intracellular concentration of Cl^-
c^e_{Na}	155 mM	Initial extracellular concentration of Na^+
c^e_K	3.5 mM	Initial extracellular concentration of K^+
c^e_{Cl}	158.5 mM	Initial extracellular concentration of Cl^-
r	0.55 μm	Radius of rat axon

Table B.3: Neuronal parameters used to model the rat axon [11, 88]

Parameter	Value	Description
C_m	1.0 $\mu F/cm^2$	Membrane capacitance
R_i	38.18 Ωcm	Computed axial resistance along the axon

Table B.4: Squid axon values used for the PNP model to generate Figure 4

Parameter	Value	Description
C_m	1.45 $\mu F/cm^2$	Membrane capacitance
C_{my}	0.166 $\mu F/cm^2$	Myelin capacitance
l_I	70 μm	Internodal distance
l_{NOR}	5.0 μm	Length of node of Ranvier
l_A	1500 μm	Total length of the neuronal axon

Table B.5: Rat axon values used for the PNP with myelin model to generate Figure 5, 7 [11]

Parameter	Value	Description
C_m	1.45 $\mu F/cm^2$	Membrane capacitance
C_{my}	0.15 $\mu F/cm^2$	Myelin capacitance
l_I	70 μm	Internodal distance
l_{NOR}	5.0 μm	Length of node of Ranvier
l_A	1500 μm	Total length of neuronal axon
δ_{pa}	12 nm	Thickness of peri-axonal space

Table B.6: Rat axon values used for the PNP model with myelin and peri-axonal space used to generate Figure 6

Bibliography

[1] Saurabh S. Mogre, Aidan I. Brown, and Elena F. Koslover. “Getting around the cell: physical transport in the intracellular world”. In: *Physical Biology* 17 (2020), p. 061003.

[2] Christina M. Marion, Kryslaine L. Radomski, Nathan P. Cramer, Zygmunt Galdzicki, and Regina C. Armstrong. “Experimental Traumatic Brain Injury Identifies Distinct Early and Late Phase Axonal Conduction Deficits of White Matter Pathophysiology, and Reveals Intervening Recovery”. In: *The Journal of Neuroscience* 38(41) (2018), pp. 8723–8736.

[3] Jorge J. Palop et al. “Aberrant Excitatory Neuronal Activity and Compensatory Remodeling of Inhibitory Hippocampal Circuits in Mouse Models of Alzheimer’s Disease”. In: *Neuron* 55 (2007), pp. 697–711.

[4] Jorge J. Palop and Lennart Mucke. “Amyloid-β Induced Neuronal Dysfunction in Alzheimer’s Disease: From Synapses toward Neural Networks”. In: *Nature Neuroscience* 13 (2010), pp. 812–818.

[5] Swagata Ghatak et al. “Mechanisms of hyperexcitability in Alzheimer’s disease hiPSC-derived neurons and cerebral organoids vs isogenic controls”. In: *eLife* 8 (2019), e50333.

[6] Dipesh Chaudhury, He Liu, and Ming-Hu Han. “Neuronal Correlates of Depression”. In: *Cellular and molecular life sciences* 72(24) (2015), pp. 4825–4848.

[7] A.L. Hodgkin and A.F. Huxley. “A quantitative description of membrane current and its application to conduction and excitation in nerve”. In: *The Journal of Physiology* 117(4) (1952), pp. 500–544.

[8] Andrew F. Huxley. “Ion movements during nerve activity”. In: *Annals New York Academy of Sciences* 81 (1959), pp. 221–246.

[9] Ian D. Duncan and Abigail B. Radcliff. “Inherited and acquired disorders of myelin: The underlying myelin pathology”. In: *Experimental Neurology* 283 (2016), pp. 452–475.

[10] X Zhan et al. “Myelin injury and degraded myelin vesicles in Alzheimer’s disease”. In: *Current Alzheimer research* 11(3) (2014), pp. 232–238.

[11] Charles C.H. Cohen, Marko A. Popovic, Jan Klooster, Marie-Theres Weil, Wiebke Möbius, Klaus-Armin Nave, and Maarten H.P. Kole. “Saltatory conduction along myelinated axons involves a periaxonal nanocircuit”. In: *Cell* 180 (2020), pp. 311–322.

[12] A.G. Richardson, C.C. McIntyre, and W.M. Grill. “Modelling the effects of electric fields on nerve fibres: influence of the myelin sheath”. In: *Medical and Biological Engineering and Computing* 38 (2000), pp. 438–446.

[13] Ellen F. Barett and John N. Barrett. “Intracellular recording from vertebrate myelinated axons: mechanism of the depolarizing afterpotential”. In: *Journal of Physiology* 323 (1982), pp. 117–144.

[14] A.R. Blight. “Computer simulation of action potentials and afterpotentials in mammalian myelinated axons: the case for a lower resistance myelin sheath”. In: *Neuroscience* 15 (1985), pp. 13–31.

[15] A.R. Blight and S. Someya. “Depolarizing afterpotentials in myelinated axons of mammalian spinal cord”. In: *Neuroscience* 15 (1985), pp. 1–12.

[16] Jurgis Pods, Johannes Schonke, and Peter Bastian. "Electrodiffusion Models of Neurons and Extracellular Space Using the Poisson-Nernst-Planck Equations—Numerical Simulation of the Intra- and Extracellular Potential for an Axon Model". In: *Biophysical Journal* 105 (2013), pp. 242–254.

[17] Yoichiro Mori. "From Three-Dimensional Electrophysiology to the Cable Model: an Asymptotic Study". In: *arXiv preprint* 0901. (2009), p. 3914.

[18] Ning Qian and T.J. Sejnowski. "An Electro-Diffusion Model for Computing Membrane Potentials and Ionic Concentrations in Branching Dendrites, Spines and Axons". In: *Biological Cybernetics* 62 (1989), pp. 1–15.

[19] Geir Halnes, Ivar Ostby, Klas H. Pettersen, Stig W. Omholt, and Gaute T. Einevoll. "Electrodiffusive Model for Astrocytic and Neuronal Ion Concentration Dynamics". In: *PLoS Computational Biology* 9(12) (2013), e1003386.

[20] Yoichiro Mori and Charles S. Peskin. "A Numerical method for cellular electrophysiology based on the electrodiffusion equations with internal boundary conditions at membranes". In: *Communications in Applied Mathematics and Computational Science* 4 (2009), pp. 85–134.

[21] Geir Halnes, Tuomo Maki-Marttunen, Daniel Keller, Klas H. Pettersen, Ole A. Andreassen, and Gaute T. Einevoll. "Effect of Ionic Diffusion on Extracellular Potentials in Neural Tissue". In: *PLOS Computational Biology* 12(11) (2016), e1005193.

[22] Courtney L. Lopreore, Thomas M. Bartol, Jay S. Coggan, Daniel X. Keller, Gina E. Sosinsky, Mark H. Ellisman, and Terrence J. Sejnowski. "Computational Modeling of Three-Dimensional Electrodiffusion in Biological Systems: Application to the Node of Ranvier". In: *Biophysical Journal* 95 (2008), pp. 2624–2635.

[23] Ibrahima Dione, Jean Deteix, Thomas Briffard, and Eric Chamberland. "Improved Simulation of Electrodiffusion in the Node of Ranvier by Mesh Adaptation". In: *PLOS ONE* 11(8) (2016), e0161318.

[24] Alain Goriely et al. "Mechanics of the brain: perspectives, challenges, and opportunities". In: *Biomechanics and Modeling in Mechanobiology* 14 (2015), pp. 931–965.

[25] D. Garcia-Gonzalez and A. Jerusalem. "Energy based mechano-electrophysiological model of CNS damage at the tissue scale". In: *Journal of the Mechanics and Physics of Solids* 125 (2019), pp. 22–37.

[26] Man Ting Kwong et al. "3D finite element formulation for mechanical– electrophysiological coupling in axonopathy". In: *Computer Methods in Applied Mechanics and Engineering* 346 (2019), pp. 1025–1050.

[27] Debabrata Auddya, Xiaoxuan Zhang, Rahul Gulati, Ritvik Vasan, Krishna Garikipati, Padmini Rangamani, and Shiva Rudraraju. "Biomembranes undergo complex, non-axisymmetric deformations governed by Kirchhoff-Love kinematics and revealed by a three dimensional computational framework". In: *Proceedings of the Royal Society A* 477(2255) (2021), p. 20210246.

[28] Andrew F. Huxley. "Ion movements during nerve activity". In: *Second conference on physicochemical mechanism of nerve activity and second conference on muscular contraction* 81(2) (1959), pp. 221–246.

[29] Christof Koch. *Biophysics of Computation: Information Processing in Single Neurons*. Vol. 1. Oxford University Press, 2004.

[30] D.I. Stephanova and H. Bostock. "A distributed-parameter model of the myelinated human motor nerve fibre: temporal and spatial distributions of action potentials and ionic currents". In: *Biological Cybernetics* 73 (1995), pp. 275–280.

[31] Eyal Bar-Kochba, Mark T Scimone, Jonathan B Estrada, and Christian Franck. “Strain and rate-dependent neuronal injury in a 3D in vitro compression model of traumatic brain injury”. In: *Scientific Reports* 6.1 (2016), pp. 1–11.

[32] Wei Li, Qingyu Fan, Zhenwei Ji, Xiuchun Qiu, and Zhao Li. “The effects of irreversible electroporation (IRE) on nerves”. In: *PloS one* 6.4 (2011), e18831.

[33] Jonathan B Estrada, Harry C Cramer III, Mark T Scimone, Selda Buyukozturk, and Christian Franck. “Neural cell injury pathology due to high-rate mechanical loading”. In: *Brain Multiphysics* 2 (2021), p. 100034.

[34] Jorge J Palop and Lennart Mucke. “Network abnormalities and interneuron dysfunction in Alzheimer disease”. In: *Nature Reviews Neuroscience* 17.12 (2016), pp. 777–792.

[35] Swagata Ghatak et al. “Mechanisms of hyperexcitability in Alzheimer’s disease hiPSC-derived neurons and cerebral organoids vs isogenic controls”. In: *Elife* 8 (2019), e50333.

[36] Doo Yeon Kim et al. “BACE1 regulates voltage-gated sodium channels and neuronal activity”. In: *Nature cell biology* 9.7 (2007), pp. 755–764.

[37] Jeffrey P. Freidberg. *Plasma Physics and Fusion Energy.* Vol. 1. Cambridge University Press, 2008.

[38] *Code repository for Action potential propagation along the neuronal axon and spatio-temporal saltatory conduction.* https://github.com/cmmg/ neuronalActionPotential. 2022.

[39] Thibault Lagache, Krishna Jayant, and Rafael Yuste. “Electrodiffusion models of synaptic potentials in dendritic spines”. In: *Journal of Computational Neuroscience* 47 (2019), pp. 77–89.

[40] Jerome Cartailler and David Holcman. “Electrical transient laws in neuronal microdomains based on electro-diffusion”. In: *Physical Chemistry Chemical Physics* 20(32) (2018), pp. 21062–21067.

[41] Jerome Cartailler, Taekyung Kwon, Rafael Yuste, and David Holcman. “Deconvolution of voltage sensor time series and electro-diffusion modeling reveal the role of spine geometry in controlling synaptic strength”. In: *Neuron* 97(5) (2018), pp. 1126–1136.

[42] Lucy M. Palmer and Greg J. Stuart. “Membrane potential changes in dendritic spines during Action potentials and synaptic input”. In: *The Journal of Neuroscience* 29(21) (2009), pp. 6897–6903.

[43] David Holcman and Rafael Yuste. “The new nanophysiology: regulation of ionic flow in neuronal subcompartments”. In: *Nature Reviews Neuroscience* 16(11) (2015), pp. 685–692.

[44] Corey D. Acker, Erika Hoyos, and Leslie M. Loew. “EPSPs measured in proximal dendritic spines of cortical pyramidal neurons”. In: *eNeuro* 3(2) (2016), pp. 1–13.

[45] Taekyung Kwon, Masayuki Sakamoto, Darcy S. Peterka, and Rafael Yuste. “Attenuation of synaptic potentials in dendritic spines”. In: *Cell Reports* 20(5) (2017), pp. 1100–1110.

[46] Krishna Jayant et al. “Targeted intracellular voltage recordings from dendritic spines using quantum-dot-coated nanopipettes”. In: *Nature nanotechnology* 12(4) (2017), pp. 335–342.

[47] Rafael Yuste. “Electrical compartmentalization in dendritic spines”. In: *Annual review of neuroscience* 36 (2013), pp. 429–449.

[48] Mark T. Harnett, Judit K. Makara, Nelson Spruston, William L. Kath, and Jeffrey C. Magee. “Synaptic amplification by dendritic spines enhances input cooperativity”. In: *Nature* 491(7425) (2012), pp. 599–602.

[49] Roberto Araya, Jiang Jiang, Kenneth B. Eisenthal, and Rafael Yuste. “The spine neck filters membrane potentials”. In: *Proceedings of the National Academy of Sciences* 103(47) (2006), pp. 17961–17966.

[50] Dax A. Hoffman, Jeffrey C. Magee, Costa M. Colbert, and Daniel Johnston. “K+ channel regulation of signal propagation in dendrites of hippocampal pyramidal neurons”. In: *Nature* 387(6636) (1997), pp. 869–875.

[51] Costa M. Colbert and Daniel Johnston. “Axonal action-potential initiation and Na+ channel densities in the soma and axon initial segment of subicular pyramidal neurons”. In: *Journal of Neuroscience* 16(21) (1996), pp. 6676–6686.

[52] Rahul Gulati and Shiva Rudraraju. “Spatio-temporal modeling of saltatory conduction in neurons using Poisson–Nernst–Planck treatment and estimation of conduction velocity”. In: *Brain Multiphysics* 4 (2023), pp. 100061–100072.

[53] Marko A. Popovic, Nicholas Carnevale, Balazs Rozsa, and Dejan Zecevic. “Electrical behaviour of dendritic spines as revealed by voltage imaging”. In: *Nature communications* 6(1) (2015), pp. 8436–8448.

[54] Jan Tønnesen, Gergely Katona, Balázs Rózsa, and U Valentin Nägerl. “Spine neck plasticity regulates compartmentalization of synapses”. In: *Nature neuroscience* 17 (2014), pp. 678–685.

[55] R. Wilbers et al. “Human voltage-gated Na+ and K+ channel properties underlie sustained fast AP signaling”. In: *Science Advances* 9 (2023), eade3300.

[56] Christopher Zimmermann, Deepesh Toshniwal, Chad M. Landis, Thomas J.R. Hughes, Kranthi K. Mandadapu, and Roger A. Sauer. “An isogeometric finite element formulation for phase transitions on deforming surfaces”. In: *Computer Methods in Applied Mechanics and Engineering* 351 (2019), pp. 441–477.

[57] Roger A. Sauer and Thang X. Duong. “On the theoretical foundations of thin solid and liquid shells”. In: *Mathematics and Mechanics of Solids* 22(3) (2017), pp. 343–371.

[58] Roger A. Sauer, Thang X. Duong, Kranthi K. Mandadapu, and David J. Steigmann. “A stabilized finite element formulation for liquid shells and its application to lipid bilayers”. In: *Journal of Computational Physics* 330 (2017), pp. 436–466.

[59] Mehrdad Zareh and Xiaoping Qian. “Kirchhoff–Love shell formulation based on triangular isogeometric analysis”. In: *Computer Methods in Applied Mechanics and Engineering* 347 (2019), pp. 853–873.

[60] PG Saffman and M Delbrück. “Brownian motion in biological membranes.” In: *Proceedings of the National Academy of Sciences* 72.8 (1975), pp. 3111–3113.

[61] J Balakrishnan. “Spatial curvature effects on molecular transport by diffusion”. In: *Physical Review E* 61(4) (2000), p. 4648.

[62] Jordi Faraudo. “Diffusion equation on curved surfaces. I. Theory and application to biological membranes”. In: *The Journal of chemical physics* 116(13) (2002), pp. 5831–5841.

[63] R. R. Molina, S. Liese, and A. Carlson. “Diffusion on membrane domes, tubes, and pearling structures.” In: *Biophysical Journal* 120(3) (2021), pp. 424–431.

[64] Colin James Stockdale Klaus, Krishnan Raghunathan, Emmanuele DiBenedetto, and Anne K. Kenworthy. “Analysis of diffusion in curved surfaces and its application to tubular membranes”. In: *Molecular Biology of the Cell* 27(24) (2016), pp. 3937–3946.

[65] WT Góźdź. “Shape transformation of lipid vesicles induced by diffusing macromolecules”. In: *The Journal of Chemical Physics* 134(2) (2011).

[66] Ashutosh Agrawal and David J Steigmann. “A model for surface diffusion of trans-membrane proteins on lipid bilayers”. In: *Zeitschrift für angewandte Mathematik und Physik* 62 (2011), pp. 549–563.

[67] Roger Tran-Son-Tay, SP Sutera, and PR Rao. “Determination of red blood cell membrane viscosity from rheoscopic observations of tank-treading motion”. In: *Biophysical journal* 46(1) (1984), pp. 65–72.

[68] Hiroshi Noguchi and Gerhard Gompper. “Fluid vesicles with viscous membranes in shear flow”. In: *Physical review letters* 93(25) (2004), p. 258102.

[69] Patrick D Tran, Thomas A Blanpied, and Paul J Atzberger. “Protein drift-diffusion dynamics and phase separation in curved cell membranes and dendritic spines: Hybrid discrete-continuum methods”. In: *Physical Review E* 106(4) (2022), p. 044402.

[70] Prerna Gera and David Salac. “Cahn–Hilliard on surfaces: A numerical study”. In: *Applied Mathematics Letters* 73 (2017), pp. 56–61.

[71] Gerbrand Koster, Martijn VanDuijn, Bas Hofs, and Marileen Dogterom. “Membrane tube formation from giant vesicles by dynamic association of motor proteins”. en. In: *Proc. Natl. Acad. Sci. U. S. A.* 100.26 (Dec. 2003), pp. 15583–15588.

[72] Paige M Shaklee, Timon Idema, Gerbrand Koster, Cornelis Storm, Thomas Schmidt, and Marileen Dogterom. “Bidirectional membrane tube dynamics driven by nonprocessive motors”. In: *Proceedings of the National Academy of Sciences* 105.23 (June 2008), pp. 7993–7997.

[73] Mijo Simunovic et al. “Friction Mediates Scission of Tubular Membranes Scaffolded by BAR Proteins”. en. In: *Cell* 170.1 (June 2017), 172–184.e11.

[74] Sandrine Morlot and Aurélien Roux. “Mechanics of dynamin-mediated membrane fission”. en. In: *Annu. Rev. Biophys.* 42 (2013), pp. 629–649.

[75] Leopold Kong et al. “Cryo-EM of the dynamin polymer assembled on lipid membrane”. en. In: *Nature* 560.7717 (Aug. 2018), pp. 258–262.

[76] Imre Derényi, Frank Jülicher, and Jacques Prost. “Formation and interaction of membrane tubes”. In: *Physical review letters* 88.23 (2002), p. 238101.

[77] Reinhard Lipowsky. “Spontaneous tubulation of membranes and vesicles reveals membrane tension generated by spontaneous curvature”. In: *Faraday discussions* 161 (2012), pp. 305–331.

[78] Amir Houshang Bahrami and Gerhard Hummer. “Formation and stability of lipid membrane nanotubes”. en. In: *ACS Nano* 11.9 (Sept. 2017), pp. 9558–9565.

[79] Ritvik Vasan, Shiva Rudraraju, Matthew Akamatsu, Krishna Garikipati, and Padmini Rangamani. “A mechanical model reveals that non-axisymmetric buckling lowers the energy barrier associated with membrane neck constriction”. In: *Soft Matter* (2020).

[80] Quentin Goutaland, Frédéric van Wijland, Jean-Baptiste Fournier, and Hiroshi Noguchi. “Binding of thermalized and active membrane curvature-inducing proteins”. In: *Soft Matter* 17(22) (2021), pp. 5560–5573.

[81] Rijk de Rooij, Ellen Kuhl, and Kyle E. Miller. “Modeling the Axon as an Active Partner with the Growth Cone in Axonal Elongation”. In: *Biophysical Journal* 115 (2018), pp. 1783–1795.

[82] *Microtubule cartoon.* `https://commons.wikimedia.org/wiki/File:Kinesin_cartoon.png`. Accessed: 2023-01-23.

[83] J. C. Simo and T. J. R. Hughes. *Computational Inelasticity.* Vol. 1. Springer New York, NY, 1998.

[84] Pierre-Alexandre Boucher, Béla Joós, and Catherine E. Morris. “Coupled left-shift of Nav channels: modeling the Na^+-loading and dysfunctional excitability of damaged axons”. In: *Journal of Computational Neuroscience* 33 (2012), pp. 301–319.

[85] Peter Läuger. *Electrogenic ion pumps.* Vol. 1. Sinauer, 1991.

[86] H. Kager, W. J. Wadman, and G. G. Somjen. “Simulated Seizures and Spreading Depression in a Neuron Model Incorporating Interstitial Space and Ion Concentrations”. In: *Journal of Neurophysiology* 84 (2000), pp. 495–512.

[87] Na Yu, Catherine E. Morris, Béla Joós, and André Longtin. “Spontaneous Excitation Patterns Computed for Axons with Injury-like Impairments of Sodium Channels and Na/K Pumps”. In: *PLOS Computational Biology* 8 (2012), e1002664.

[88] Michael Muller and George G. Somjen. “Na^+ and K^+ Concentrations, Extra- and Intracellular Voltages, and the Effect of TTX in Hypoxic Rat Hippocampal Slices”. In: *Journal of Neurophysiology* 83 (2000), pp. 735–745.